UNIVERSITA' DEGLI STUDI DI NAPOLI "FEDERICO II"

Facoltà di Scienze Matematiche, Fisiche e Naturali

DOTTORATO DI RICERCA IN SCIENZE DELLA TERRA
(indirizzo Geofisica e Vulcanologia)
XX CICLO

Upper crustal structure and seismotectonics of the Val d'Agri area, Southern Italy, through integration of local earthquake and active seismic tomographies, and geological mapping

Tutor
Dott. Luigi Ferranti

Dottoranda
Luisa Valoroso

Correlatori
Dott. Claudio Chiarabba
Dott. Luigi Improta

Coordinatore
Prof. Giuseppe Nardi

2004-2007

Contents

Introduction

Seismic hazard assessment requires the accurate knowledge of the location, geometry and kinematics of active faults able to generate moderate to large earthquakes.

In southern Apennines this topic is a difficult task to achieve because of the youthfulness of the active NE-oriented extensional stress regime (about 700 kyr) and the low extensional rates (≈1-3 mm/yr), which combine in concealing surface-faulting traces. This makes challenging the identification of active faults by geological and geomorphological mapping alone, and allows to explain why most of the large Apennine historical earthquakes have not been associated with precise causative faults so far.

The Agri valley is an intramontane basin located in the axial portion of the southern Apennines in the Lucania region. This area, with up to M7 earthquakes, is the most seismically active sector of the central-western Mediterranean region, and has been repeatedly struck by destructive earthquakes (i.e. 1857 Me7 Basilicata earthquake, 1980 M6.9 Campania-Basilicata earthquake). Active fault systems in the area have been investigated by field studies and commercial reflection profiles. Nonetheless their geometry and kinematics are not fully constrained and even the seismogenic source of the 1857 Basilicata earthquake is still debated.

This work focuses on defining location, geometry and kinematics of recent and active faults in the Val d'Agri area, by integrating passive and active seismic data with detailed geological mapping. The integration of these different datasets provides a detailed image of the upper crustal structure allowing to constrain geometry and kinematics of recent and active faults from seismogenic depths toward the surface. This multidisciplinary approach represents a powerful and necessary tool to investigate active tectonics in areas of complex tectonic history.

The data used in this work are:

1) *Background seismicity*: the use of dense seismic networks allows the lowering of magnitude threshold for earthquakes detection along active faults. This is a prerequisite to investigate source parameters, deep structure, kinematics, present day seismic activity and deep geometry of active faults. With these motivations form May 2005 to July 2006 a dense temporary network of up to 23 seismic stations was operated in the axial sector of the Lucanian Apennines. The seismic network covers an area of about 1500 km^2 including the Val d'Agri basin, partially the Vallo di Diano basin and the Monti Alpi (fig. 1).

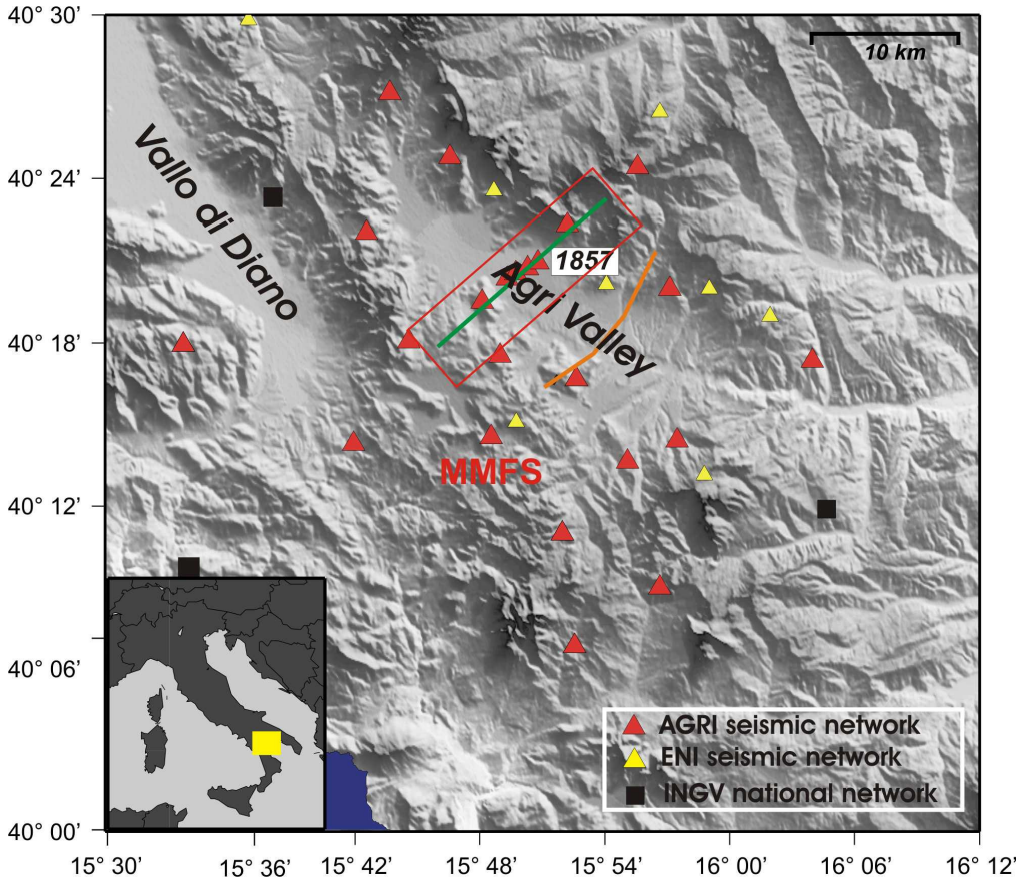

The Agri Valley temporary seismic network (red triangles) complemented by permanent stations of the ENI (yellow triangles) and Italian National seismic network (black squares). The green and orange lines represent the two multifold wide-aperture profiles used to image the basin structure. The area investigated through detailed geological mapping is contoured by the red rectangle. The macroseismic epicentre of the 1857 Basilicata earthquake is also shown.

Low-magnitude seismic events are used to define the upper crustal velocity structure through local earthquake tomography, and to gain original information on the fault structure at depth.

2) *High-resolution crustal profiles*: Two multi-fold wide-aperture seismic crustal profiles, about 15 km long, crossing the central sector of the Agri basin, are analysed to obtain a detailed image of the shallow crustal structure of the basin down to about 2 km depth. This analysis provides an unique opportunity to fill the information gap that commonly exists between the surface geologic trench data (about 3-5 m) and by field surveys (extrapolated to about few hundred meters), and those obtained by seismic or seismological data (depth > 2 km).

3) *Geological mapping and fault kinematics data:* the reconstruction of detailed geological mapping together with fault kinematics analysis allows to compare and verify the existence of

geometric and kinematic correspondence between the Quaternary faults mapped at the surface and those observed by geophysical data.

In chapter 1, the tectonic evolution of the southern Apennines focusing on the Lucanian region and on the Val d'Agri area is briefly reviewed. As main target of this study, a particular attention is addressed to the recent Quaternary extensional deformation.

In chapter 2, hypocentral locations of the background seismicity recorded by the Val d'Agri seismic network are presented. Furthermore, focal mechanisms of selected events and the seismic behaviour in term of seismic release with time are shown.

In the third chapter, I present high-resolution tomographic images of the Agri basin (down to 1.5 km depth) obtained by analysing two multifold wide-aperture seismic crustal profiles, about 15 km long, crossing the central sector of the basin. The non-linear first-arrival traveltimes inversion procedure is described and a geological and structural interpretation of the tomographic models is discussed.

In the fourth chapter, I present the results of detailed geological mapping and fault kinematics analysis carried out along the seismic profiles (chapter 3), in areas where the connection between surface geology and geophysics is particular critical.

In chapter 5, the three-dimensional velocity structure of the Val d'Agri area and the relocated seismicity are presented. The tomographic inversion of both the *P*-wave arrival times (from the local earthquakes) and the differences $S - P$ yields high resolution *Vp* and *Vp/Vs* models respectively, down to 12 km depth. The local earthquake tomography procedure is described and an interpretation of the obtained velocity models is discussed.

Finally, conclusive remarks about the structural setting and seismotectonics of the Val d'Agri area are summarized.

Chapter 1

The southern Apennines and the Val d'Agri area: seismotectonic setting

Introduction

The Val d'Agri is an intramontane basin located in the axial portion of the southern Apennines in the Lucania region. This area, with up to M7 earthquakes, is the most seismically active sector of the central-western Mediterranean region, and has been repeatedly struck by destructive earthquakes (i.e. 1857 Me7 Basilicata earthquake, 1980 M6.9 Campania-Basilicata earthquake).

The Val d'Agri area is characterized by a complex pattern of thrusts, folds and normal faults reflecting the superposition of two main tectonic phases: a Mio-Pliocene compression forming E-NE verging thrusts and folds and, starting from Early-Middle Pleistocene, an extensional tectonics with a NE-SW stretching axis (Mazzoli *et al*., 2000; Menardi Noguera and Rea, 2000; among many others).

This change in the tectonic regime occurred with the development, in the inner and axial zone of the southern Apennines, of large extensional and transtensional faults, which crosscut the pre-existing contractional structures (Catalano *et al*., 1993; Cinque *et al*., 1993; Hyppolite *et al*., 1994; D'Agostino *et al*., 2001).

As inferred by focal mechanisms of strong earthquakes and borehole breakout data, the NE-SW oriented extension is still active and is responsible for the present-day crustal seismicity of the southern Apennines (Gasparini *et al*., 1985; Amato and Montone, 1997, Chiarabba *et al*., 2005) (fig. 1-1). Earthquakes characterized by predominant normal-faulting focal mechanisms, with NW-oriented nodal planes, occur within a narrow seismic belt, about 20 to 40 km wide, centred on the axis of the Apennine chain (Amato *et al*., 1997; Selvaggi, 1998; Galadini *et al*., 2000a; Valensise & Pantosti, 2001) (fig. 1-1). Quaternary extension is commonly expressed by SW-dipping faults. However, in the present seismogenic belt, coseismic faulting locally occurs on NE-dipping structures (e.g. the seismogenic source for the 1980 M6.9 Campania-Basilicata earthquake).

In the following paragraphs, the tectonic evolution of the southern Apennines focusing on the lucanian region and on the Val d'Agri area will be briefly reviewed. As main target of this study, a particular attention will be addressed to the recent Quaternary extensional deformation.

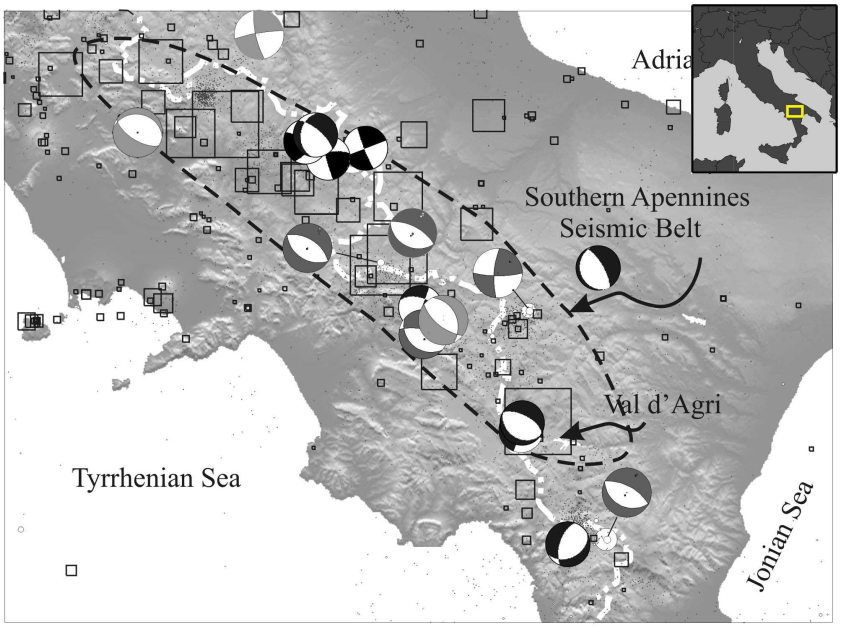

Fig. 1-1. Southern Apennines seismic belt is contoured by the black dashed line (from Valensise & Pantosti 2001); the white dashed line represents the chain axis; instrumental (black dots) and historical (squares, scaled from Me) seismicity; focal mechanisms (4.2 < M < 6.9) are derived from Harvard CMT Catalogue (in grey) and Gasparini *et al*. (1985, in black). (from Maschio *et al*., 2005)

The Apennine chain

The Apennine thrust belt of Italy forms part of the Africa-verging mountain system in the Alpine-Mediterranean area. The belt runs northwest to southeast forming the topographic backbone of Italy and is associated with the Tyrrhenian back-arc basin to the west and with a foredeep, to the east, that includes part of the Po plain, part of the Adriatic sea, the Bradano Though onshore in southern Italy. The belt can be divided into two major arcs, the northern Apennines and the southern Apennines – Calabrian arc (fig. 1-2).

The Mediterranean area evolved in the framework of convergent motion between the Africa and European plates since late Cretaceous (Dewey *et al*., 1989). North-south convergence between Africa and Eurasia was dominant up to Oligocene time; since Upper Tortonian, the basin-thrust belt-foredeep system migrated eastward driven by gravity-induced sinking of the Adriatic (continental) and Ionian (oceanic) lithosphere and related subduction roll-back (e.g. Malinverno and Ryan, 1986; Dewey *et al*., 1989; Patacca and Scandone, 1989; Doglioni, 1991; Faccenna *et al*., 1996). The progressive propagation of the compression toward the Apulia foreland is clearly documented by the development and evolution of a series of eastward younger foredeep basins, and of small basins developed on top of the advancing allochtonous units (Patacca and Scandone, 2001). Mainly east to north-east directed thrusting

in the southern Apennines lasted until the Early Pleistocene (Patacca *et al*., 1990). The geometry of the orogenic wedge was later modified, during the Pleistocene, by strike-slip tectonics developed during the final stages of continent-continent collision (Catalano *et al*., 1993). Since the Middle Pleistocene, deformation was characterized by NE-SW extension on NW-SE striking high-angle normal faults. The Middle Pleistocene kinematic pattern is ongoing as documented by focal mechanisms of large earthquakes and borehole breakout data (Gasparini *et al*., 1985; Montone *et al*., 2004, Pondrelli *et al*., 2004; 1997-2004 Harvard QRCMT Catalogue on http://mednet.ingv.it/events/QRCMT/html).

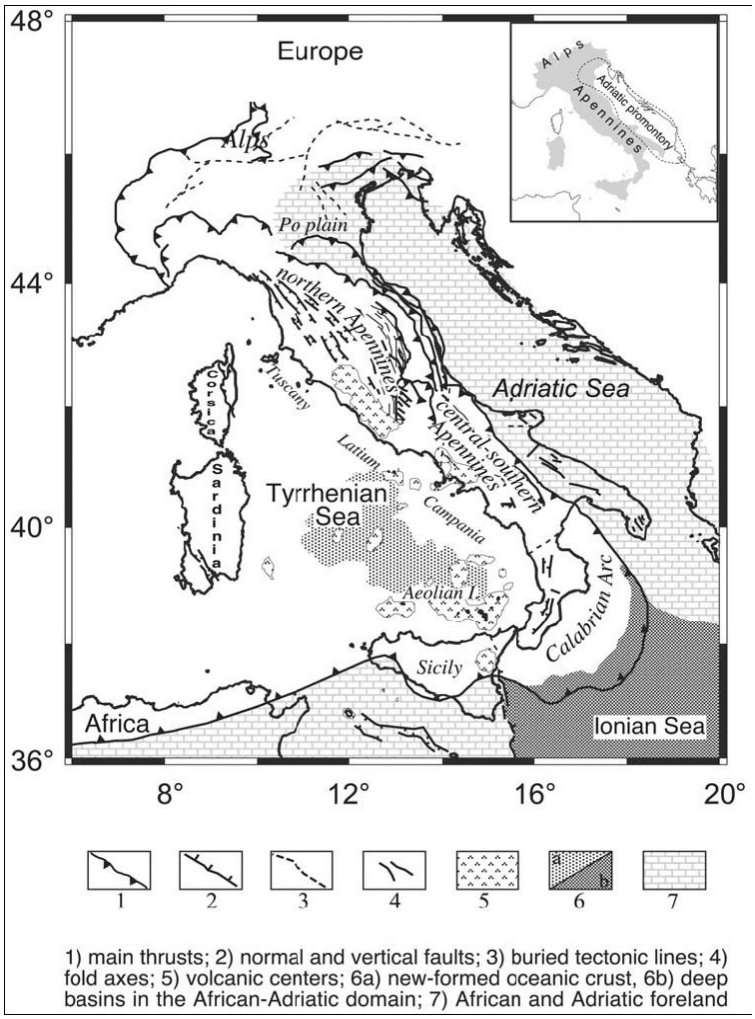

Fig. 1-2. Structural map of the italian region. The main geographical and tectonic units are shown (from Margheriti *et al*., 2003).

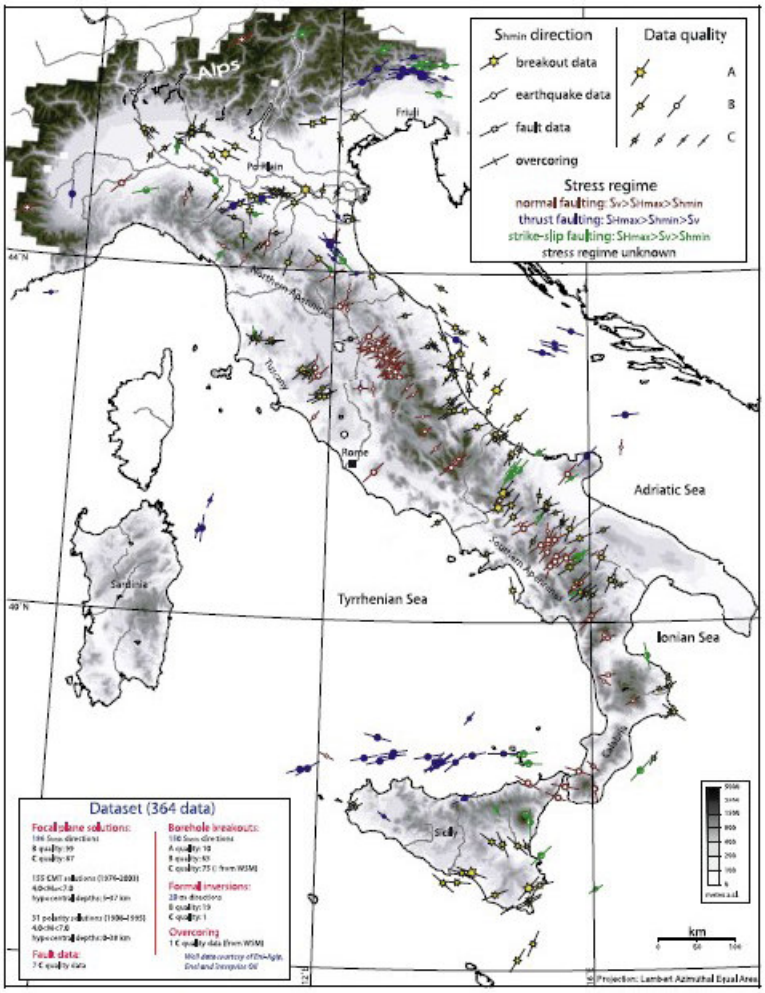

Fig. 1-3. Active stress map of Italy with minimum horizontal stress orientation (from Montone *et al.*, 2004).

The Lucanian Apennines

The knowledge about the shallow and deep structure of the Lucanian Apennines (fig. 1-4a/b) has been strongly improved during last two decades thanks to the huge amount of seismic data acquired in the area for oil exploration (Mostardini & Merlini, 1986; Casero *et al.*, 1991; Mazzoli *et al.*, 2000; Mazzotti *et al.*, 2000; Menardi Noguera and Rea, 2000; Shiner *et al.*, 2004; Butler *et al.*, 2004; Scrocca *et al.*, 2005). The area, in fact, hosts important oil fields where the reservoirs are the thick carbonates of the Apulian platform.

The Lucanian Apennines includes allochthonous units derived from the deformation since Tortonian times of both carbonate platform (Apennine Platform; D'Argenio *et al.*, 1972) and pelagic basin (Lagonegro basin; Scandone, 1972) sequences of the Adria domain (Patacca and Scandone, 1992). These units are tectonically overlain by Lower-Middle Miocene turbiditic

sequences and thrust-top-basin deposists (Albidona and Gorgoglione Formations) of the Sicilide Nappe, originally deposited in a more internal oceanic domain and deformed before the opening of the Tyrrhenian basin (figg. 1-4, 1-5). These units are completely detached from their original substratum (Adria continental crust) and transported, together with detached Miocene foredeep sediments, onto the foreland carbonates of the Apulian platform, depositionally overlain by Pliocene terrigenous marine deposits. These structures suffered repeated thin-skinned thrust: firstly the Apenninic platform (D'Argenio *et al*., 1973) over the previously folded Lagonegro basin deposits and secondly the stacked allochthon over the Apulian platform (e.g. Scandone, 1972; Cello and Mazzoli, 1999; Mazzoli *et al*., 2001) (fig. 1-4b).

The detachment between the allochthon and the buried Apulian units is marked by a *mèlange* zone several hundred meters thick. This unit consists predominantly of intensely deformed and overpressured deep-water siltstone and mudstone (e.g. Mazzoli *et al*., 2000; Borraccini *et al*., 2002; Shiner *et al*., 2004; Butler *et al*., 2004) (fig. 1-4).

A schematic section of the thrust stack in the area is (from top to bottom):

- *Internal units:* Liguride and Sicilide nappes represented by remnants of an accretionary wedge developed during oceanic subduction on the Neotethyan domain (Ogniben, 1985; Monaco and Tortorici, 1995; Catalano *et al.*, 2004). These units are unconformably covered by Upper Oligocene-Middle Miocene terrigenous sequences developed both above and ahead of the accretionary prism (Albidona and Gorgoglione Formations, Monaco and Tortorici, 1995).
- *Allochthonous units*: Mesozoic to Paleogene in age, are made of carbonates of the Apenninic Platform and of deep-water silicoclastic deposits of the Lagonegro basin. These units are involved in the thrust belt with the Upper Miocene flysch deposits of the foredeep phase.
- *Apulian Carbonate Platform*: 6-7 km thick succession of Mesozoic and Tertiary shallow marine carbonates. The deeper portion is made up of Upper Triassic interbedded anhydrites and dolomites comprising the Burano Formation drilled in the Apulia foreland.
- *Permian – Lower Triassic clastic succession*: drilled by two deep wells in the foreland area at the base of the Apulia Platform (Puglia 1 and Gargano 1; Improta *et al*., 2000) and loosely correlated to the Verrucano Group cropping out in Central Apennines (Bally *et al*., 1986).

The outcropping units are unconformably covered by Miocene-Pliocene marine and continental deposits and Quaternary continental deposits filling the quaternary intramontane basin (e.g. Val d'Agri, Vallo di Diano, Melandro-Pergola basin in the Lucania sector). Fig.1-5 shows a tectonostratigraphic scheme of the southern Apennines, where Western Platform stands for Apenninic Platform.

Compressional deformation: In the southern Apennines, the compressional deformation of the upper allochthonous units lasted until Early Pliocene (Menardi Noguera and Rea, 2000). During Late Pliocene-Early Pleistocene the tectonic accretion involved also the western portion of the Apulian domain (Inner Apulian Platform, Cello and Mazzoli, 1999; Menardi Noguera and Rea, 2000). These units form antiformal stacks, separated from the undeformed or weakly deformed part of the Apulian platform, which crops out in the Apulia foreland (Outer Apulian Platform of Menardi Noguera and Rea, 2000) (fig. 1-4b). The deep structure of this sector of the Apennines is made problematic by the poor resolution of seismic reflection data (e.g. CROP-04 data, Mazzotti *et al*., 2000; Scrocca *et al*., 2005) that clearly image the top Apulian platform reflector but do not allow a good definition of the internal architecture of the belt. These uncertainties open to different interpretation of the deep tectonic style and of the degree of basement involvement for this sector of the Apennine chain (e.g. thin vs thick-skinned tectonic models). A detailed discussion on this topic can be found in several works (e.g. Mazzoli *et al*., 2000; Butler *et al*., 2004; Shiner *et al*., 2004; Scrocca *et al*., 2005 among many others).

Extensional and strike-slip deformation: After this episode of shortening, lasted from Upper Miocene to Lower Pleistocene (Patacca *et al*., 1990), the southern Apennines belt experienced a change of the displacement field (Cinque *et al*., 1993; Hyppolite *et al*., 1994, Amato and Montone, 1997). During Early Pleistocene the introduction into the trench of the thick continental Adriatic lithosphere slowed the propagation of contraction toward the foreland (Doglioni *et al*., 1994; Lucente *et al*., 1999; Ferranti & Oldow, 2005). Contractional deformation continued at the front of the chain while a mixture of strike-slip and normal faulting occurred along the Tyrrhenian side of the chain (Cinque *et al*., 1993; Hyppolite *et al*., 1994; Monaco *et al*., 1998; Schiattarella *et al*., 1998; Catalano *et al*., 2004).

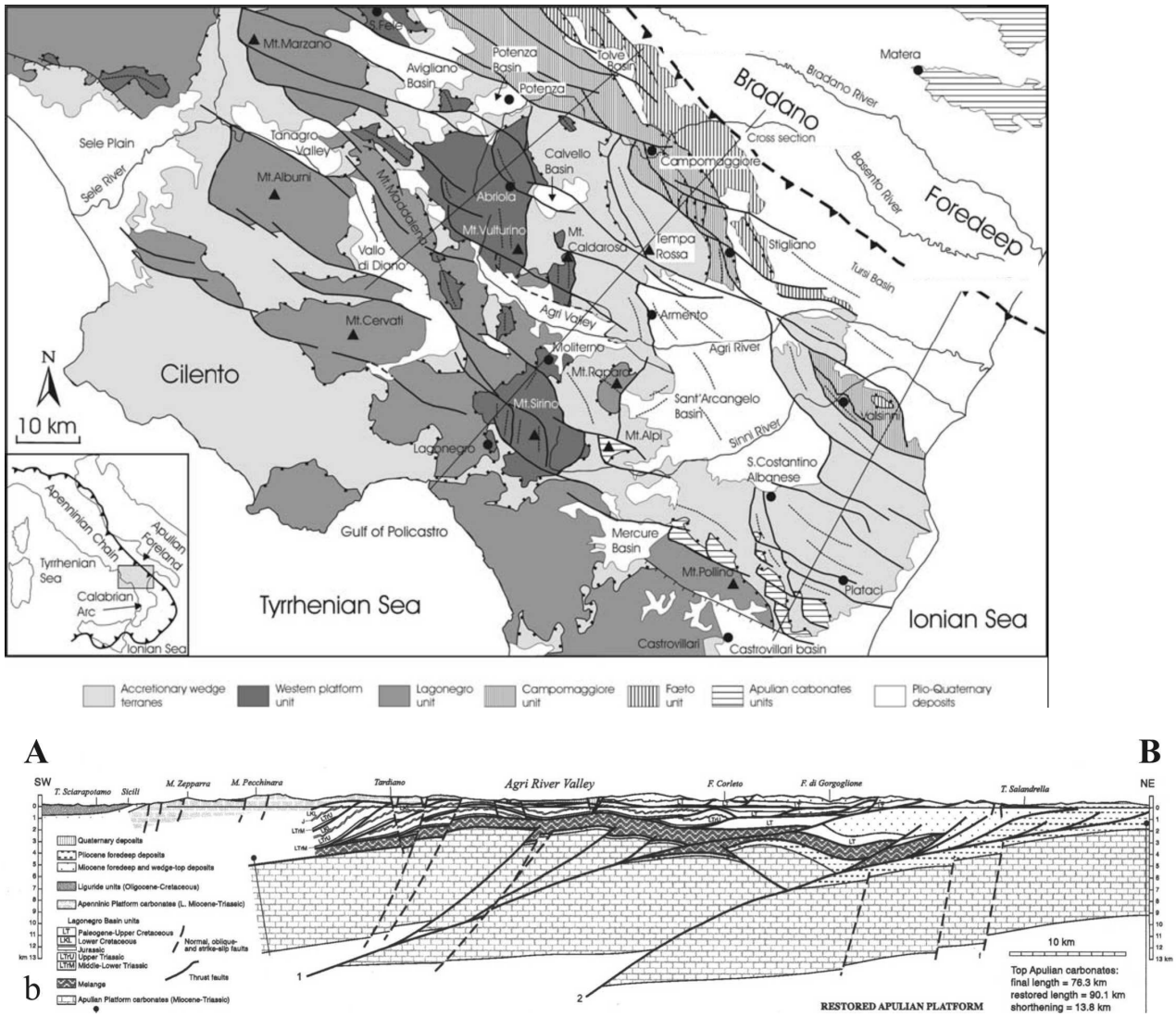

Fig. 1-4. a) tectonostratigraphic map of the southern Apennines. (from Catalano *et al*., 2004). b) Geologic section across the Southern Apennines in the Lucania area (from Butler *et al*., 2004; location in the upper map).

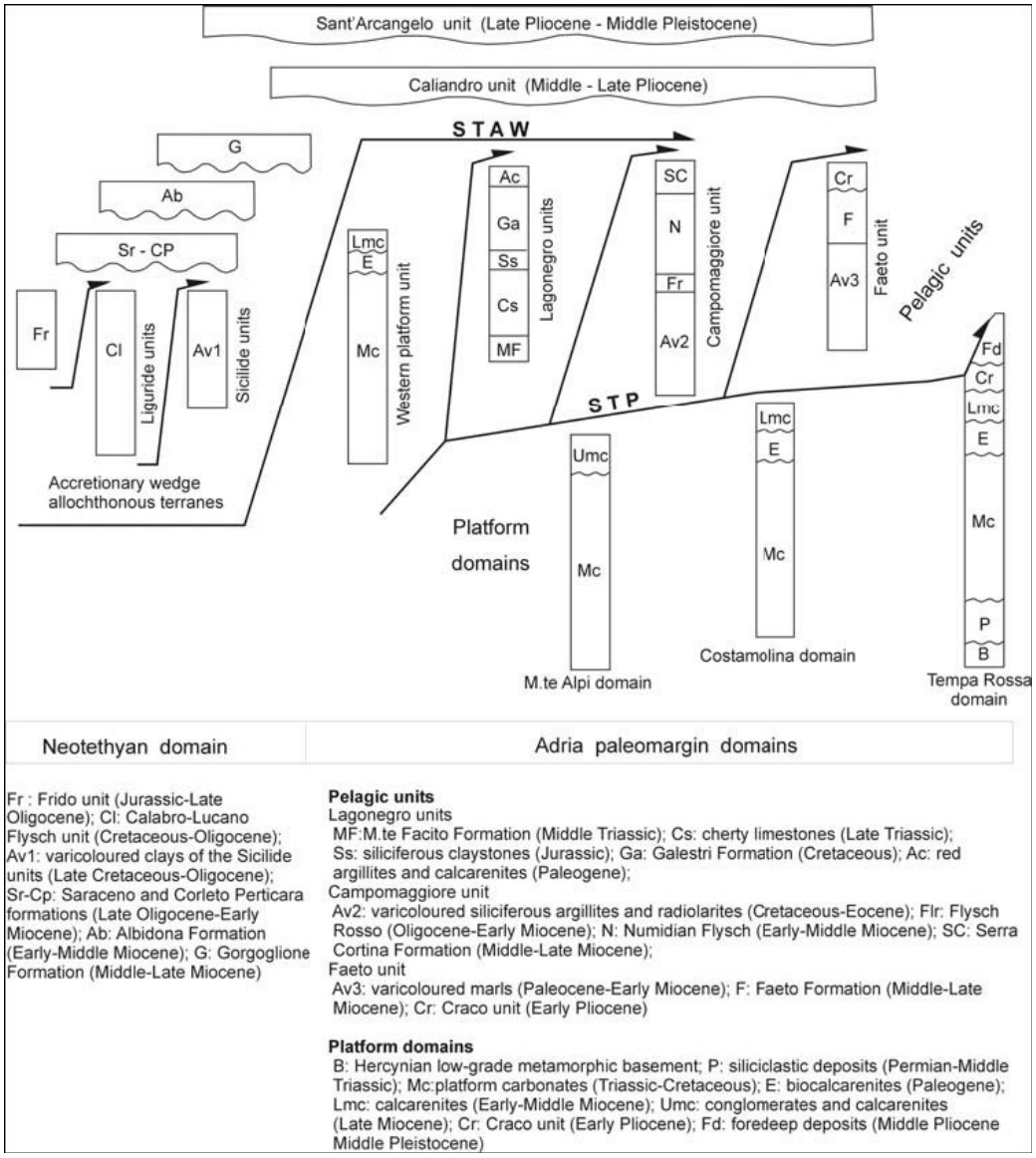

Fig. 1-5. Tectonostratigraphic scheme of the southern Apennines (from Catalano *et al*., 2004)

Since the Middle Pleistocene, deformation was characterized by NE-SW extension on NW-SE striking high-angle normal faults and by a rapid and large uplift (more than 1000 m) affecting the axial portion of the belt where active extension localizes (Hyppolite *et al*., 1994) (fig. 1-4).

The uplift and the recent extension of the belt have been related to the upwelling of the asthenosphere in the Tyrrhenian region following the slab retreat (Di Stefano *et al*., 1999). The absence of deep seismicity in the southern Apennines suggests that the subduction is no longer active. The subducted slab can only be identified by seismic tomography (Amato *et al*., 1993, Lucente *et al*., 1999; Piromallo & Morelli, 1997-2003; Chiarabba *et al*., 2005).

NE-SW extension resulted in development of numerous grabens bounded by normal faults (e.g. Mercure, Vallo di Diano, Val d'Agri, Melandro-Pergola) (fig. 1-4a) and filled by continental Middle Pleistocene sediments, and in volcanic activity along the Tyrrhenian margin.

The bulk of Quaternary extension has been accommodated by SW-dipping faults, which have attained mature morphologic and structural features and, nowadays, separate the mountain range from intramontane basins. Most of these faults are suspected to be active (Galadini *et al*., 2000). However, in the present seismogenic belt, coseismic faulting locally occurs on NE-dipping structures (e.g. the seismogenic source for the 1980 M6.9 Campania-Basilicata earthquake) that could signal seismogenic sources developed very recently (Westaway and Jackson, 1987). Most models envisage a general tendency of the southern Apennines to collapse toward the Tyrrhenian basin. However, the Campania-Basilicata earthquake was generated by a northwest-trending normal fault producing down-throw of the north-eastern Adriatic side (e.g. Valensise and Pantosti, 2001).

The Val d'Agri basin

The high Agri valley basin is a NNW-SSE oriented intramontane basin located in the axial sector of the Lucanian Apennines (fig. 1-4). The basin is filled with Quaternary continental deposits laying on the allochthonous units of the southern Apennines fold and thrust belt. These units consist of carbonates of the Apenninc Platform (Monti della Maddalena Unit, D'Argenio *et al*., 1975) thrust on the coeval pelagic rocks of the Lagonegro basin (Scandone, 1967) and their Miocene synorogenic deposits (fig. 1-6). In the south-eastern portion of the basin, Lower to Middle Miocene turbiditic sequences and thrust-top deposits of the Sicilide nappe extensively crop out.

More in detail, the carbonates of the Monti della Maddalena unit are made of alternation of Jurassic to Cretaceous calcarenites and calcirudites related to an open shelf environment, which is believed to be the marginal to slope part of the platform, overlying intertidal stromatolitic dolomite of Upper Triassic age (D'Argenio *et al*., 1975), while the Lagonegro units consist of Triassic-Miocene carbonate, siliceous, marl and siliciclastic rocks. Rocks of the Lagonegro units mainly outcrop on the eastern side of the basin and in sparse tectonic windows beneath the Monti

della Maddalena thrust-sheet along the western side.

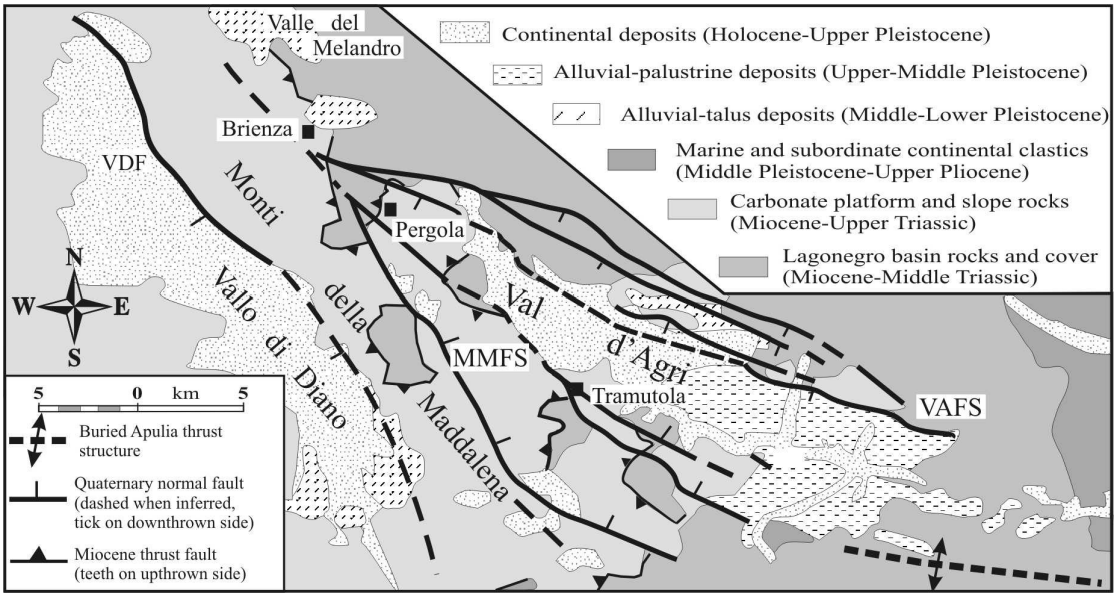

Fig. 1-6. Schematic geologic map of the Val d'Agri area showing distribution of the Quaternary oblique and normal faults. VDF=Vallo di Diano Fault; MMFS=Monti della Maddalena Fault System; EAFS= Eastern Agri Fault System (from Maschio *et al*., 2005).

Conversely, limited outcrops of the carbonates are found east of the basin where the leading edge of the thrust sheet is located (fig. 1-6).

Quaternary deposits are represented by Lower-Middle Pleistocene slope breccias deposits ("Galaino and Marsico breccias" Di Niro & Giano, 1995), Middle-Upper Pleistocene alluvial-lacustrine sediments ("Complesso Val d'Agri", Di Niro *et al*., 1992) and Upper Pleistocene-Holocene alluvial deposits (fig. 1-6).

The genesis and evolution of the basin is linked to the activity of two main fault systems bordering the valley. Its structural evolution can be summarized into two main steps (Giano *et al*., 2000). During Early-Middle Pleistocene the opening of the basin was controlled by N120° trending, left-lateral transtensive faults located along the eastern border of the valley (Turco and Malito, 1988; Cello *et al*., 2000, Giano *et al*., 2000). The left-oblique transtension was responsible for the accumulation, tilting and uplift of the slope breccias deposits and for the deposition of alluvial to lacustrine sediments.

Starting from Middle Pleistocene, the pre-existing structures were reactivated with a normal-faulting kinematics and newly formed normal faults contributed to the basin widening and deepening (Giano *et al*., 2000; Maschio *et al*., 2005). During Quaternary, subsidence in the basin was accompanied by a generalized uplift of the area at 0.6 mm/a (Schiattarella *et al*., 2003;

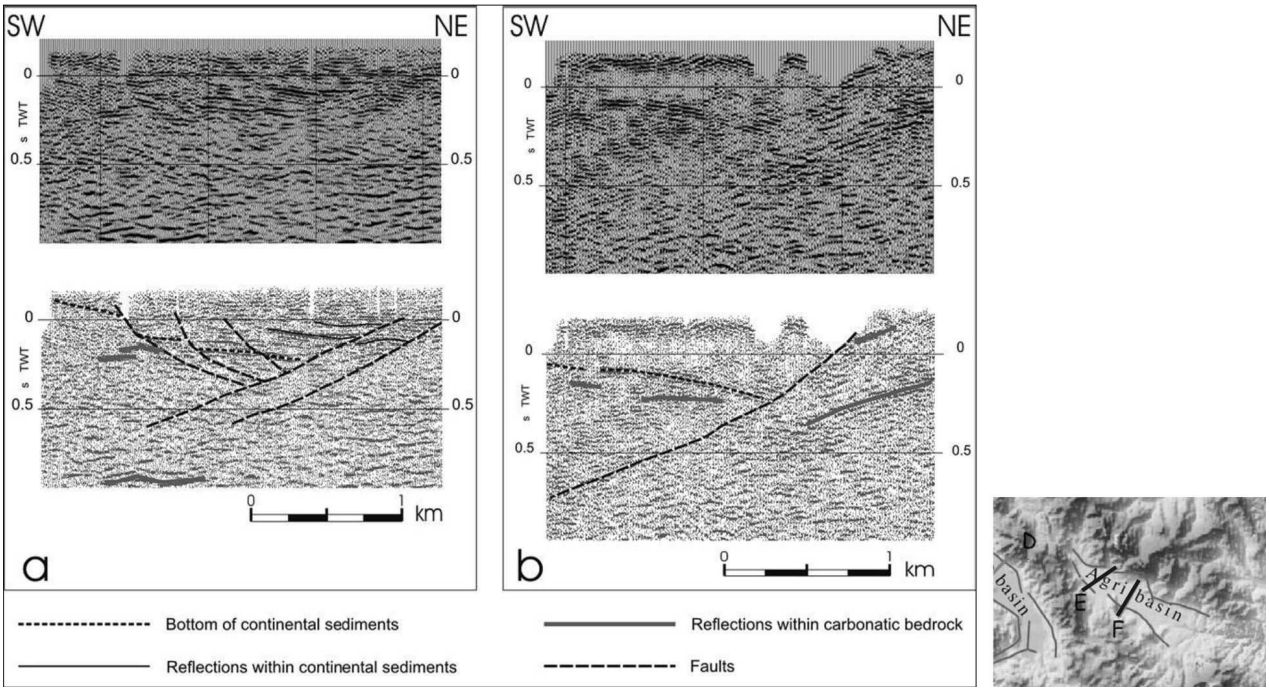

Fig. 1-7. Seismic reflection profiles through the Agri basin, sections a=E and b=F are located in the map on the left (from Barchi *et al*., 2007).

Boenzi *et al*., 2004). The deformation is testified by seismic activity and by loose slope deposits and paleosoils involved in faulting in the last 40 ka (Giano *et al*., 2000, D'Addezio *et al*., 2006, Ferranti *et al*., 2007).

Quaternary and active fault systems

The deep architecture of the basin and the geometry of the fault systems in the area have been mainly investigated by morpho-tectonic and structural studies (Cello *et al*., 2000-2003; Mazzoli *et al*., 2000, Maschio *et al*., 2005), macroseismic data (Branno *et al*., 1983), as well as seismic and geoelectrical surveys (Morandi and Ceragioli, 2000; Borraccini *et al*., 2002; Colella *et al*., 2004). Nonetheless, the internal structure of the basin and the geometry and kinematics of the active fault systems bordering the valley are discussed and even the seismogenic source responsible for the 1857 Basilicata earthquake is still debated (Benedetti *et al*., 1998; Cello *et al*., 2003; Maschio *et al*., 2005; Burrato and Valensise, 2007). Conventional seismic reflection profiles (Barchi *et al*., 2006), acquired to image the top of the Apulia platform at about 3 km depth, poorly image the shallow basin structure (fig. 1-7). The sections in fig. 1-7 indicate throw of some hundreds meters on fault located along the eastern side of the basin, and commonly do not show faults on the western side. Furthermore, seismic and electrical tomographies (Morandi and Ceragioli, 2002; Colella *et al*., 2004), even furnishing important insights on the basin structure, do not provide high-resolution images of

the faults geometry at depth. Finally, geomorphologic and structural data are not univocally interpretable (Benedetti *et al*., 1998; Giano *et al*., 2000; Cello *et al*., 2000-2003; Mazzoli *et al*., 2000, Maschio *et al*., 2005).

About the active fault systems in the basin there are 2 different hypothesis:

- Many Authors suggest the SW-dipping faults, well-exposed along the northern flank of the basin, as the surface expression of a local seismogenic source (Benedetti *et al*., 1998; Cello and Mazzoli, 1999; Cello *et al*., 2000-2003, Barchi *et al*., 2007). This fault system is known as Val d'Agri Fault System (VAFS, Cello *et al*., 2000-2003) or Eastern Agri Fault System (EAFS, Maschio *et al*., 2005).
- The second hypothesis proposes a NE-dipping normal fault system as playing the main role in controlling the recent tectonic activity in the area. This fault system, studied by means of structural and geomorphological data by Maschio *et al*., (2005), is located along the western flank of the basin (Monti della Maddalena Fault System; MMFS hereinafter). Its activity probably started during Middle Pleistocene with Late Pleistocene-Holocene activity confirmed by paleoseismological trenching (D'Addezio *et al*., 2006) and high-resolution shallow seismic (Improta and Bruno, 2007).

Cello *et al*. (2000-2003), by means of remote sensing analyses, geological mapping and structural field work, accurately describe the geometry and kinematics of the EAFS (fig. 1-8). This faults system has a clear geomorphic expression and is composed by 120°N-trending left-lateral strike-slip faults and their conjugate N30 trending right-lateral transtensional faults, and other related N90-N110 and N130-N150 trending left-lateral transtensional and transpressional faults. At the surface, the fault system is composed by five main strands showing rectilinear traces, spaced about 1 km apart, and associated with mature fault-line scarps (fig. 1-8). The total length of the fault system is more than 25 km; but no detailed definition exists (Gambini, 2003). Fault kinematics analysis indicate a main left oblique-slip episode, with a lateral displacement in excess of 1 km (Gambini, 2003), followed by a second normal component event observed on the lowermost fault strands with displacement of about 500 m (Barchi *et al*., 2006). The latter are thus reactivated with normal kinematics (Maschio *et al*., 2005) and a paleosoil (≈32 ka, Giano *et al*., 2000) was faulted in response to this second slip episode.

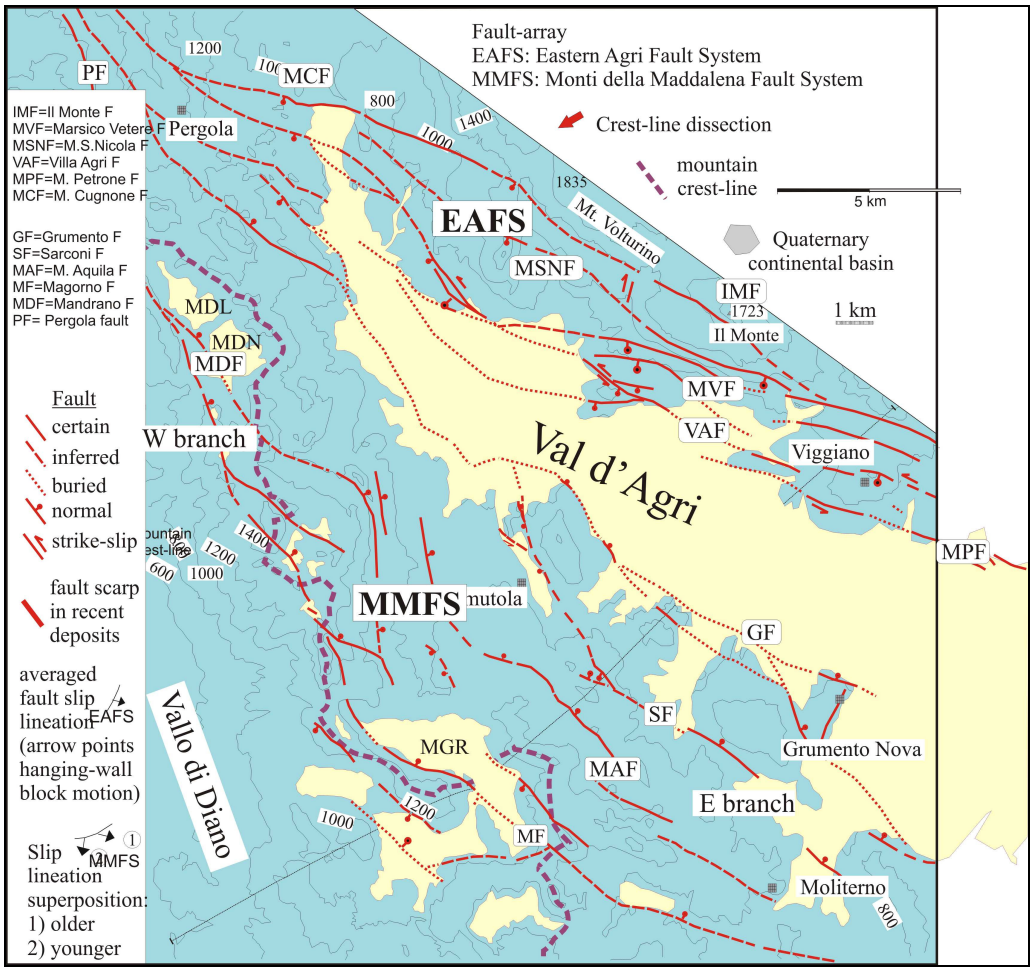

Fig. 1-8. Morphostructural map of the Agri basin showing the main quaternary fault systems.

On the basis of these evidences Cello *et al.* (2000-2003) believe this fault system as responsible of the genesis and of the structural evolution of the basin. Furthermore, they consider the EAFS the surface expression of a seismogenic structure that could be responsible of the major seismicity of the area. Other authors such as Benedetti *et al.* (1998), Michetti *et al.* (2000) and Barchi *et al.* (2006) share this hypothesis.

On the other hand, other Authors (Valensise and Pantosti (2001); Maschio *et al.*, 2005; Burrato and Valensise, 2007) on the basis of geomorphological and historical data, and according to geometrical and kinematic affinities with the seismogenic source for the 1980 M6.9 Irpinia earthquake, suggest that the NE-dipping normal fault system, located along the western side of the valley, is the most probable source for the historical and ongoing seismic activity of the area (MMFS, Maschio *et al.*, 2005).

The MMFS is accurately described from a geometric and kinematic point of view by Maschio *et al.* (2005). This fault system runs for about 25 km between the Pergola and Moliterno villages. The northern boundary is not well constrained, thus the MMFS could run further

northward reaching a maximum length of 35 km. The system can be divided into two main branches (fig. 1-8). Fault kinematic data reveal a prominent normal component of slip. Late Pleistocene and Holocene deposits are involved in faulting along the eastern branch of this fault system (D'Addezio *et al.*, 2006, Improta & Bruno, 2007).

The MMFS shares several geometric and morphologic features with the Irpinia fault: they have a comparable length (22-35 km for the MMFS and 38 km for the Irpinia fault); the average extensional axis is 30°N-40°NE consistent with the 33°NE seismological tensile axis of the Irpinia fault (Harvard CMT Catalogue data). Finally, as the Irpinia fault, this fault system is associated with a subtle geomorphic expression, which is indicative of small cumulative displacements along the faults.

Historical and instrumental seismicity

The most destructive event recorded in the Val d'Agri basin is the 1857 earthquake with equivalent magnitude 7.0 and maximum intensity in the Mercalli-Cancani-Sieberg (MCS) of XI grade (Mallet, 1862; Branno *et al.*, 1983; Boschi *et al.*, 2000). The earthquake consisted of two shocks. The damage distribution associated indicates the Agri valley as the most damaged area enclosed in the X-XI isoseismal line. Other important historical seismic events occurred in 1651 (Me=6.5, Vallo di Diano earthquake) at the north-western end of the Agri basin, in 1694 (Me=6.9) close to the Irpinia epicentre and in 1836 (Me=6.3) south of the Val d'Agri basin (fig. 1-9).

Instrumental seismicity recorded by the Italian permanent seismic network (RSNC) of INGV between 1984-2004 (Chiarabba *et al.*, 2005) shows dense cluster of earthquakes related to the four main seismic sequences that occurred in the recent period, namely the 1980 M6.9 Campania-Basilicata earthquake, the Potenza 1990 Md=5.5 and 1991 Ml=5.2, the 1996 Irpinia Ml=4.9 and the 1998 Castelluccio Md=5.5, all localized out of the study area. Most of the large and moderate magnitude earthquakes are located between 5 and 15 km depth and display an extensional focal mechanism.

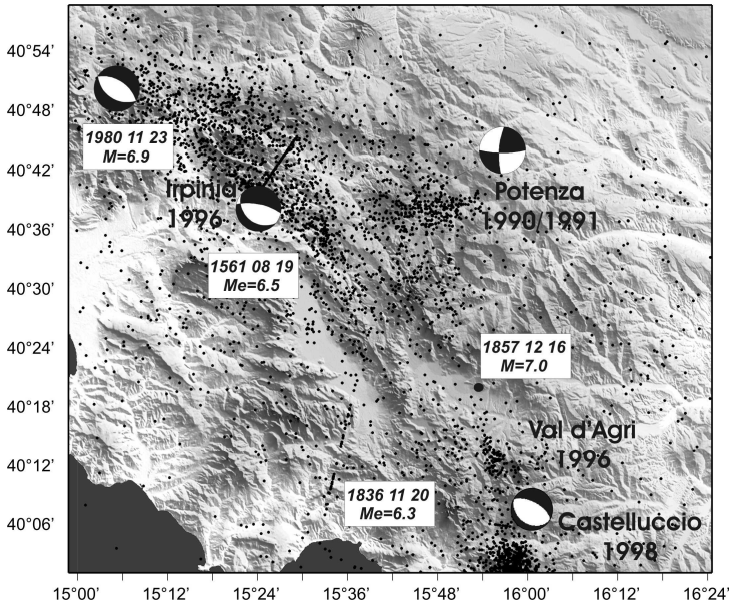

Fig. 1-9. Seismotectonic framework of the lucanian Apennines; small black dots represent the instrumental seismicity of the last 20 years (Chiarabba *et al.*, 2005); white boxes are the historical earthquakes from CPTI working group. Focal mechanism solutions are from Harvard CMT catalogue and Gasparini *et al.*, 1985. The macroseismic epicentre of the 1857 Basilicata earthquake is also shown by a large black dot.

The 1990 and 1991 Potenza events are the only significant exception to this behaviour, showing almost pure strike-slip mechanism and greater hypocentral depth (e.g. 26 km for the 1990 event, see Azzara *et al.*, 1993). These fault plane solutions are consistent with the direction of regional extension for this area as resulting from borehole breakout data (Amato and Montone, 1997, Cucci *et al.*, 2004). T-axes are usually NE-SW and E-W oriented.

The most significant seismic sequences occurring in the Val d'Agri basin during last 20 years was recorded between 3 April and 12 June 1996 and is described by Cucci *et al.* (2004). The sequence is localized along the south-western flank of the Val d'Agri basin and consists of 50 low-magnitude events, with magnitude in the range $1.8 \leq Md \leq 3.4$. Ipocentral locations errors are as large as 2.5 km and do not allow to image an active structure (Cucci *et al.*, 2004).

Chapter 2

The Agri valley seismic network

Introduction

In this chapter I present hypocentral locations of the background seismicity recorded by a dense seismic network installed in the Val d'Agri area. Furthermore, focal mechanisms of selected events and the seismic behaviour in term of seismic release with time are shown.

The use of a dense local seismic network allows the lowering of the minimum magnitude threshold for earthquakes detection. This is a pre-requisite to investigate seismic activity around known active faults and possibly to define their geometry at depth and their kinematics.

The Agri seismic experiment

During May 2005 to June 2006 a dense temporary seismic network, composed by up to 23 continuously recording stations, was operating in the axial sector of the Lucanian Apennines. The seismic network covers an area of about 1500 km^2 including the Val d'Agri basin, partially the Vallo di Diano basin and the Monti Alpi (fig. 2-1). The average receiver spacing is about 5 km. The temporary network was complemented by seismic stations of both the ENI permanent network (13 stations recording on trigger mode) and the Italian National Seismic network (fig. 2-1).

The stations were equipped with different digital acquisition systems (Reftek130 and Marslite88) and three-component short and long period seismic sensors (Lennartz 3D 1s and 5s, and Nanometrics Trillium 40s). Three stations were also equipped with strong motion sensors. The stations were continuously recording on a flash card (2 Gb) at a sampling rate of 125 Hz per channel, in order to have a good sampling for local events. Solar panels were used to power the instruments and a GPS antenna provided the absolute timing for the recording. The stations were located preferentially on rocky outcrops and the background noise level was studied in order to select sites characterized by an high signal-to-noise ratio. The stations were visited once every 45 days for data collection and servicing.

In order to extract local earthquakes from the continuously recorded data a trigger algorithm was applied. The algorithm is based on the *Sta/Lta* ratio (Short time average/Long time average; Piccinini *et al.*, 2003). After performing numerous tests the following values for trigger parameters were chosen: *Sta/Lta* ratio 3; *Sta* 2s; *Lta* 40s; *duration* 2s. A minimum number of 4 stations was imposed to declare a trigger coincidence. The chosen setting,

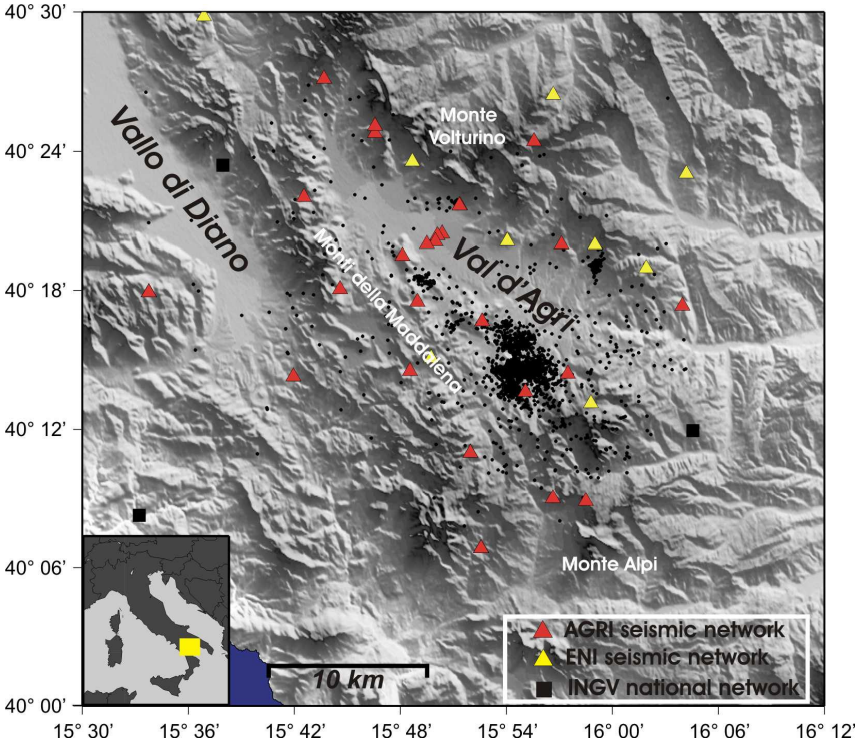

Fig. 2-1. Map showing the Agri seismic network (red triangles) and about 2000 seismic events recorded during the experiment. Black squares are stations of the Italian national seismic network and yellow triangles of the ENI permanent network.

together with the very dense geometry of the seismic network, allowed to achieve a very low magnitude earthquake detection (M_L>-0.19) with a small number of false events. In thirteen months, from the continuously recorded data, about 4000 triggered events were extracted, testifying a high rate of background seismic release.

Data analysis

At first the dataset of about 4000 micro-earthquakes was analysed by an automatic *P*-wave picking procedure in order to obtain preliminary hypocentral locations. In the ensuing phase, about 700 well-located events were selected (i.e. events affected by very small hypocentral location errors and RMS values) to verify the *P*-wave automatic readings and to hand-pick *S*-wave arrival times.

Automatic P-wave picking

In the first stage of the dataset analysis, a recently developed picking system called *MannekenPix* (Aldersons, 2004; Di Stefano *et al*., 2006), capable of producing highly accurate first arrival *P*-wave picks and related polarities, was applied. In the last years

MannekenPix has been used, with successful results, to pick *P*-wave arrivals on a large dataset of local and regional events recorded by the Italian National Seismic Network (Di Stefano *et al.*, 2006). The application of this automatic procedure to the very low-magnitude dataset recorded by the dense Agri seismic network has also a test-meaning.

The advantages of using a very accurate automatic picking procedure are:

- A low time-consuming preliminary analysis of the dataset
- Highly accurate first-arrival *P*-wave picks and related polarities
- Consistency in timing error assessment

MannekenPix was calibrated on a reference dataset of about 700 waveforms (from 120 seismic events of the Agri experiment) that were accurately hand-picked and quality-weighted following the scheme shown in table 1. In this calibration phase, the system defines an observation weighting scheme. When the calibration phase is completed, the picker system is able to mimic the picking by a human analyst. Furthermore, the phase readings have a consistency in data error assessment. This point is of primary importance because the estimated average observation error (i.e. the noise level in the data) normally defines the termination of the iterative inversion process of seismic tomography and hypocenters calculation (Di Stefano *et al.*, 2006). This picking procedure is based on a single trace approach (Allen, 1978-1982) that picks each seismogram independently from the others, according to the great variety of waveforms observed. The result obtained by the use of this automatic picking system was very successful since most of the about 20000 *P*-phase automatic readings are comparable to those of a good human analyst.

The application of this procedure allowed the preliminary location of about 4000 low-magnitude seismic events. The figure 2-1 shows 1991 seismic events identified by RMS time residuals less than 1 s, azimuthal gap less than 200°, hypocenters formal errors less than 2 and 3 km horizontally and vertically respectively, and at least 4 *P*-wave readings, located by using HYPOELLIPSE code (Lahr, 1989).

Hypoellipse class	Picking uncertainty (sec)
0	0 - 0.025
1	0.025 - 0.050
2	0.05 - 0.4
3	> 0.4

Table 1. Weighing scheme followed for the phase reading on the waveforms.

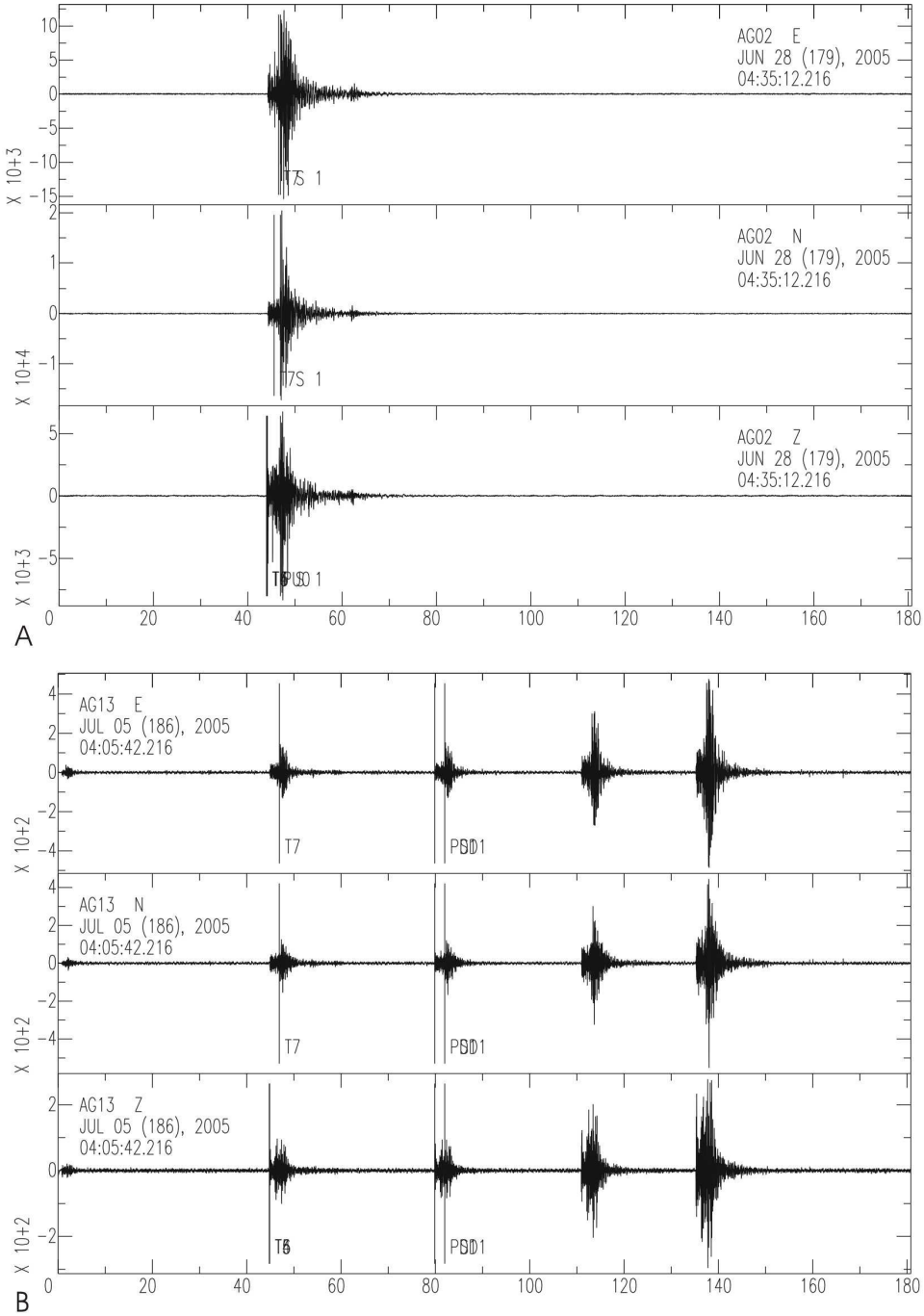

Fig. 2-2. Three-component waveforms recorded by the Agri seismic network. A) local earthquake recorded at the AG02 station (M_L=2.33) b) example of multiple event (0.22<M_L<1.28).

From the dataset analyzed by the automatic picking procedure, about 700 events were extracted to verify *P*-wave readings and to hand-pick *S*-wave arrival times to better constrain hypocentral locations. The selection was made according to these parameters: RMS time residuals less than 1 s; vertical location error less than 2 km; horizontal location error less than 1 km; more than 8 *P*-wave readings.

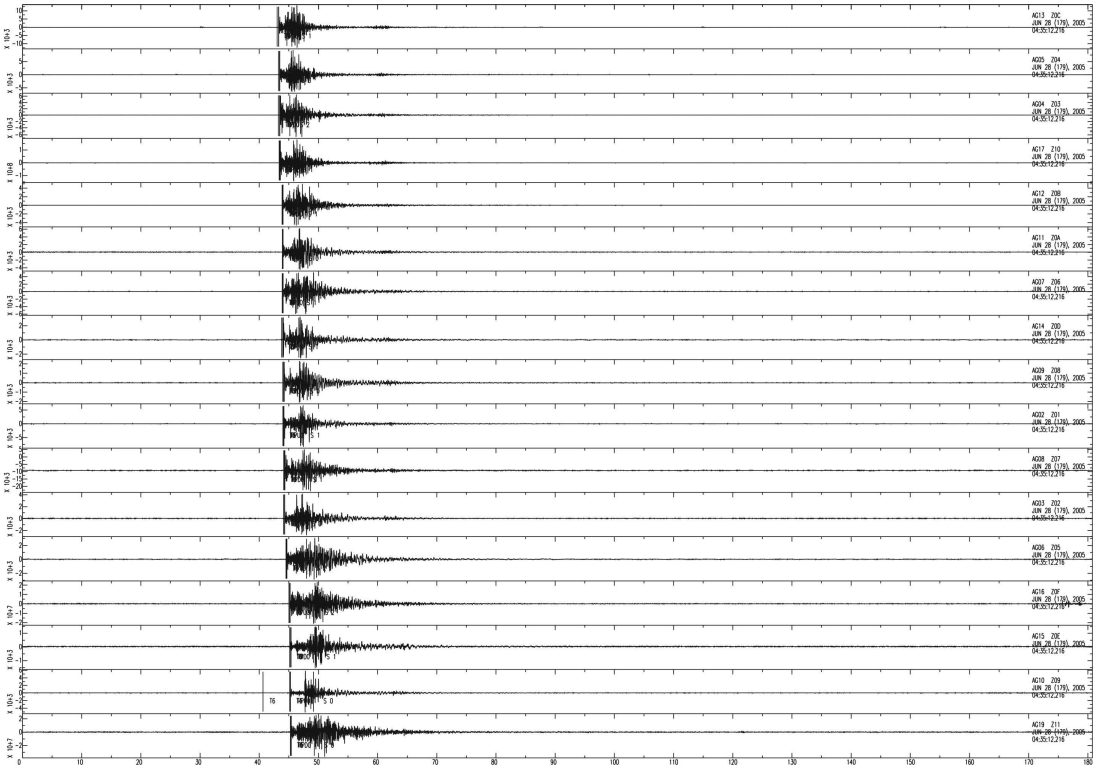

Fig. 2-3. Vertical component seismograms of the 28th June 2005 local earthquake. P-phase first arrivals are marked with a vertical bar.

In addiction, in order to avoid an over-sampling of limited areas, where a high number of low-magnitude earthquakes are located, a spatial selection was applied.

The final dataset consists of 678 seismic events (fig. 2-6) with a final number of *P* and *S* readings of 9571 and 8933, respectively. This dataset has been used for the 1D velocity model computation and magnitude estimation. These events are characterized by location RMS values less than 0.3 s, azimuthal gaps smaller than 200° and horizontal and vertical errors less than 0.5 km (fig. 2-3).

1-D model selection

The influence of 1-D (one-dimensional) velocity model on earthquake location is severe. Therefore, it is very important to reach a global minimum in the model space, avoiding to remain trapped within secondary minima. For these reasons, the one-dimensional (1D) velocity model of the area was computed by applying a non-linear inversion technique based on genetic algorithms (Sambridge and Gallagher, 1993; Kim *et al.*, 2006).

Genetic algorithms are a global search algorithm particularly suitable to solve highly non-linear and non-local optimization problems.

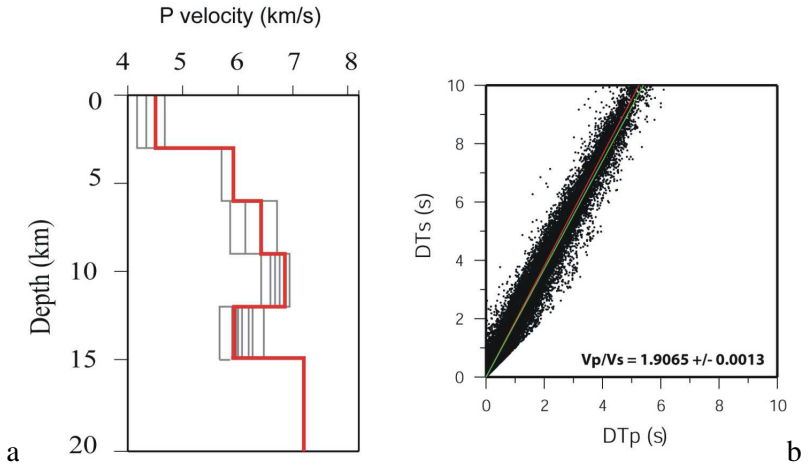

Fig. 2-4. (left) *P*-wave best velocity model (thick red line). Grey lines are models with misfit value below 0.1077s; (right) Wadati diagram: the computed *Vp/Vs* ratio is equal to 1.90.

Despite of other linearized iterative methods (i.e. Velest code, Ellsworth, 1977; Kissling *et al.*, 1994) that require the introduction of a-priori information, through the definition of a starting model, the genetic algorithms do not need any derivative information (Sambridge and Drijkoningen, 1992). These global search algorithms seek in the entire model space the 1D model which minimizes the misfit between the time spent by seismic waves through the candidate model, and the observed traveltimes. HYPOELLIPSE code was used to perform the forward modelling. The search technique is based on three operators: selection, crossover and mutation. These operators act together on the first generation of the population (i.e. velocity models) to produce a new population and to re-direct the solution towards a better one. Velocity values of the initial velocity models are randomly generated while the layers thickness was set at 3 km. The population size (i.e. number of velocity models) was chosen at 300 individuals and at 300 the number of iterations. When the 70% of the generated velocity models has an individual global misfit (e.g. global RMS residuals) less than 0.1077 s, the genetic code ends the search.

Figure 2-4a shows the best-fit 1D *Vp* model with the minimum misfit value (thick line) and other *Vp* models having misfit values smaller than 0.1077 s (thin lines). The model is made of 5 layers with a 3 km thickness. Table 2 shows *P*-wave velocity values and thickness of the best 1D model.

The computed *Vp* model is consistent with *P*-wave velocities found for rocks composing the Apennines as defined by velocity logs and laboratory measurements (Improta *et al.*, 2000).

Layer	Depth to the layer top	Velocity (km/s)
1	0-3	4.33
2	3-6	5.92
3	6-9	6.42
4	9-12	6.85
5	12-15	5.93
6	> 15	7.0

Table 2. 1D Vp velocity model obtained by genetic algorithm inversion.

P-wave velocities increase up to 12 km depth with values in the range 4.33 km/s and 6.85 km/s; further below (from 12 to 15 km depth) a lower *P*-wave velocity (5.93 km/s) indicates a velocity inversion. The velocity retrieved for the upper layer (4.33 km/s) can confidently represent an average of the velocities of the heterogeneous terrains outcropping in the area (Menardi Noguera and Rea, 2000, Shiner *et al*., 2004). This velocity value is also constrained by *P*-wave velocity models calculated, through first-arrival traveltimes tomography, for the shallow crustal structure (down to 2 km depth) of the Agri basin (see chapter 3 for an exhaustive treatment).

From 3 to 9 km depth, the model shows *P*-wave velocities between 5.92 and 6.42 km/s. These values (≈ 6 km/s) are compatible with the *P*-wave velocities observed by seismic refraction profiles and subsurface data, which have been associated to the Mesozoic limestone of the Apulia Carbonate Platform (Improta *et al*., 2000).

Following the interpretation by Improta *et al*. (2000) the high *Vp* (6.85 km/s) found between 9 and 12 km depth, are compatible with the deeper portion of the Apulia Platform consisting of Upper Triassic dolomites and anhydrites of the Burano formation.

In correspondence with the deepest layer, between 12 and 15 km depth, a decrease of the *P*-wave velocity is observed (*Vp* ≈ 5.9 km/s). This layer can be tentatively associated with Permo-Triassic clastic deposits, equivalent to those drilled by two deep wells in the foreland area at the base of the Apulia Platform (Puglia 1 well and Gargano 1 well) (Improta *et al*., 2000; Mazzoli *et al*., 2001; Shiner *et al*., 2004). However, this velocity inversion is not well constrained because of the decreasing data density beneath this layer.

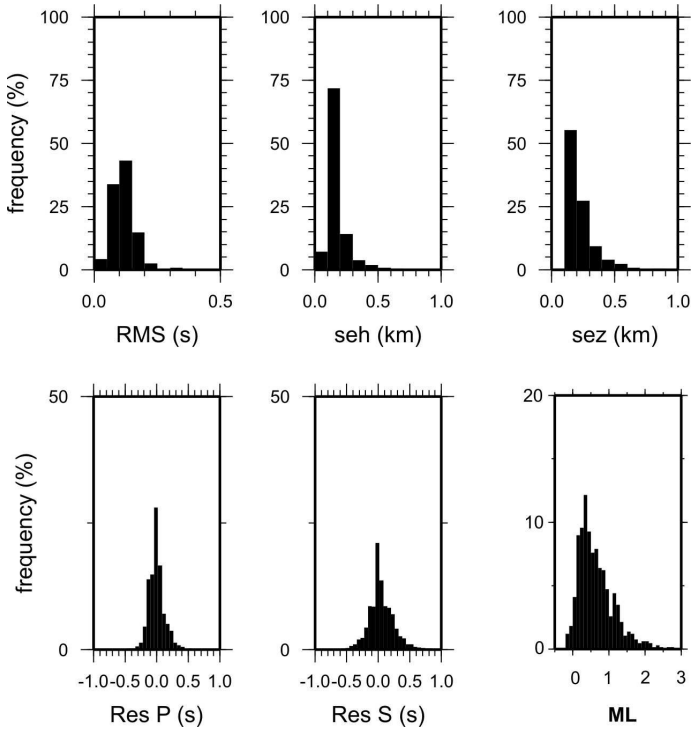

Fig. 2-5. Histograms showing the residuals (seconds), horizontal and vertical formal errors (km), *P*- and *S*-phases residuals and magnitude for the selected dataset.

The mean *Vp/Vs* ratio for the study area was computed by using a cumulative Wadati diagram (Lay and Wallace, 1995). The obtained value is 1.90 (figure 2-4b). This value is higher with respect to *Vp/Vs* ratio reported in literature for adjacent regions (1.82 *Vp/Vs* value computed by Frepoli *et al*. (2005) over a wider area of the Lucanian Apennines), but in agreement with other seismic zones of the Apennine chain (e.g. Umbria-Marche seismic zone; Chiarabba and Amato, 2003).

The *local magnitude* for 657 selected events was estimated following the formulation originally proposed by Richter (1935, 1958) and subsequently modified and adapted to the Italian area (Piccinini *et al*., 2003; Console *et al*., 2006).

Following the method originally used by Richter, M_L is given by:

$$M_L = LogA - LogA_0 - S$$

where A is the maximum trace amplitude in millimetres measured from a Wood-Anderson seismogram, A_0 is a distance dependent attenuation curve, and S is a station dependent M_L adjustment.

Assuming a parametric form for Log A_0 proposed by Alsaker *et al*. (1991) and derived by Bakun and Joyner (1984) the formula becomes:

$$M_L = \text{Log } A + n^* \text{ Log } (R/R_{ref}) + (-k^*(R-R_{ref})) - V(R_{ref})$$

where A is the maximum trace amplitude in millimetres measured on the seismogram (i.e. the maximum *S*-wave amplitude), R is the epicentral distance (in km), *n* and *k* are parameters related to geometrical spreading and attenuation of the *S*-waves and are dependent to the study region. R_{ref} is the reference distance and the $V(R_{Ref})$ is the reference magnitude value corresponding to R_{ref} (Piccinini *et al*., 2003). In our case, the two constants *n* and *k* have been recently calculated for the Italian area by Console *et al*. (2006) resulting in *n* equal to 1.11, *k* equal to -0.00189. R_{ref} has been set equal to 100 km and $V(R_{ref})$ is equal to 3.

The maximum trace amplitude was measured on waveforms from a Wood-Anderson instrument, obtained by subtracting the seismometer and digital station response from our seismograms. The maximum amplitude was measured after rotating each horizontal seismogram to the radial and transverse components.

The magnitude for each of the horizontal seismometers is averaged in a least-squares sense to give a M_L for a given station. The values of M_L for each station are averaged to give the magnitude. M_L may vary considerably from station to station, due not only to station corrections but also to variability in radiation pattern.

Local magnitudes range between -0.19 and 2.74 while the completeness threshold is about 0.4 (fig. 2-5). The detection of such a small magnitude events was allowed by the very dense station array used in the area and by the selection of sites characterized by a high signal to noise ratio.

Space and time seismicity distribution

Fig. 2-6 shows map and vertical section views of the selected 678 earthquakes. Seismicity is preferentially located along the south-western flank of the basin, highlighting a NW-SE trending zone, about 20 km long and 5 km wide, characterized by a very large number of low-magnitude seismic events (fig. 2-6, vertical sections 7 to 12). Elsewhere, the seismicity is scarce and sparsely distributed through the entire area. Only two small clusters are located along the western and eastern side of the basin, respectively (fig. 2-6, vertical sections 3 to 6).

Seismicity distribution versus depth (histogram in fig. 2-6) delineates a 12 km thick seismogenic layer, also recognizable in the two main cross-sections (vertical sections 1 and 2 in fig. 2-6) comprising all the recorded seismicity.

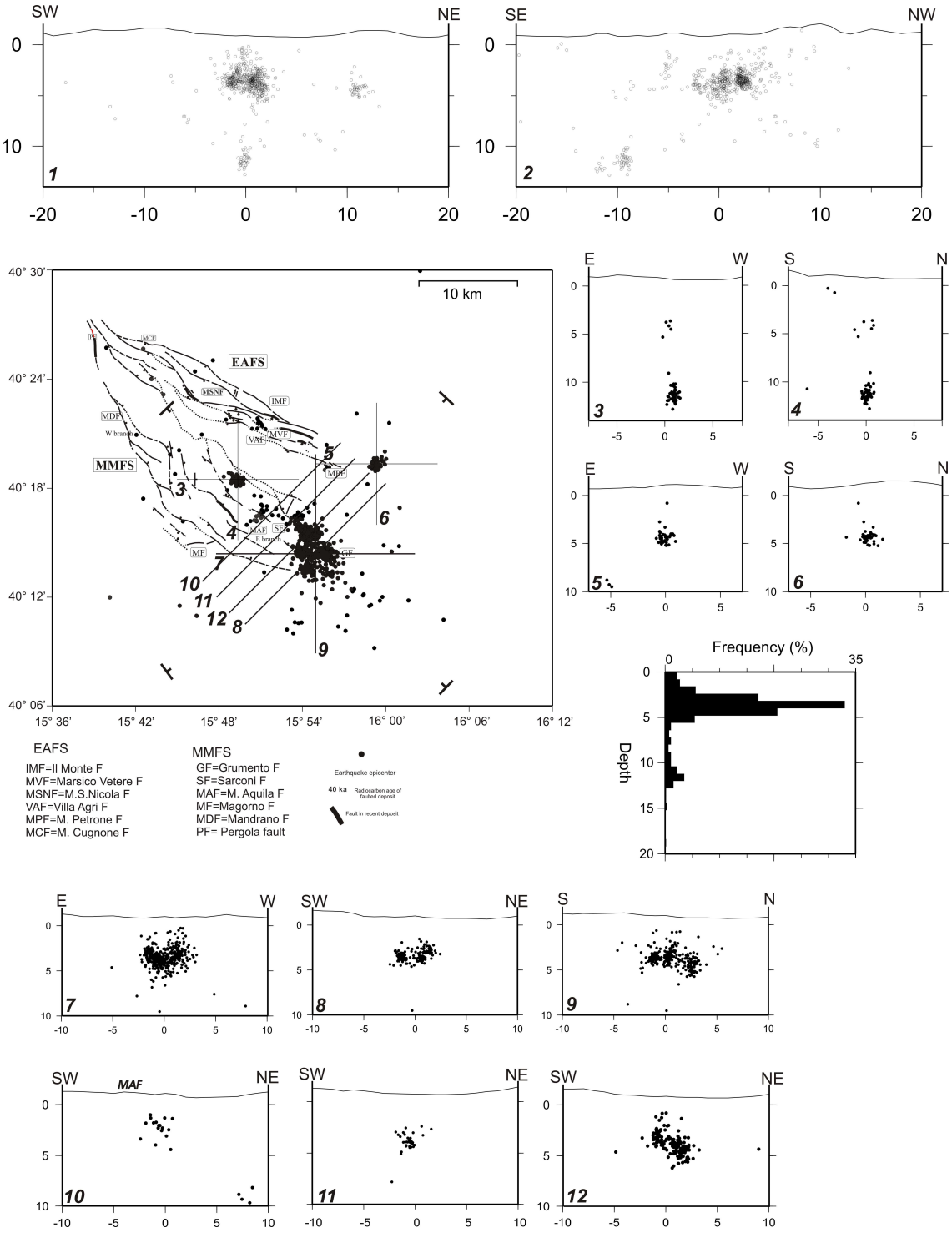

Fig. 2-6. Map and cross-section view of the selected 678 seismic events. The Apenninic and anti-Apenninic vertical cross-sections (1 and 2) comprise all the earthquakes shown in map. The small cross-sections (3, 4, 5 and 6) show hypocentral locations for events related to the two small clusters located along the western (sections 3 and 4) and eastern (sections 5 and 6) side of the basin. The other cross-sections (7 to 12) show hypocentral locations for the events of the main cluster located along the south-western border of the basin. The detailed location of the main Quaternary fault systems is also shown (modified from Maschio *et al*., 2005).

The histogram shows a bi-modal distribution: about 90% of the recorded seismicity is confined within the shallow crust between 2 and 6 km depth, while the main contribution to the deeper peak derives from the cluster located along the western side of the basin with hypocenters in the range 10-13 km depth (fig. 2-6, sections 3-4). This distribution underlines the presence of a layer between 6 and 10 km depth, where the seismic release is almost absent.

Most of the seismic events are located in the southern portion of the basin defining an area of about 5x10 km^2 in plant with hypocenters located between 2 and 6 km depth (fig. 2-6, sections 7 to 12). Although at a first look hypocenters seem arranged in a quite chaotic way, without enlightening any fault geometry, the NE-striking cross-sections 8, 10, 11 and 12 suggest the presence of a 50 to 60° NE-dipping structures that limit hypocenters to the bottom. However, the occurrence of a large number of low-magnitude seismic events in this volume suggests that seismicity occurs on small fractures spread all over the volume rather than preferentially clustered along a fault plane.

The remaining seismic events recorded during the experiment are clustered in two small volumes (fig. 2-6, sections 3 to 6). The first one is located along the north-eastern flank of the valley and is made of about 50 seismic events with magnitude in the range $0.19 < M_L < 1.75$ located between 4 and 6 km depth (fig. 2-6, sections 5-6). The other cluster, made of about 40 seismic events with M_L between 1.02 and 2.11, is located along the western flank of the valley. This cluster, with hypocenter locations between 10 and 13 km depth, represents the only deep seismicity recorded over the thirteen months of experiment (fig. 2-6, sections 3-4). The cross-sections 3 and 4 show that deep events are preferentially distributed along a vertical plane.

Fig. 4-7 shows the plot of the cumulative number of events versus time (black line) respect to the number of events per day versus time (gray line). The resulting figure allows to make same consideration about the rate of seismic release over time. In the Val d'Agri area the rate of seismic release is quite high (about $3.3*10^{-3}$ events/day/km^2, computed considering 2000 events recorded in 13 months over a 1500 km^2 area) and almost continuous in time (i.e. the black curve in fig. 4-7 does not show any significant slope variation).

However, some steeper segments, corresponding to an increasing seismic release rate, highlighted by the three shaded coloured area are recognizable.

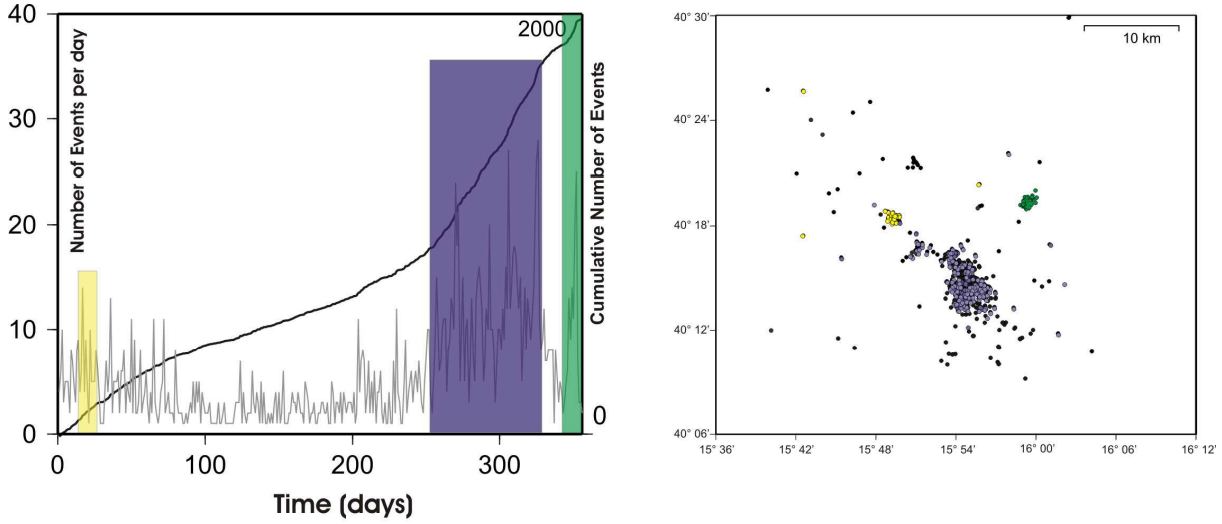

Fig. 2-7. (left) Cumulative number of events (black curve) and number of events per day (grey line) versus time. (right) Colour coded zoom of the main cluster zone.

It is possible to observe that the coloured areas correspond to the occurrence of the previously described main clusters. In particular, the yellow coloured area corresponds with the occurrence of the deep cluster along the western border of the basin while the green one is linked to the cluster located along the eastern border of the basin. So these small clusters are released in form of minor seismic sequences.

Finally, the broad violet dashed area highlights an increasing of the seismic release starting from March-April 2006 until the end of the experiment in July 2006, related to the main cluster located in the southern portion of the basin.

Focal mechanism computation

Focal mechanisms for 108 best-located events were computed by using the *P*-wave first motion polarity method using the FPFIT code of Reasenberg and Oppenheimer (1985) (the computed solutions are shown in appendix A). Quality factors QF and QP were chosen ranging between A and B, while the minimum number of *P*-wave polarities was set to 7. QF reflects the solution prediction misfit of the polarity data, while QP reflects the solution uniqueness in terms of 90% confidence regions on strike, dip and rake.

Fig. 2-8 shows 48 focal mechanisms selected from the computed 108, as representative of the highest magnitude events. Statistical analysis of the kinematics of the nodal planes shows that about 70 % of the focal mechanisms have a normal solution (fig. 2-8). In particular, about 45% are normal (rake between -60°/-120°) with about 7% of pure normal events.

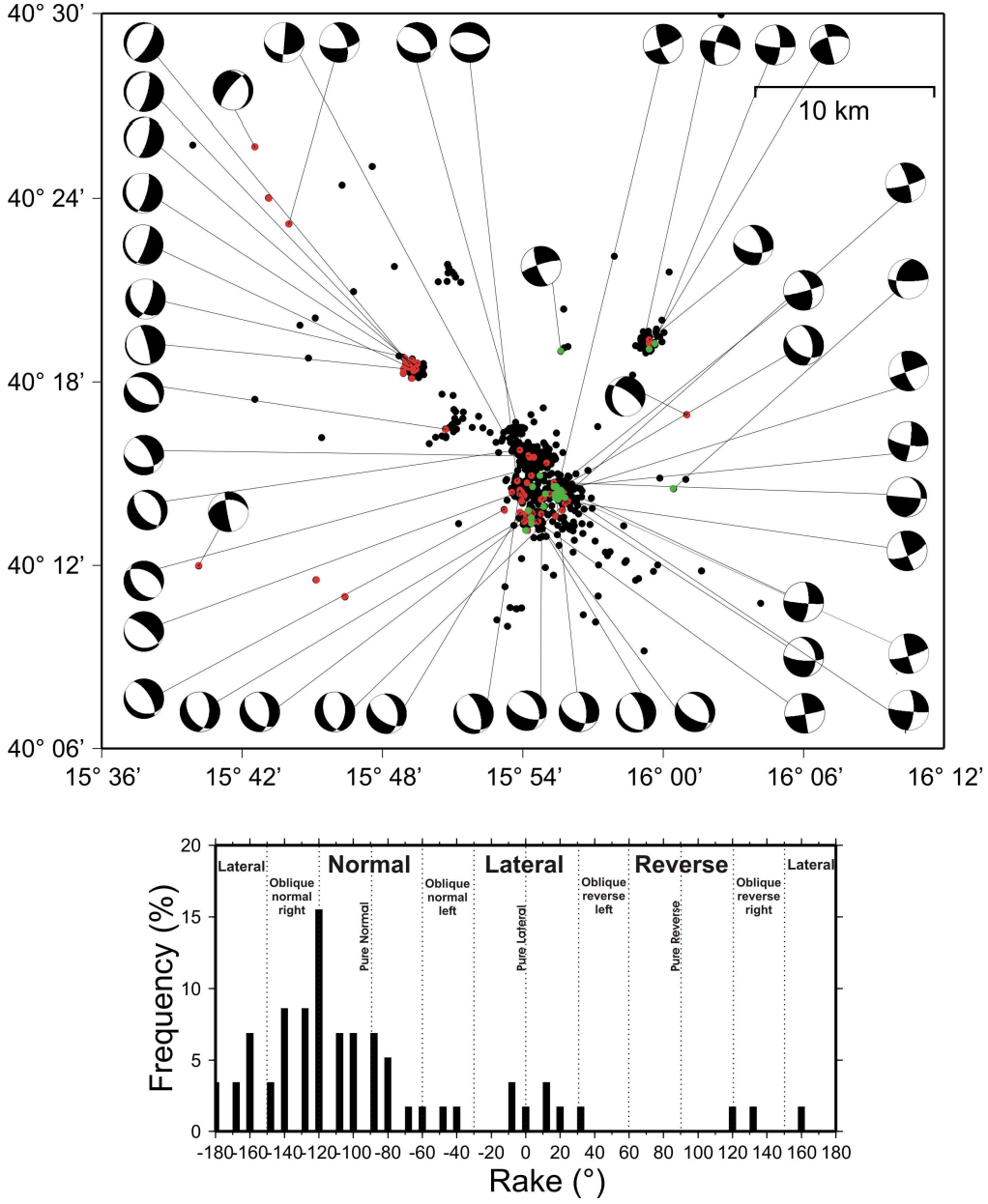

Fig. 2-8. (top) Map showing focal mechanism solutions for 48 selected seismic events. Red and green dots are for events with normal and strike-slip focal mechanism, respectively. (bottom) histogram showing rake values for the 108 computed focal mechanisms. Normal and trastensional kinematics dominate, whilst reverse components are almost absent.

About 23 % are oblique/normal with right or left lateral component. The remaining events are mostly left or right lateral and only 4% have reverse kinematics (see histogram in fig. 2-8). Most of T-axes are sub-horizontal (plunge < 40°) oriented about 50° toward NE. These solutions are in agreement with pseudo-focal mechanisms computed by fault slip inversion from surface exposures of fault planes (Maschio *et al.*, 2005 and also fig. 6 of chapter 4) and

with focal mechanisms of large earthquakes in the region (Cucci *et al*., 2004; Montone *et al*., 2004).

The focal mechanisms of the deepest cluster of events (focal mechanisms located along the upper left side of the map in fig. 2-8) show a dip-slip kinematics. Focal mechanisms for earthquakes belonging to the main cluster, located in the southern portion of the basin, show a prevailing normal component kinematics. However, some seismic events located in the right portion of the cluster show strike slip (right-lateral) kinematics (fig. 2-8).

Relation between seismicity and geological structures

The relation between the recorded seismicity and the main geological structures mapped at the surface (fig. 2-6, Maschio *et al*., 2005) is not straightforward.

Most of the seismicity located along the south-western side of the basin is spatially associated with the southern sector of the Monti della Maddalena fault system. The NE-trending vertical sections 7 to 12 in fig. 2-6 highlight that the low-magnitude seismicity is limited downward by an about 50° NE-dipping planes. In particular, in the section 10, earthquakes are aligned along a 50° NE-dipping plane, whose projection at the surface shows a good correspondence with a fault scarp in young deposits recently identified by means of geomorphological, geophysical and paleoseismological surveys (Monte Aquila Fault, Maschio *et al*., 2005, D'Addezio *et al*., 2006; Improta & Bruno, 2007). Furthermore, the earthquake hypocenters in the vertical sections 11 and 12 in fig. 2-6 are in agreement with other two small strands of the MMFS named Sarconi and Grumento fault, respectively. These structures could confine seismic release in the hanging wall of their fault planes. Meso-structural analysis for these structures indicates NW-SE striking and 55° to 65° NE-dipping fault planes characterized by a normal kinematics with a NE-oriented T-axes. These characteristics are in agreement with the focal mechanisms computed in this study (see focal mechanisms located along the lower left side of the map in fig. 2-8). However, it is worth noting that seismicity does not occur on fault planes at the depth where major earthquakes enucleate in the southern Apennines seismic belt.

Moving toward the eastern border of the basin, the seismicity is almost absent. No earthquakes have been recorded neither along nor around the main fault planes of the Eastern Agri fault system located along this side of the basin (fig. 2-6). The only small cluster is probably induced by oil extraction (fig. 2-6, sections 5 and 6).

The deep cluster of seismicity is hardly connected with a specific Quaternary or older structure in the basin. As shown by focal mechanism solutions (focal mechanisms located

along the upper left side of the map in fig. 2-8) these seismic events seem to be related to an about N20° sub-vertical fault plane characterized by a dip-slip kinematics. The choice of this nodal plane is suggested by the elongation of the seismic event on a vertical plane (fig. 2-6, sections 3 and 4). This deep seismicity does not show a straight linkage with the shallow seismicity recorded along the western flank of the basin. It could be probably related to the re-activation of inherited structures at the bottom or even below the Apulia platform.

Discussion

The background seismicity recorded during the thirteen months of the experiment (about 2000 earthquakes) testifies a high rate of seismic release with magnitude in the range -0.19 and 2.74. Most of these earthquakes concentrate in the shallow crust between 2 and 6 km depth beneath the south-western portion of the basin (fig. 2-6). These low-magnitude earthquakes reflect small fractures spread in a volume whilst only a small portion enlighten fault plane geometry at depth. The kinematics of these events show a preferentially normal component with NE-oriented T-axes.

It is worth noting that this volume is adjacent to the most significant seismic sequence occurring in the Agri basin during last 20 years, recorded between 3 April and 12 June 1996, described in the work of Cucci *et al*. (2004). The sequence, made up of 50 low-magnitude events, with magnitude in the range $1.8 \leq M_d \leq 3.4$, was localized along the south-western side of the Val d'Agri basin. Another small swarm occurred in the same area in 2002 (19 earthquakes with magnitude $M_d<2.8$; Frepoli *et al*., 2005). The characteristics of these small sequences are similar to those observed for the shallow seismicity described in this study.

These observations suggest the presence of active NE-dipping structures located along the south-western side of the Agri basin. However, as already stated, the hypocenter distribution do not allow to recovery the fault geometry at depth greater than 6 km. The small cluster of deep seismicity does not appear directly correlated to the shallower seismicity and, consequently, it does not represent a constraint for the prolongation of the small fault planes at greater depth. For its location this deep seismicity appear linked to the activity of deep structure at the base or even below the Apulia platform suggesting the activation of inherited structure at the base of the Apulia platform.

Therefore, although our data can not solve the worm debate about the seismogenic source responsible of the 1857 event, furnish incontrovertible constrains about the present tectonic activity of some segments of the MMFS improving the knowledge of the geometry at depth and kinematics of this fault system.

Chapter 3

High-resolution imaging of the Val d'Agri basin by controlled source crustal tomography

Introduction

In this chapter, I present new insights on the structural architecture of the Val d'Agri basin focusing on the Quaternary fault systems, by analysing two high-resolution seismic crustal profiles, about 15 km long, crossing the central sector of the basin (fig. 3-1). In the following chapter 4, these seismic profiles will be analysed together with results of detailed geological mapping carried out along the seismic profiles, in areas where the connection between surface geology and geophysics is particular critical (fig. 3-17 and figures in chapter 4).

Assessment of seismic hazard posed by active faults requires the accurate knowledge of numerous parameters, including the location, geometry, slip rate, recurrence interval and kinematics of recent fault movements. Although geological field surveys and paleoseismological trench studies can reveal much about these parameters, subsurface data are also necessary to understand the history and three-dimensional geometry of faults at greater depth (see Dolan & Pratt, 1997).

As described in first chapter, active fault systems in the Val d'Agri basin have been mainly investigated by field studies and commercial reflection profiles. However, even when commercial seismic reflection profiles are available, these data are not able to image, in detail, the shallow structure of the basin for the following reasons (e.g. Barchi *et al*., 2006).

First of all, the acquisition geometry and the processing sequence applied to commercial seismic profiles are aimed at imaging deep reflectors (the top of the Apulia Carbonate Platform). Consequently, the resolution of the time migrated stack sections does not allow the detailed imaging of the complex depositional structures of the basin and of small displacement newly formed active faults. Moreover, in thrust belt environments, on land seismic exploration may be hampered by the combination of extreme topographic variation, highly variable surface geology, complex velocity structures, which often lead to poor quality structural images. Data quality may be, indeed, strongly affected by diffraction/scattering phenomena, strong multiples and static problems, which are caused by small-scale heterogeneities and by rough topography (Mazzotti *et al*., 2000; Dell'Aversana *et al*., 2001). In such geological environments, alternative acquisition and processing strategies should be considered.

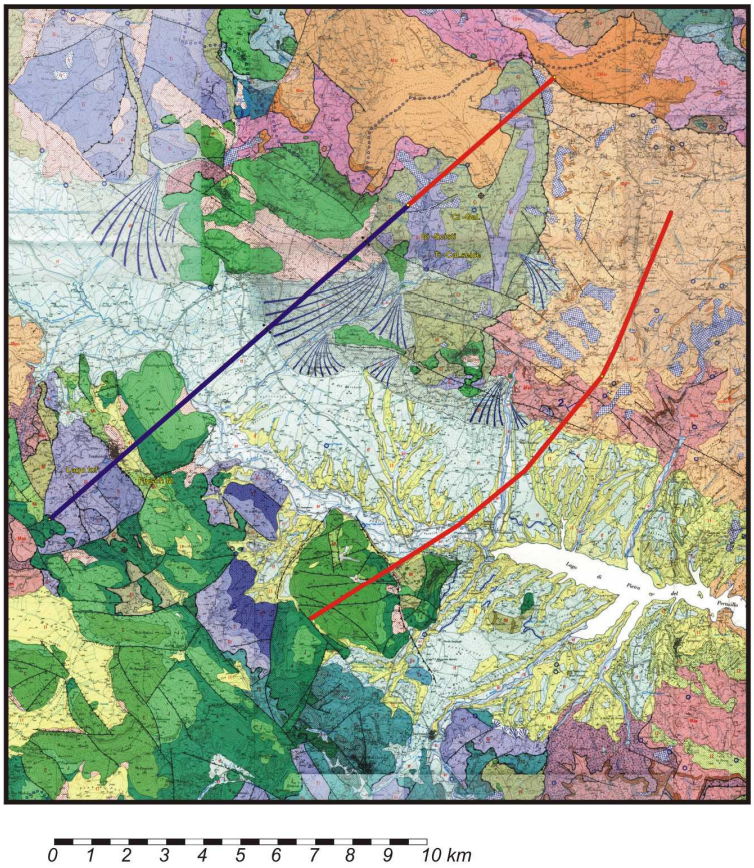

Fig. 3-1. Geological map of the Agri basin (from Lentini et al., 1988) with the location of the two seismic profiles (Esit700 in blue and Esit658 in orange). Note the bending profile of the Esit658 line.

To overcome these limitations, and with the aim to enhance seismic data quality beneath the basin, the Enterprise Oil Italiana and Eni acquired, in 1999, two seismic lines with a non-conventional multi-fold wide-aperture acquisition lay-out (Dell'Aversana, 2003) characterized by densely spaced shots and receivers to a maximum offset of 18 km.

These wide-aperture profiles allowed recording of dense refracted and turning waves, as well as large amplitude post-critical reflected waves at large offset, that are well suited to estimate the large-scale velocity distribution at depth by first-arrival or combined first-arrival/reflection traveltimes tomography (e.g. Dell'Aversana *et al.*, 2002). Besides providing complementary information on the investigated structure, the velocity models obtained by traveltimes tomography could be used to improve near-vertical reflection data processing (tomostatic) and to apply pre-stack depth migration (Dell'Aversana *et al.*, 2002; Dell'Aversana, 2003).

This dense wide-aperture dataset provides a unique opportunity to obtain a very detailed image of the shallow structure of the Val d'Agri basin since dense and clear first-arrival

traveltimes associated to direct, turning and head-waves observed up to 6-8 km offsets, are well suited to perform a high-resolution tomography. In addiction, data redundancy makes the tomographic inversion more stable.

In order to obtain two high-resolution 2D *P*-velocity models for both lines, first arrivals traveltimes were hand-picked on common shot record sections, selected according to the signal-to-noise ratio. Due to the high complexity of the investigated shallow structure, traveltimes were inverted using a non-linear inversion procedure effective to image strongly heterogeneous media.

The present chapter is organized as follow:

- description of the seismic experiment
- data processing and first-arrival traveltime reading
- non-linear tomography inversion method
- models description and resolution

The seismic survey

Seismic data used in this study were collected in 1999 by Entreprice Oil and Eni-Agip (ESIT R & D project – Enhance Seismic in Thrust Belt; EU Thermie fund) with a non-conventional multi-fold wide-aperture acquisition geometry along two SW-NE striking profiles (Esit700 and Esit658), crossing the Val d'Agri basin (fig. 3-1).

The Esit700 profile has a maximum length of 18 km extending from the south-western Monti della Maddalena toward the north-eastern M.te Caldarosa mountain system; it crosses the Agri valley in correspondence of Tramutola and Villa d'Agri villages. The Esit658 line is located to the south of the basin and extends for a maximum length of 15 km. It crosses Grumento Nova village in the Agri valley. Shots are located on different types of rocks belonging to the basinal Lagonegro unit, to the carbonates of the Apennine Platform and to the Quaternary continental deposits of the Agri fluvial system (fig. 3-1). This complex surface geology influences the shots efficacy and affects the seismic energy radiation.

Vertical-component 10 Hz geophones were deployed for the whole lines length with a constant spacing of 90 m. Conventional explosive charges (5-10 kg) were shot every 60 m along the profiles (fig. 3-2), in boreholes at a nominal depth of 20 m. The sampling rate was 100 Hz.

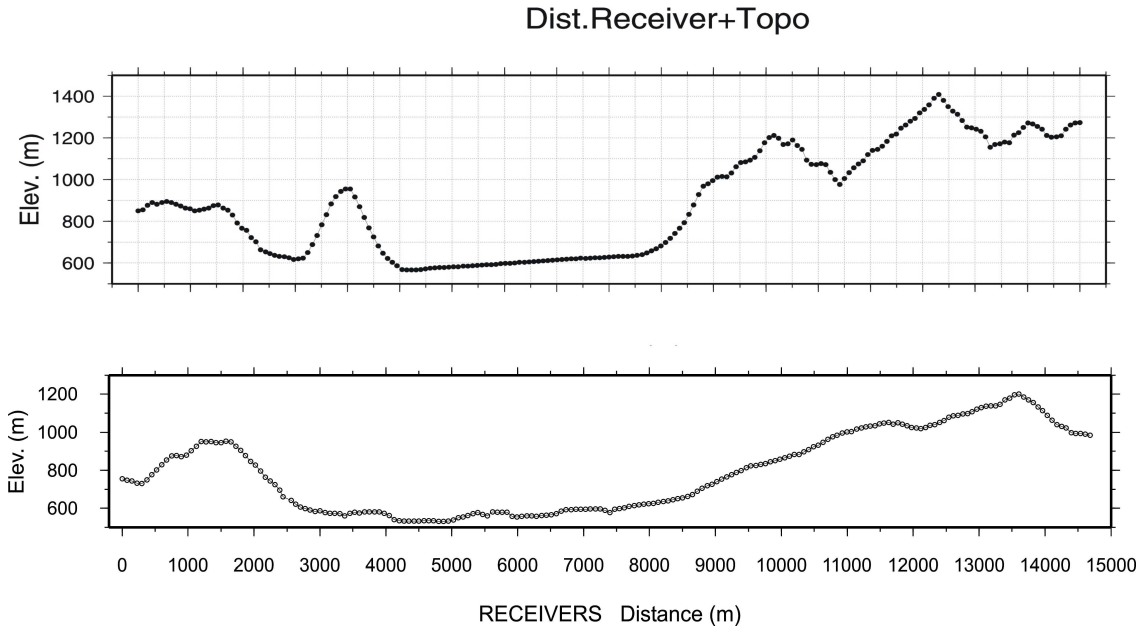

Fig. 3-2. Receiver distribution along the Esit700 (top) and Esit658 (bottom) seismic profiles.

The topography along the profiles is extremely rough, the maximum difference in height is about 600 m (fig. 3-2). Some problems related to the acquisition layout are: the irregular spacing of the sources along little portions of the profiles (i.e. no sources in correspondence of Tramutola village along Esit700 (fig. 3-2) and in the western portion of the Esit658 line close to Grumento Nova), and the bending trace of the Esit658 line (fig. 3-1).

First-arrival times: data processing and picking

First-arrival traveltimes were accurately hand-picked on sections arranged in Common Shot Panel (hereinafter CSP). We selected 111 CSPs for the Esit700 line and 99 CSPs for the Esit658 line, according to signal-to-noise ratio and being careful to keep a good coverage all along the profiles. Every CSP section, for the Esit 700 and Esit 658 line, is made of 144 and 201 seismograms, respectively.

The analysis of the Esit700 profile was limited to a maximum 13 km offset toward NE. The reasons are a general low signal-to-noise ratio that makes difficult the picking beyond few km to the source, and because data from CSPs from such a large offset do not contain information about the basin structure that is the target of this study.

Data quality strongly depends on the position of the source along the profile (i.e. on the local geologic conditions). Record sections for shots in the continental deposits filling the Agri basin share an overall good signal to noise ratio (fig. 3-3a).

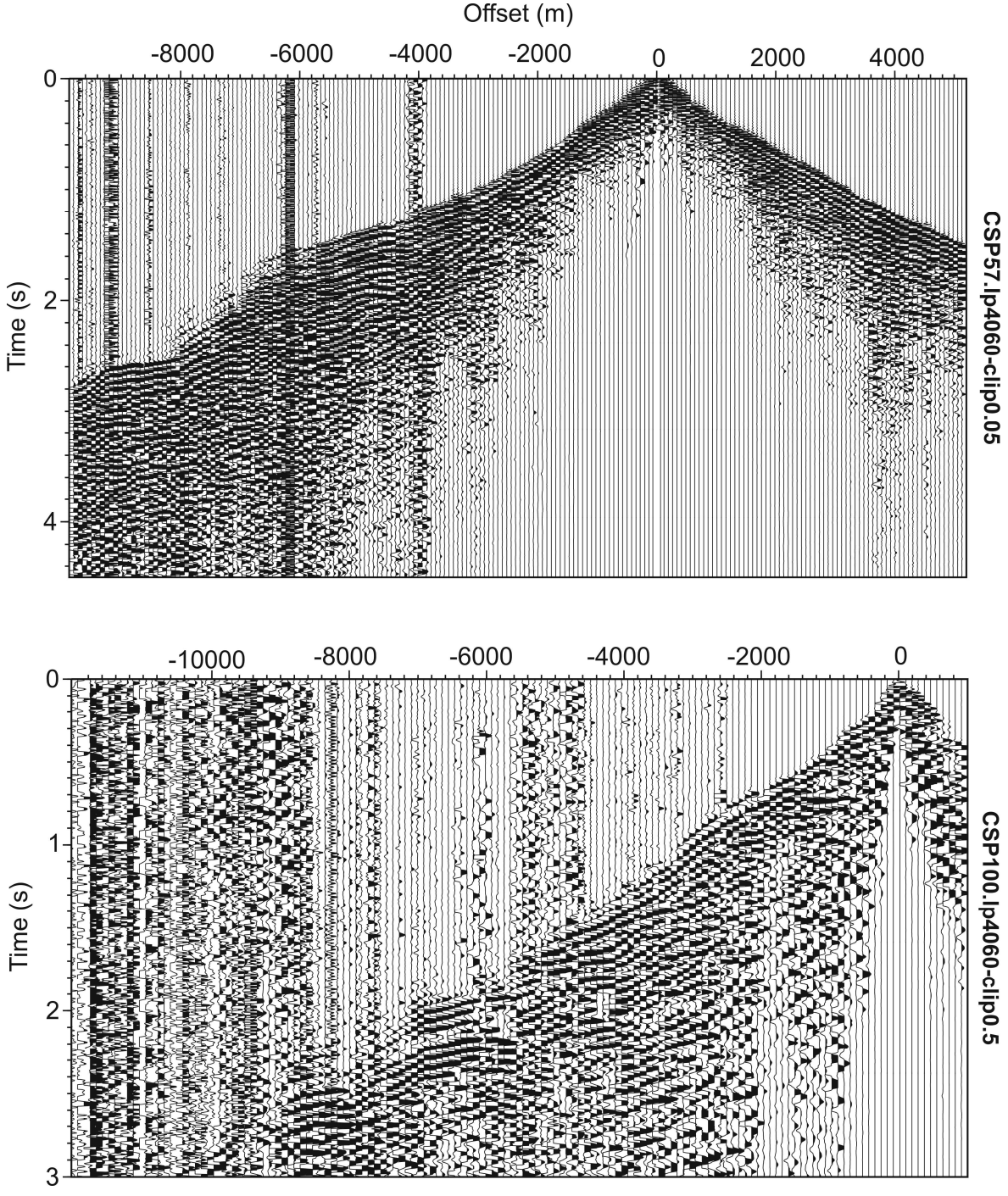

Fig. 3-3. Examples of two multi-fold wide-aperture Common Shot Panels at different offset. Data quality dramatically depends on the complex surface geology. The sections are plotted with a normalized amplitude and a 40 Hz low-pass filter to remove high-frequency noise. (top) First-arrivals are clearly visible up to 6 km offset. The rapid attenuation of first-arrivals amplitude (shadow zone) at 6 km offset

testifies the presence of a complex velocity field. (bottom) CSP section for a shot located on the eastern side of the basin where crop out basinal rocks of the Lagonegro Fm.

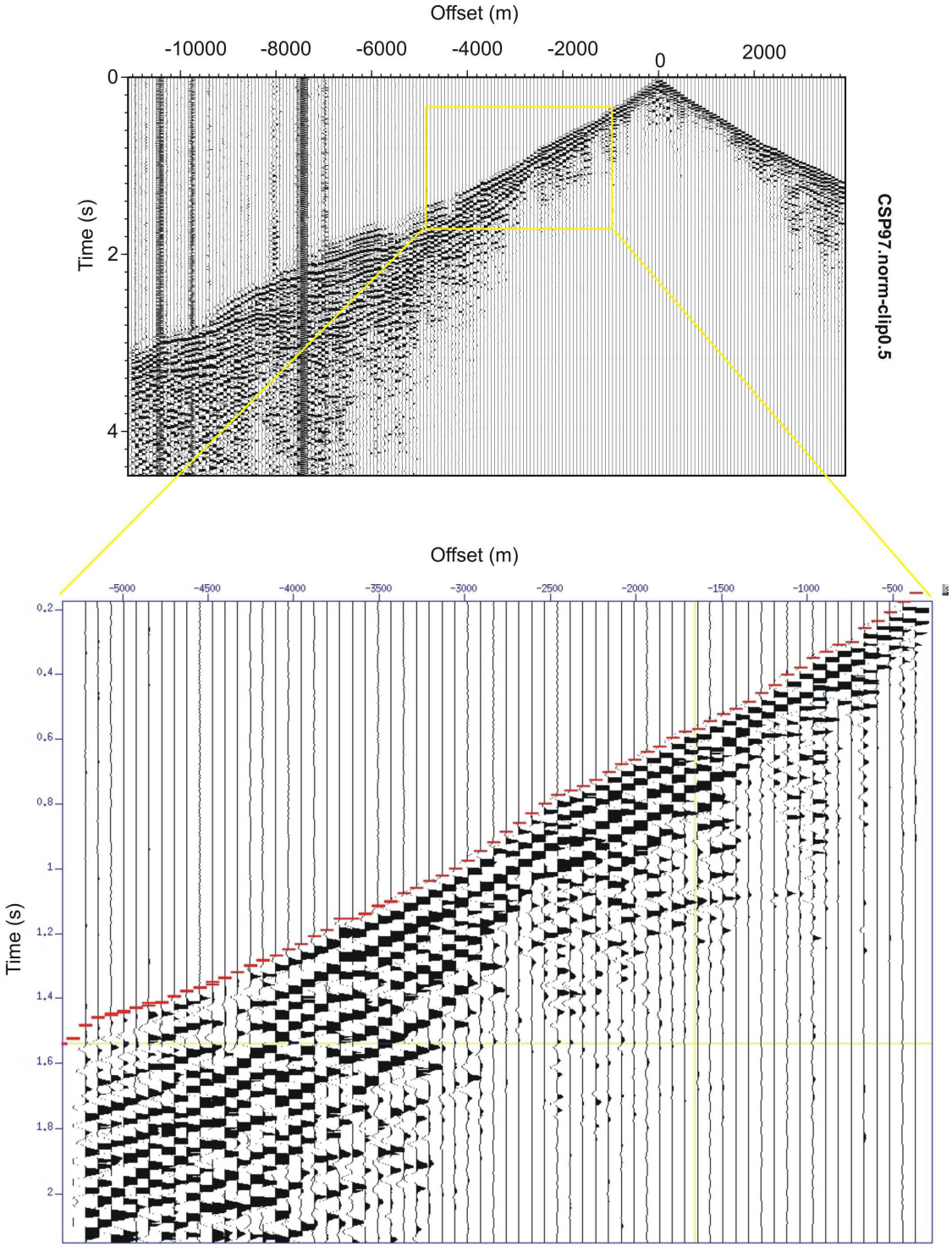

Fig. 3-4. Example of first arrival times picking on good quality data.

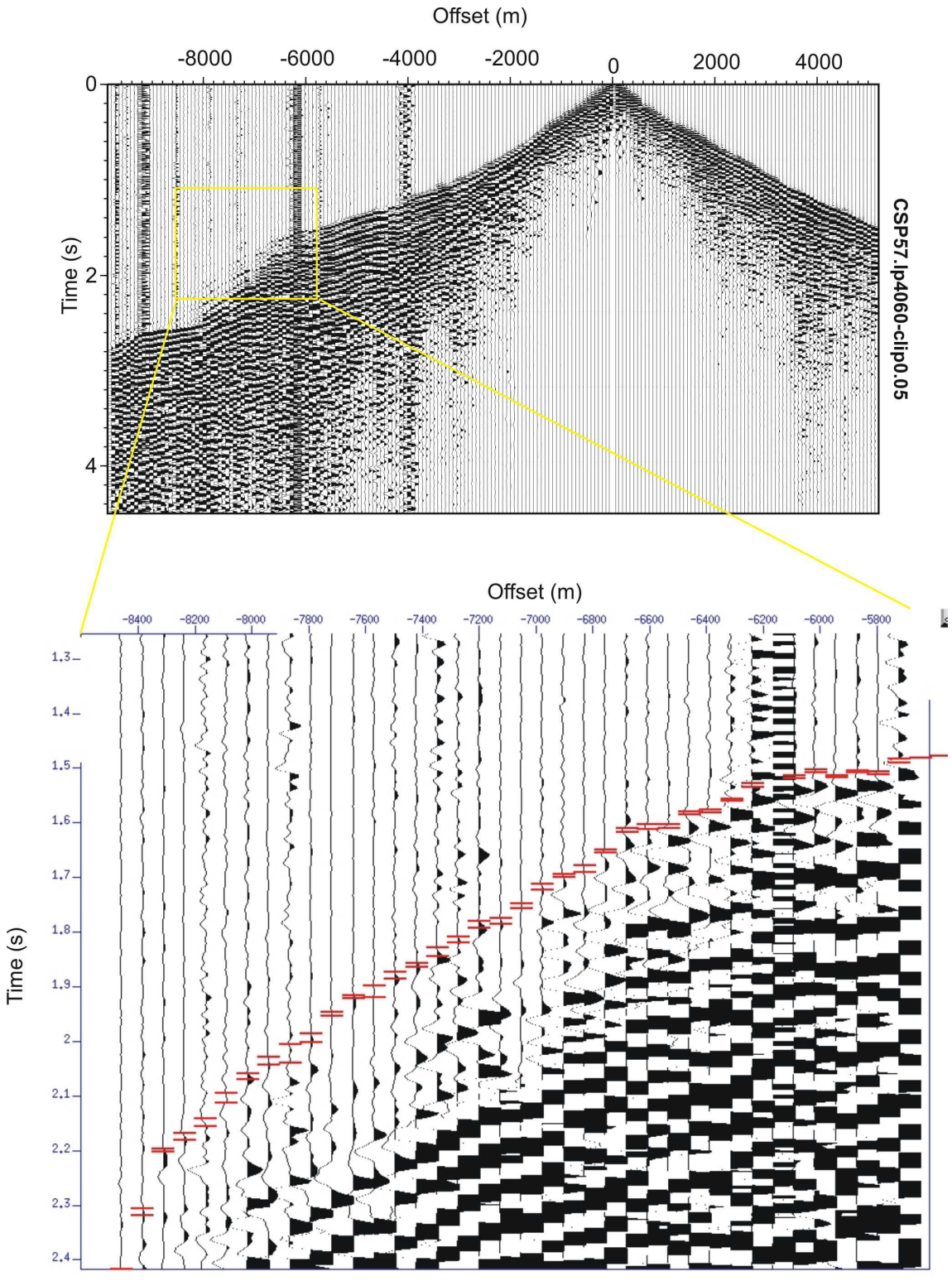

Fig. 3-5. Example of subtle first arrival times picking at large offset.

First-arrival are very clear up to 5-7 km offsets; at larger offsets first-arrivals are affected by a strong, rapid attenuation in correspondence of a shadow zone. This effect testifies the complexity of the velocity field (presence of a low-velocity layer) and makes the identification of first-arrivals at larger offsets difficult.

Conversely, CSPs for shots performed at the edge of the profiles on basinal rocks of the Lagonegro units exhibit a lower signal-to-noise ratio and very subtle first-arrivals beyond 3-5 km offsets (figure 3-3b). In this case, large part of the seismic energy is lost to produce ground-roll.

In order to facilitate first-arrivals identification and to ensure an accurate picking in case of poor-quality traces, signal-to-noise ratio around first-arrivals was improved by filtering data. The filter operator was designed based on results of frequency-time analysis performed on traces selected at different offsets for numerous CSPs by using the Gabor Transform (Dziewonsky *et al*., 1969) (fig. 3-6).

First-arrivals have a frequency content in the 10-40 Hz range, with a progressive shift toward low-frequencies for increasing offsets due to the anaelastic attenuation. Consequently, first-arrivals identifications and picking for both poor-quality CSPs and large-offset traces were performed after the application of a low-pass filter with a 40 Hz corner frequency suitable to suppress high-frequency noise (fig. 3-5). Conversely, clear impulsive first-arrivals observed on good-quality CSPs in the small-intermediate offset range (< 5 km offsets) were picked on raw trace (fig. 3-4).

First-arrivals identification for traces beyond 3-4 km is further facilitated by plotting data with a reduction velocity of 5.5 km/s that allows to align subtle head-waves refracted by a high-velocity layer located beneath the Agri basin (fig. 3-3a).

We did not use a more complicated processing sequence because of the overall data high-quality and because the application of FK filter to remove coherent noise or of Automatic Gain Control to enhance first arrivals would have modified the waveform and consequently worsen the reading accuracy.

More than 23500 first arrivals were hand-picked following a *picking* strategy which is based on the reading of a time window (t_1, t_2) instead of a single reading with a weighting factor (Herrero *et al*., 1999; Improta *et al.*, 2002). At the time t_1 we observe a change in the waveform character, amplitude standout and in the signal coherence suggesting the first pulse arrival, while the time t_2 corresponds to the upper limit for the first pulse based on clear arrivals of seismic waves on the trace (figg. 3-4 and 3-5).

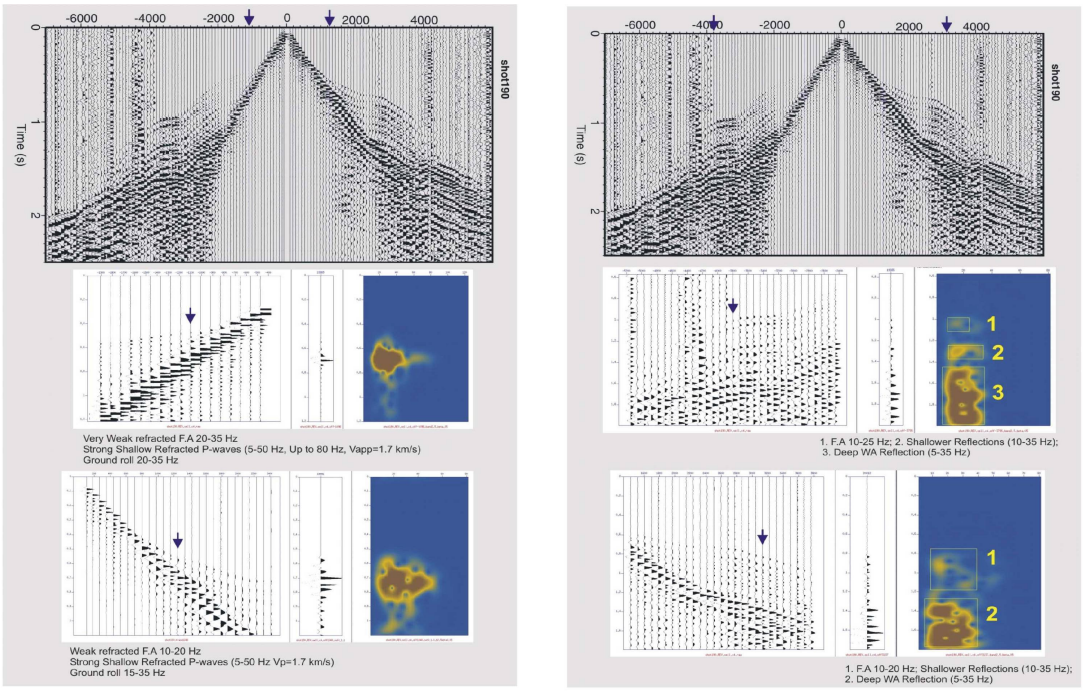

Fig. 3-6. Frequency time analysis by Gabor transform. First-arrivals frequency content at small (1500 m) and intermediate (5000 m) offset.

In this picking strategy the probability function inside the picking window t_2-t_1 is considered constant and is not associated to a Gaussian distribution of the reading error around the arrival time. This strategy is much more appropriated for a non-linear inversion strategy.

The width of the t_2-t_1 window is used by the inversion procedure as a weight of the picking quality. With this strategy we have three types of first arrival reading: traces with a very good quality picking identified by a t_2-t_1 window equal to the sampling rate; traces with an uncertainty weighted on the t_2-t_1 width and traces with a very low signal-to-noise ratio where it is possible to pick only the time t_2. In this case theoretical arrivals have to be smaller then the measured t_2. The advantage of this strategy is that the picking is easier even on noisy trace.

Impulsive first arrivals with t_2-t_1 window equal to the sampling rate are usually picked up to 4000-5000 m offset. At larger offset first arrivals are identified by a t_2-t_1 window of about 0.03 sec from 5-6 km to 7-8 km offset. Finally, a window with only t_2 assigned is for some poor-quality seismograms for receivers with offset greater than 8000 m.

The figure 3-7 shows the distribution of first-arrival times versus source-to-receiver distance: the curve is characterized by strong knees that testify the presence of strong lateral and vertical *Vp* velocity variations. For this reason a non-linear tomographic inversion code described in details in the following paragraphs was used.

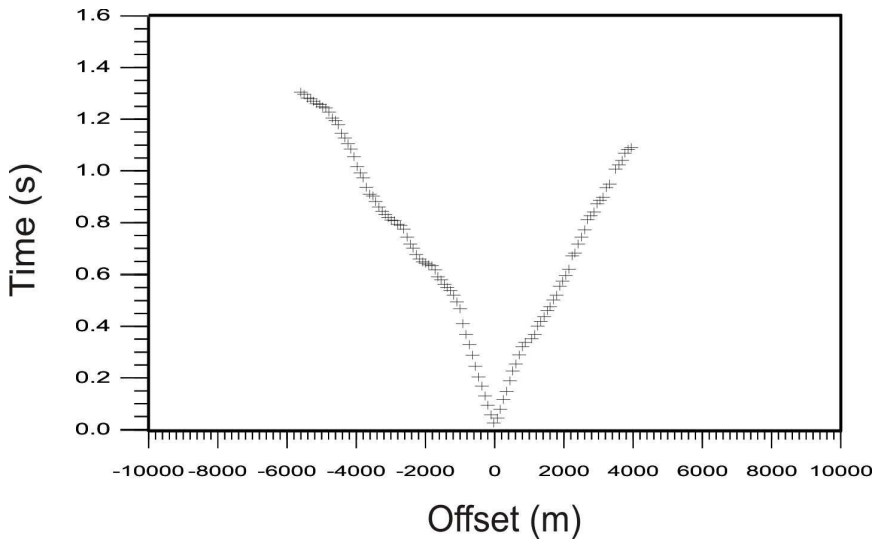

Fig. 3-7. Travel time graph: the distribution of traveltimes with distance is characterized by strong knees that testify the presence of rapid lateral and vertical velocity variations.

The non-linear tomographic technique

Due to the presence of strong vertical and lateral velocity variations in the basin, too strong to be detected by a classical, iterative-perturbative tomography, a non-linear inversion procedure that is specifically designed to image strongly heterogeneous media and does not require a reference starting model was used. Moreover, the estimation of traveltimes by asymptotic, approximate, ray computational methods can be inaccurate due to their difficulties in properly taking into account the ray bounding, shadow zones and head waves generation from irregular refractors. Thus, a pseudo-global, non-linear approach, based on a wave-front tracing technique has been used (Herrero *et al*., 1999; Improta *et al*., 2002).

The main characteristics of the method are described in the following sections.

Forward problem: is solved with a finite-difference Eikonal solver (see Podvin and Lecomte, 1991; Vidale, 1988). This method is based on Huygens' principle, for which every point on a wave-front is considered to be a source that gives rise to another circular wave front. Local discontinuity of the time gradient in the first arrival time field are built as intersections of locally independent wavefronts. This method provides accurate first-arrival traveltimes for extremely severe and arbitrary shaped velocity contrasts and also take into account the existence of direct, refracted and diffracted waves. Tracing the isochrones in the medium we obtain an image of the first-arrival wave-front propagation. A simple type of representing the propagation is the use of a *back ray-tracing* procedure (Podvin and Lecomte, 1991): the

principle is to start from the station and follow the maximum gradient direction of the first arrival time function up to the shot point. The grid used in this study for the forward problem computation is very fine (25x25m spaced). Such a fine grid is necessary to perform a very accurate estimation of first-arrival traveltimes. However, this grid has too many nodes to be used for the model parameterization.

Velocity model parameterization: the medium is parameterized by a grid of points in which the velocity is defined. The velocity in the other points of the model is assigned by a 2D bi-cubic spline interpolating function (see Lutter *et al*., 1990). This inversion grid is coarser than the grid used for the computation of the forward problem. If the computational grid was used as inversion grid the inverse problem could become too non-linear, requiring computational time too large for an exhaustive exploration of the model parameters space.

Inverse Problem: the inversion strategy is based on a "multiscale" approach and a non-linear optimization scheme.

The multi-scale procedure consist of a series of inversion runs and at each run the number of the model parameters is progressively increased refining the node grid. The first run is performed without a-priori information. The following runs use the models from the previous run as reference model (see scheme shown in figures 3-8 for an easier comprehension). This approach, introduced by Lutter *et al*. (1990), allows to determine in the early stage of the inversion procedure the large-wavelength components of the velocity model and then progressively to image the smaller wavelength components.

Each inversion run is solved by searching for the minimum of a least-square L_2-norm defined as the sum of the weighted square differences between observed and computed traveltimes. The inversion method adopt a hybrid scheme based on a combination of global random search (Monte Carlo technique) and a local search performed by Downhill Simplex algorithm (fig. 3-9). This approach allows the dense exploration of the model parameters space and reduces the risk to be trapped in secondary minima of the cost function because when a local minimum of the cost function is found, through the local search algorithm, a global search is performed (fig. 3-9).

Fig. 3-8. Flow scheme followed during the multi-scale inversion procedure for the Esit658 line, to achieve the best-fit model.

At each inversion run a velocity perturbation is assigned at each nodes. This parameter (ΔV) is generally high in the early stages of the inversion procedure, when only the large wavelength components of the model is resolved, but rapidly decrease in the final stages when the inversion procedure recovers the short wavelength components of the model (fig. 3-8).

A lower limit of 50 m/s and an upper limit of 7000 m/s were used as a-priori constrains in order to avoid unrealistic high *P*-wave velocity.

The method includes two stopping criteria: one for each inversion run and one for the whole inversion procedure.

- Each inversion run is stopped when the value of the misfit function does not vary even after a large number of global explorations (e.g. Monte Carlo algorithm) (fig. 3-9). Anyway, even when a lot of iterations are run, we are not sure that the absolute minimum of the misfit function has been reached. In order to further reduce the risk to obtain a model corresponding to a secondary minimum of the cost function, each inversion run is repeated starting from a different starting model (e.g. different global search in the model parameters space with a Monte Carlo initialisation) (fig. 3-8).
- The multi-scale procedure is stopped:

- if the total residual *rms* is comparable to the data variance
- if the value of the misfit function for successive runs has a little reduction (in percentage with respect to the previous one)
- according to the results of an *a-posteriori* resolution test performed on the final minimum-cost-function model, focusing on the resolution of the target of the study.

Resolution

An important drawback of a non linear inversion technique is the resolution assessment of the retrieved image. Meanwhile, in the classical linearized inversion theory, this assessment is well established by computing the resolution matrix, there is no fast technique to evaluate resolution of a model resulting from a non linear inversion. A practical solution is to perform an *a-posteriori* resolution study. Resolution of the minimum cost function model for each inversion run is qualitatively assessed by an "*a-posteriori"* checkerboard resolution test (fig. 3-10).

In practice:

- a perturbation (± 100 m/s), small enough not to change the wave path in the medium between shots and receivers, is added to the final model. The perturbation has a chessboard pattern and is defined by a bi-dimensional sinusoidal function (fig. 3-10)
- first arrival traveltimes are then computed for the "*perturbated model"* and a new dataset is set up
- a new inversion is run using the new computed dataset and the final model as reference
- the obtained velocity model is subtracted to the reference model

Thus, in case of perfect resolution (Resolution matrix = Identity matrix) the difference between this new model and the reference model must give the chessboard perturbation pattern in shape and amplitude. In the reality, the chessboard perturbation pattern is recovered only in the well-resolved regions of the model (fig. 3-10). It is worth noting that increasing the number of the model parameters the resolution depth becomes progressively smaller (see the recovered perturbation patterns in figg. 3-12, 3-13, 3-14). The reason is that moving deeper the model sampling decreases and consequently the smaller wavelength components of the model will be resolved only in the shallower part of the image.

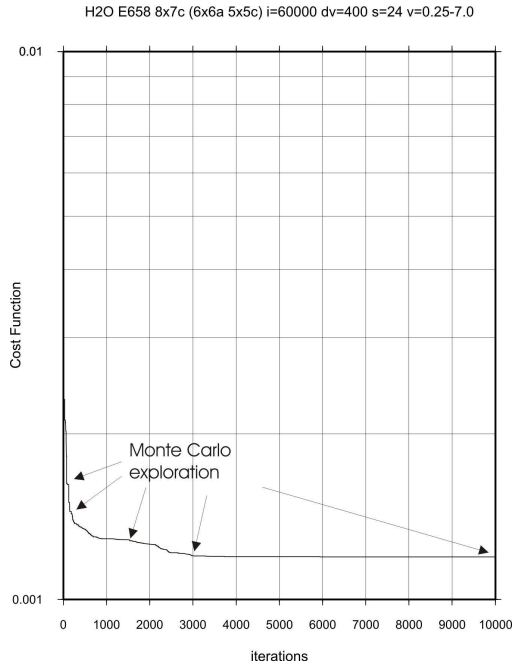

Fig. 3-9. Example of cost-function reduction, showing local (Downhill Simplex) and global (Monte Carlo) search, for the fifth run of the Esit658 inversion procedure. The inversion run is stopped when the misfit function does not change even after numerous global Monte Carlo exploration.

First arrival time inversion

Esit 700 line

The dataset inverted includes 8287 first-arrival traveltimes. In order to avoid border effects, the model was extended 500 m south-westward and about 700 m north-eastward. The model is 14 km in length and 2.9 km in thickness, extending from -1.2 km b.s.l. to 1.7 km a.s.l.. A grid spacing of 25x25 m has been used for traveltimes computation. A lower (50 m/s) and an upper limit (7 km/s) were used to avoid unrealistic *P*-wave velocities. The inversion process starts with 6 parameters (3 horizontal nodes x 2 vertical nodes) and ends after 13 runs with a final inversion of 663 model parameters (39 horizontal and 17 vertical nodes corresponding to a node spacing of 308 x 88 m) (fig. 3-14).

The velocity perturbation for each nodes (ΔV) ranges from 1500 m/s (2^{nd} inversion run) to only 200 m/s (13^{th} inversion run). The figure 3-8 represents an example of the flow scheme followed during the multi-scale inversion procedure to achieve the best-fit model.

Each step of the multi-scale procedure is not limited to a single inversion run giving the minimum cost function. For example moving from the second (6 parameters) to the third step different parameterizations are tested (e.g. 5x3, 4x4, 4x3 nodes) and each inversion is repeated with the same parameterization but starting with a different Monte Carlo initialization number (*seed*).

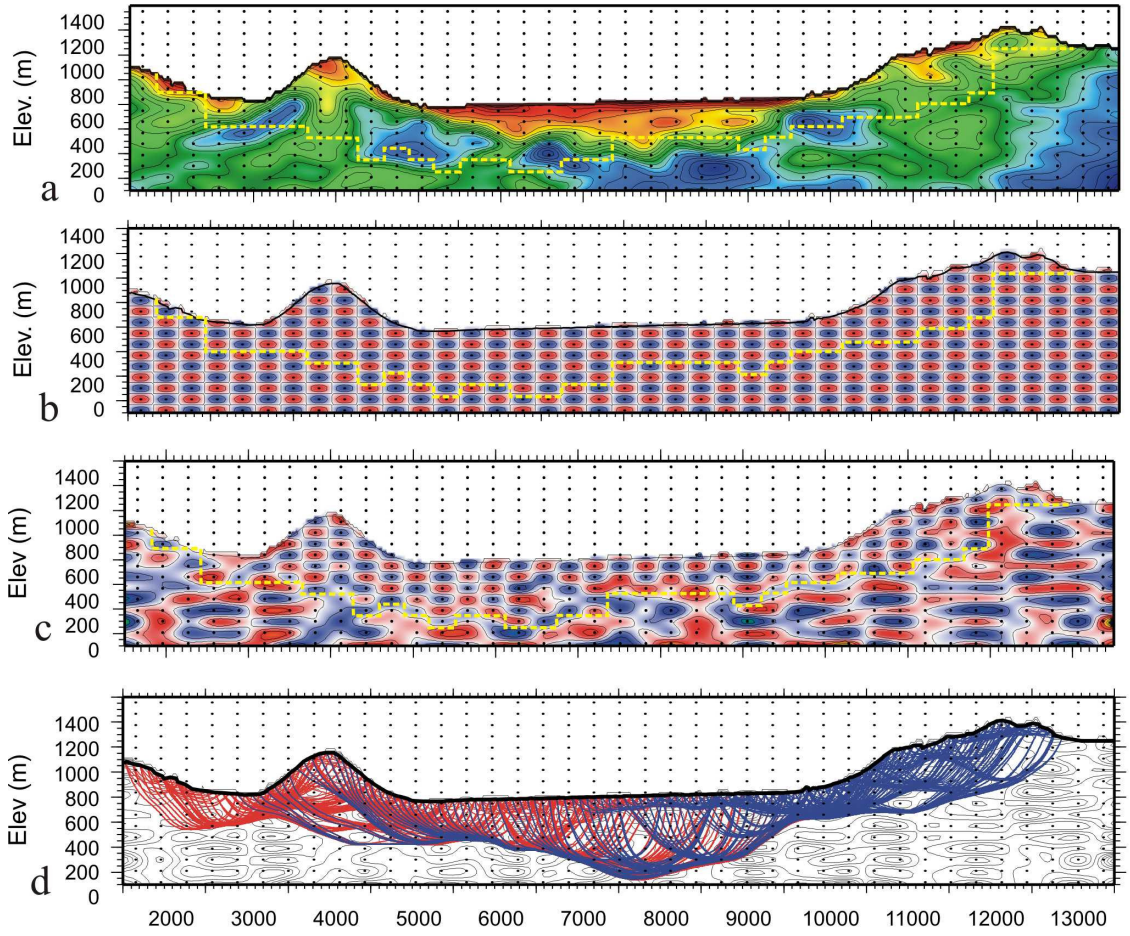

Fig. 3-10. Checkerboard test for the last model of the Esit700 inversion procedure (39x17f). a) the velocity model obtained by first-arrival traveltime tomography; b) perturbation pattern used to perform the checkerboard resolution test. The perturbation consists of a 39x17 cell pattern with a maximum perturbation of ± 100 m/s; c) Retrieved perturbation pattern; d) example of back ray-tracing in the velocity model. The well-resolved region (contoured by a yellow dashed line) is confined to the upper part of the model; the reason is that moving toward greater depth the ray density for each cell decreases and also first-arrival traveltimes are affected by greater reading uncertainty.

Finally, the same inversion is run adopting a different ΔV (e.g. the range for the velocity perturbation that a node can experience) that for this step ranges between 700 m/s and 1500 m/s.

The *"best model"* for each inversion step is selected among several models according to the cost-function value and to results of resolution tests (fig. 3-10).

Proceeding with the inversion runs the model dimension is progressively reduced, according to the well-resolved region, in order to reduce computational time.

Furthermore, seismic phase readings are revised taking into account the computed first-arrival traveltime residuals (fig. 3-11).

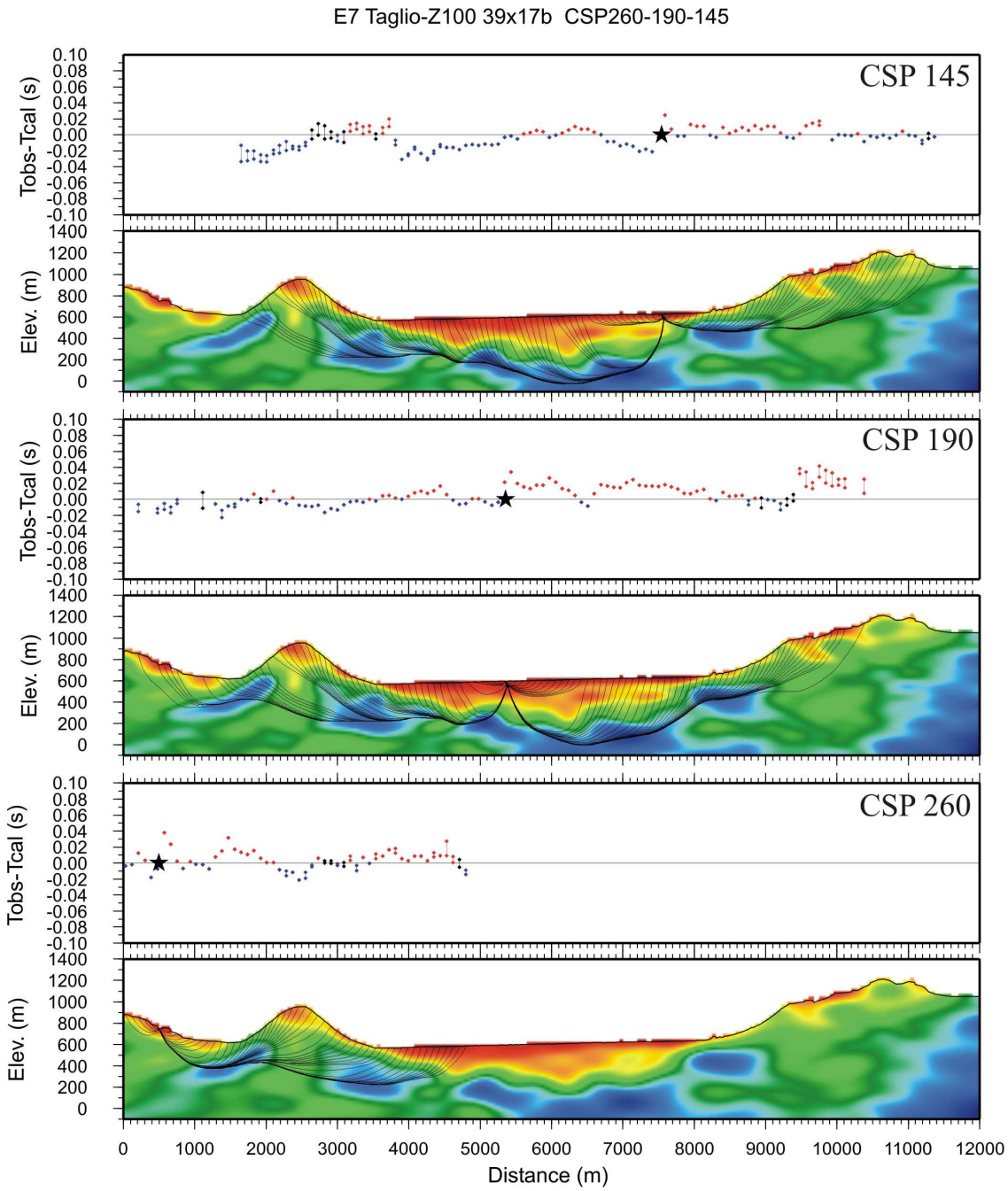

Fig. 3-11. First-arrival time residuals for three representative Common Shot Panel sections. Time residuals are computed for both t1 and t2 times. Shot positions are depicted by a star. In this figure residuals from the last step of the Esit700 procedure model (39x17f) are shown. Residuals are small and confined in the 0.04 s time range. This procedure is a useful way to check picking errors and to verify that traveltime residuals decrease gradually increasing the number of model parameters. Black lines show ray-path computed using back-ray-tracing tecnique.

Moving toward even smaller wavelength models, the computation of traveltimes residuals can highlight inconsistency in first arrivals identification suggesting small revision in the phase reading.

In the following section some "*best models*" representative of important steps of the multi-scale inversion procedure will be described. Each model is showed with the corresponding recovered perturbation pattern and the best resolved region contoured by a yellow dashed line (figg. 3-12, 3-13, 3-14).

As first model (fig. 3-12a) the one resulting from the fourth run is shown. The model 7x5a (2000x580 m node spacing) has 35 parameters and represents a large wavelength model. The resolution depth reaches 1300 m; the model shows an high vertical velocity gradient in the axial and right portion of the model and a pronounced lateral *Vp* variation on the left side of the profile. The model 13x9n (1076x322 m node spacing) (fig. 3-12b) is from the sixth run and has 117 model parameters. Despite its large wavelength component due to the coarse node spacing, this model shows a very clear velocity inversion, in the well-resolved region, on the left side of the profile. The model also shows clear lateral velocity variations at about 7 and 10 km distance. The best resolved region is deep up to 1100 m.

The model 19x10a (190 model parameters; 736x215 m node spacing; run 8) (fig. 3-13a) has been cut along the depth axis, reaching 750 m b.s.l., in order to reduce computational time. The well-resolved region is up to 950 m depth from the surface. The model shows a complex velocity field. The low-velocity body depicting the basin infill is well imaged and also a low *Vp* velocity zone in between two high-velocity zones (at about 4 km distance). Two velocity inversions are observed on both sides of the model; the first located at about 5 km distance and the second at about 10 km distance.

The model 28x15a (420 model parameters; 500x143 m node spacing; run 10) (fig. 3-13b) has a resolution depth of 850 m. Within the low-velocity shallow region (corresponding to the basin infill) are recognizable two bodies with different *P*-wave velocities. The basin bottom has an irregular shape and the substratum shows very rapid vertical and lateral *Vp* velocity variations.

The fig. 3-14 shows the two "*best-models*" of the last inversion steps for the multi-scale inversion procedure. The inversion procedure was then stopped because the resolution power of the data does not allow to obtain more detailed information about the basin structure. Both models show a very detailed picture of the Val d'Agri basin up to 500 m depth.

The model 32x14a (448 model parameters, run 12, 375x107 m node spacing) has a resolution depth of 600 m (fig. 3-14a). The basin infill is highlighted by the low-velocity shallow zone about 400-450 m thick. A low-velocity zone is located at about 5 km distance, between two high-velocity bodies. A very pronounced velocity variation appears at about 9.5 km distance, juxtaposing the body with *Vp* in the range 2500-3000 m/s to a very high velocity body (*Vp* in

the range 4500-5500 m/s). Below the basin, an high-gradient vertical zone separates the basin infill from the basin substratum.

The model 39x17b (663 model parameters, run 13, 308x88 m node spacing) is the last model and the well-resolved region is up to 500 m deep, yielding valuable information about the shallow structure of the Agri basin (fig. 3-14b). The basin is filled by two different units. A body (*Vp* in the range 2500-3000 m/s) outcrops along the right side of the basin; it reaches 400 m depth in correspondence of a basin depocenter (located at about 7.5 km distance) and is characterized by a low-gradient velocity zone with isovelocity lines abruptly deepening toward SW. This body is partially covered by a body with *Vp* velocity in the range 1250-2500 m/s characterized by a progressively westward increase of thickness; it reaches about 250 m depth at about 6 km distance outlining another basin depocenter shifted toward the western side of the basin; isovelocity lines are characterized by a more regular pattern. Below these sediments a region of high *Vp* gradient causes a rapid velocity increase and can be interpreted as the contact between the basin infill and the pre-Quaternary limestone substratum. This region has a very complex shape characterized by an irregular stepwise topography. The substratum is made of two bodies characterized by different *Vp* velocity: one has velocities in the range between 3000 and 4500 m/s while the other one is characterized by very high *P*-wave velocities (4500 and 6000 m/s). These bodies are arranged in very complex shapes depicting very strong lateral and vertical velocity variations. An high-angle contact is highlighted by the pattern of the iso-velocity lines on the eastern side of the profile. Finally, an anomalous low *P*-wave velocity (2250-4000 m/s) body in between two high-velocity bodies is imaged in correspondence of the Monticello Hill, located at about 4000 m distance where carbonates of the Apennine Carbonate Platform outcrop. To better investigate this velocity anomaly detailed field mapping was conducted. This topic will be addressed in detail in the following sections and in the chapter 4.

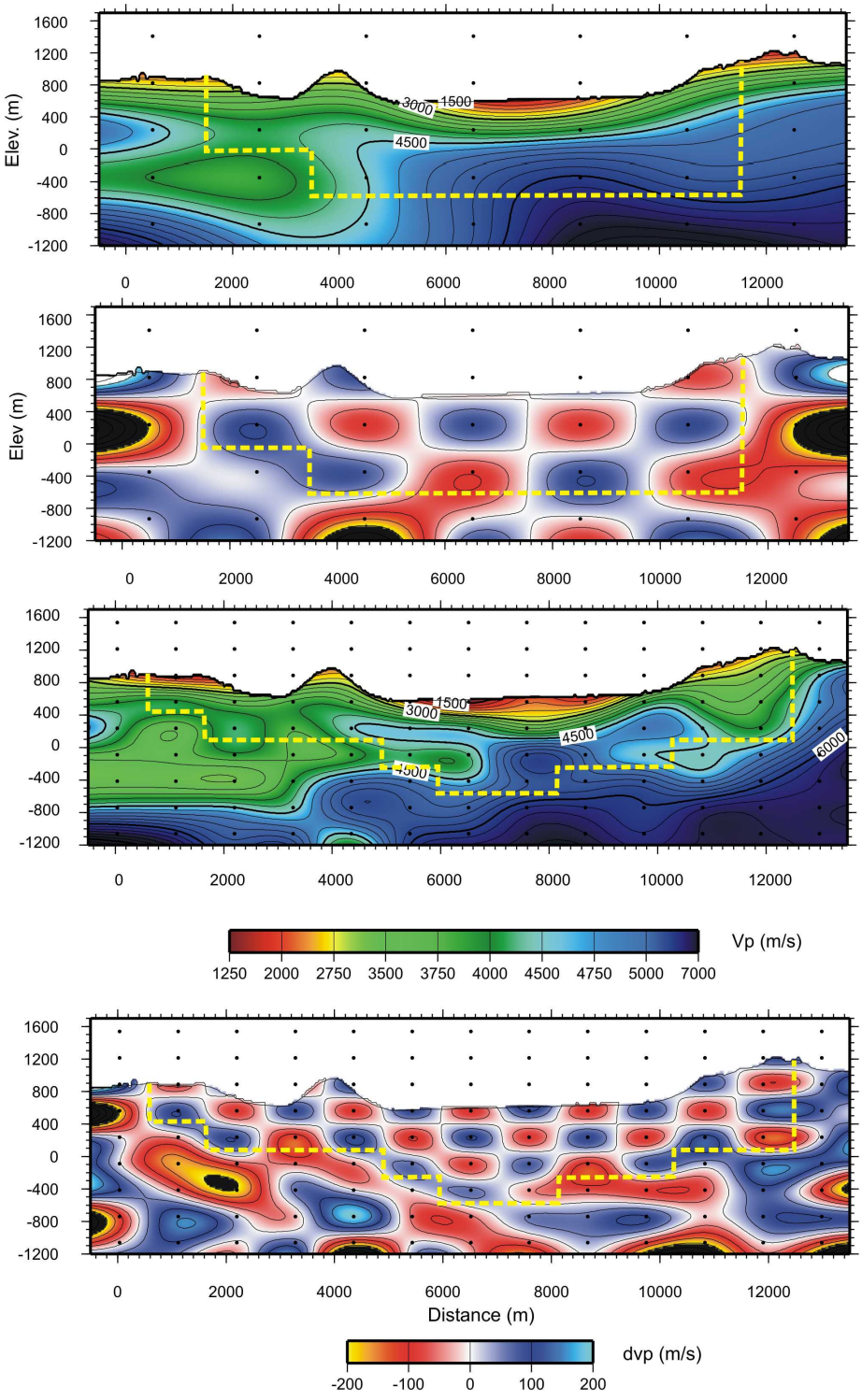

Fig. 3-12. Esit 700 inversion procedure: two large wavelength models with their retrieved perturbation pattern. The best resolved region is contoured by the yellow dashed line. The black circles indicate the control points. The model 7x5xx (top) is from the fourth run. The model 13x9n (bottom) is from the sixth run. The maximum resolved depth is 1300 m. A velocity inversion is already retrieved in the model on the right. See text for further explications.

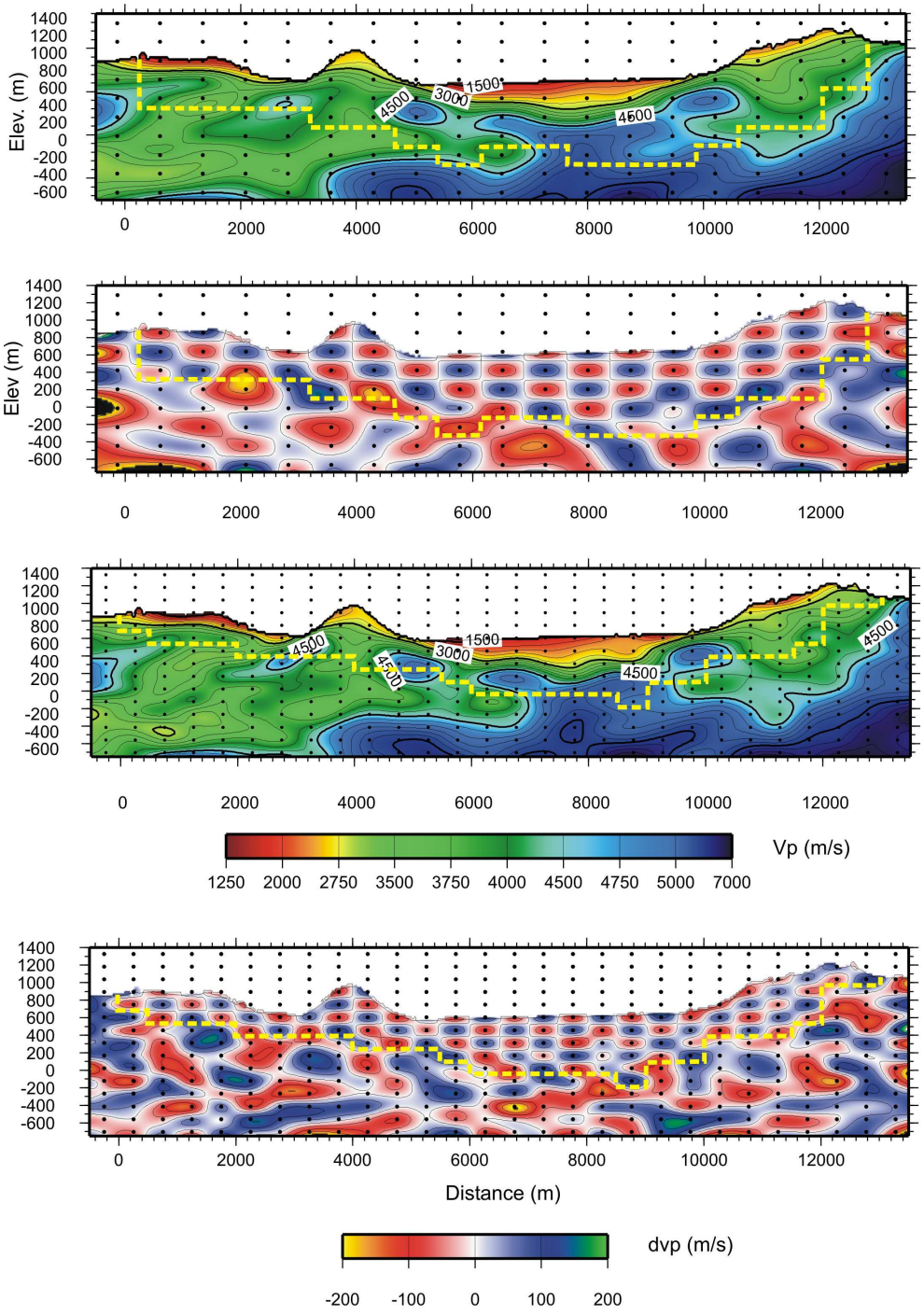

Fig. 3-13. Esit 700 inversion procedure: two intermediate wavelength models with their retrieved perturbation pattern. The best resolved region is contoured by the yellow dashed line. The model 9x10a2 (top) is from run eight. The model 28x15a (bottom) is from run ten. The maximum resolved depth is 950 for the model on the left and 850 m for the model on the right.

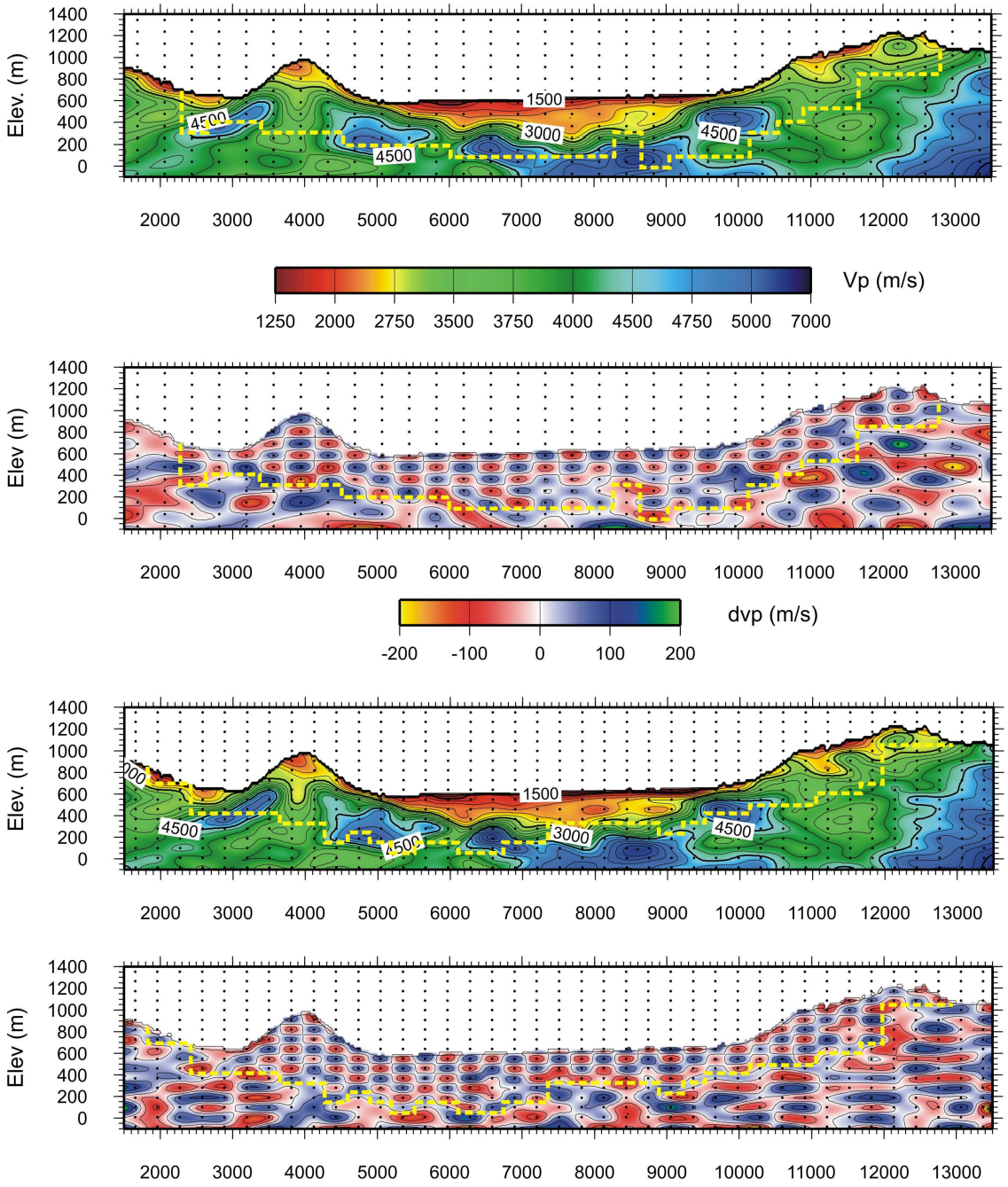

Fig. 3-14. Esit 700 inversion procedure: very high-resolution models. The model 32x14a (top) is from run 12. The model 39x17b (bottom) is from run 13 (last one) and has 663 inversion parameters. The well-resolved region is up to 500 m depth (about 0 m a.s.l.).

Esit658 line

For this seismic profile 15218 first-arrival traveltimes were inverted. The model is 15.5 km in length and 2.9 km in thickness (from -1.2 km b.s.l. to 1.7 km a.s.l.) and was extended 500 m south-westward to avoid border effects. The grid used for the forward problem is a 25x25 m mesh.

The inversion procedure starts with a 5 parameters model (3 horizontal x 2 vertical nodes) and stops, after 14 inversion steps, with a 350 parameters (25 horizontal x 14 vertical nodes) final model (fig. 3-16). The figure 3-8 shows the multi-scale scheme followed during this inversion procedure to achieve the final model. The range for the velocity perturbation (ΔV) applied for this inversion procedure ranges between 1000 m/s and 200 m/s. As for the Esit700 line, in the following paragraph the most representative tomographic images will be shown.

Fig. 3-15a shows the model 8x7n, obtained after 7 runs, representing a large-wavelength model (1937 x 414 m node spacing). The best resolved region reaches a depth of 1400 m from the surface. A shallow low-velocity zone is imaged in the central part of the profile depicting the basin infill. A high *Vp* velocity gradient is showed along the western flank of the basin. The substratum shows two very clear velocity inversions: one is located at a shallow depth at about 3 km distance along the western side of the model while another one is imaged at greater depth (-800 m b.s.l.) along the eastern sides of the model at about 10 km distance. A gradual ad positive *Vp* velocity gradient is observed below the basin.

The model 16x12a (fig. 3-15b) is from the run 10 and has 192 model parameters (968 x 241 m node spacing). The well-resolved region is up to 1300 m. Even if this model images the large-wavelength components the resulting tomographic image is complex. A shallow *Vp* velocity region, with velocity up to 3000 m/s corresponds to the basin infill; two velocity inversions are imaged at about 3.5 and 10 km distance.

Fig. 3-16 shows the "*best models*" of the last inversion steps of the Esit658 inversion procedure. Both models show almost the same characteristics suggesting that a further step in the multi-scale inversion procedure will be not useful to obtain a more detailed model (i.e. data variance would be greater than the final total *rms*). The model 21x12a (fig. 3-16a, 738 x 166 m node spacing) and the model 25x14f (fig. 3-16b, 620 x 142 m node spacing) are well-resolved up to 1 km depth.

The model 25x14f shows a shallow body with *Vp* velocity in the range of 1500-2750 m/s corresponding to the basin infill; this body reaches a maximum depth of about 250 m. The contact with the substratum has a quite regular shape. The substratum is constituted by different velocity bodies. At about 3700 m distance the model.

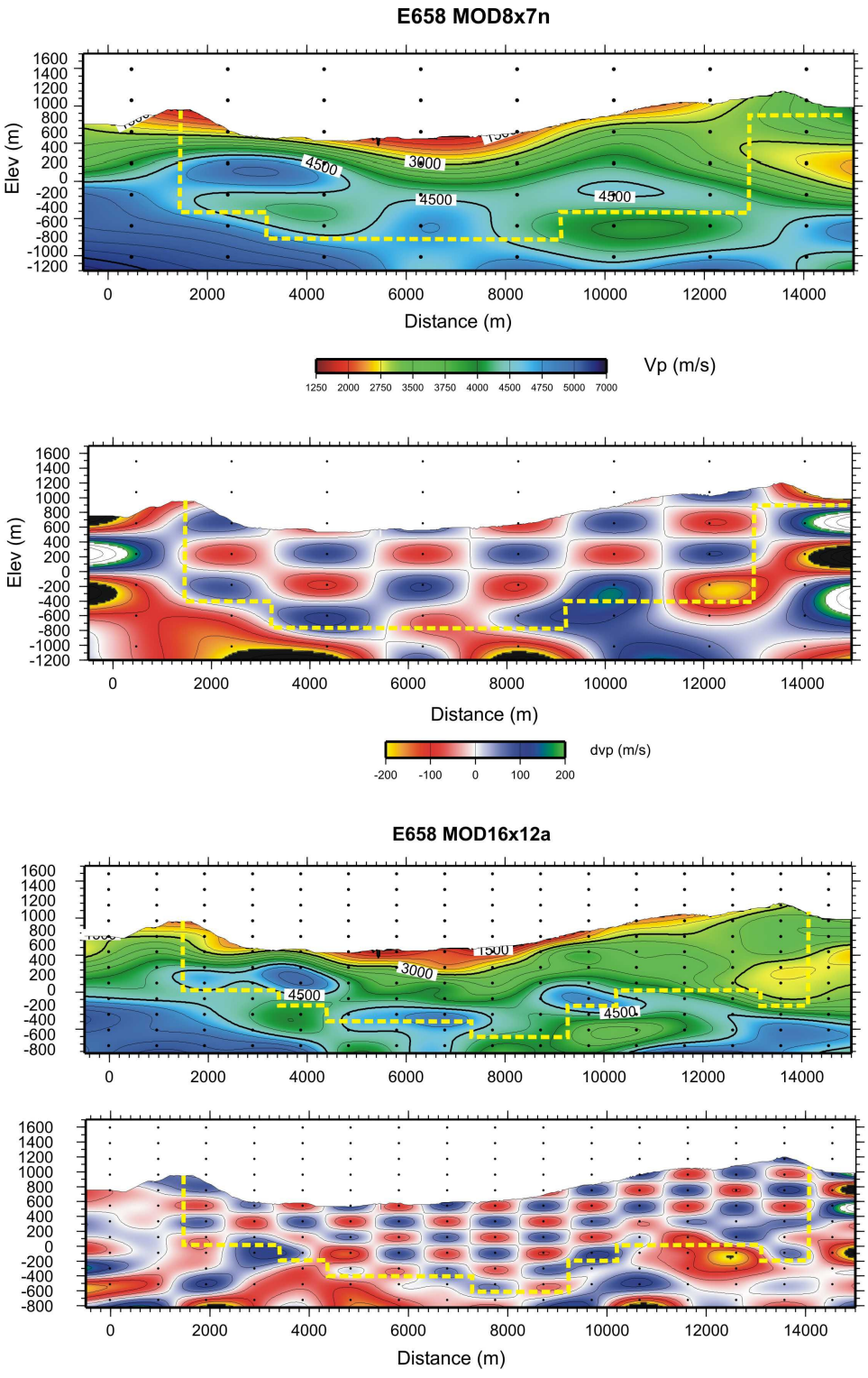

Fig. 3-15. Esit 658 inversion procedure: two large wavelength models with their retrieved perturbation pattern. The best resolved region is contoured by the yellow dashed line. The black circles indicate the control points. The model 8x7n (top) is from the run 7. The model (bottom) is from run 10. The maximum resolved depth is 1200 m.

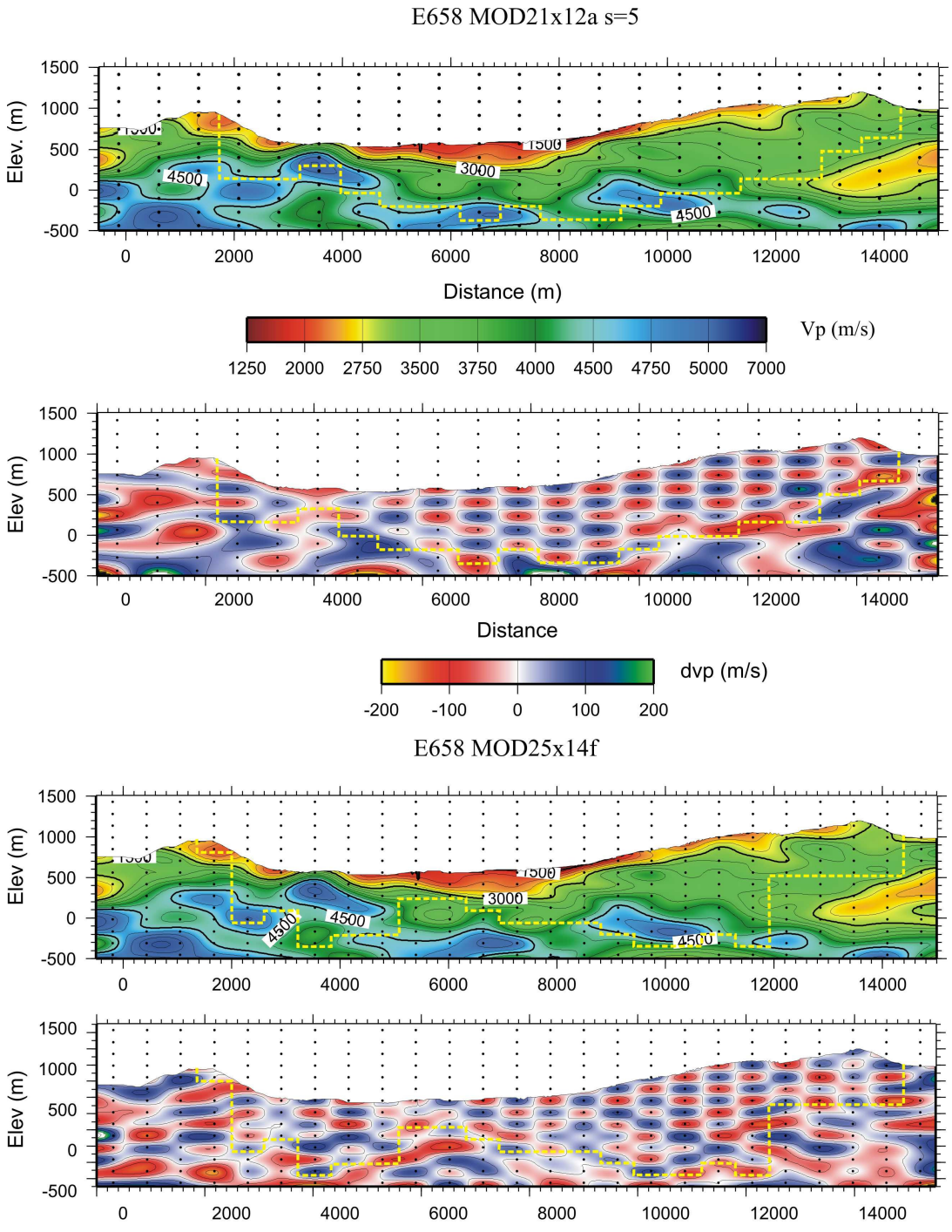

Fig. 3-16. Esit 658 inversion procedure: very high-resolution models. The model 21x12a (top) is from run 12. The model 25x14f (bottom) is from run 13 (last one) and has 350 inversion parameters. The contour of the well-resolved region is quite irregular; the maximum depth is up to 800 m (corresponding to -200 m b.s.l.).

Along the left side of the basin (about 4 km distance) the model images an abrupt velocity increase that puts a high-velocity body (*Vp* between 4500 and 5250 m/s) at shallow depth. Moving toward the central and the right portion of the model a body with *Vp* velocity in the range of 3000 and 4500 m/s and variable thickness can be followed through the entire tomographic image. This body is characterized by a low-velocity gradient. Below this body a continuous region with velocity in the range 4500-5000 m/s can be recognized.

2D velocity models interpretation

We used the available surface geologic information (Lentini *et al*., 1988), four exploration wells published by Dell'Aversana (2003) and results of previous seismic and geo-electrical surveys (Morandi and Ceragioli, 2002; Colella *et al*., 2004; Barchi *et al*., 2006) to provide a first-hand geological and structural interpretation of the tomographic models (figg. 3-17 and 3-18). For the Esit700 line, this first hand interpretation will be refined with results of original mapping discussed in chapter 4.

Esit 700 line

Starting from the basin infill the body with *Vp* velocity between 2500-3000 m/s, located along the north-eastern border of the basin, is associated with slope breccia and fanglomerate deposits (e.g. "Galaino and Marsico Breccias" Early-Middle Pleistocene; Di Niro & Giano, 1995) (fig. 3-17). These deposits reach a thickness of about 400 m in correspondence of the maximum depth of the basin located around 8 km of distance. This feature is interpreted as a structural low hosting a major basin depocenter. The body is thicker along the eastern margin of the basin and may be interpreted as reflecting fan subsidence and thickening at a fault-controlled mountain front, documenting SW-dipping faults (Cello *et al*., 2003).

The cemented breccias are covered by sediments with seismic velocity in the range 1250-2500 m/s, which thickens progressively westward. These sediments are interpreted as the recent alluvial and fluvio-lacustrine deposits of the Agri river (Agri Complex, Middle-Late Pleistocene; Di Niro *et al.*, 1992). These sediments reach the maximum thickness of 350 m in correspondence of a further basin depocenter located along the western side of the basin around 6.3 km distance (fig. 3-17). This thickening could reflect recent fault control by a NE-dipping fault system along the western margin of the valley.

The contact between the Quaternary sediments and the pre-Quaternary substratum has an irregular stepwise topography. This suggests tectonic activity during basin sedimentation, mainly related to a marked component of extensional displacement (fig. 3-17).

The pre-quaternary units correspond to two different *Vp* velocity bodies: the body characterized by a very high *Vp* value (4500-6000 m/s) is interpret as carbonates of the Apennine platform (D'Argenio *et al*., 1975) and the body with *Vp* between 2750 and 4500 m/s corresponds to Mesozoic and Cenozoic cherty limestone, radiolarite and argillite of the Lagonegro basin (Scandone, 1967). Furthermore, *P*-wave velocities allows to discern different units inside the Lagonegro basin rocks: *P*-wave velocities down to 3000 m/s (shown at shallow depth along the eastern side of the profile at distance greater then 10 km) are indicative of Galestri Formation made of argillites and chalky limestone (Scandone, 1967) while higher velocities (up to 4500 m/s) correspond to radiolarites and argillites of Scisti Silicei Formation. This situation is also typified along the western side of the basin where Lagonegro basin rocks repeatedly sits structurally above carbonates of the Apennine Platform. This interpretation is well-constrained by exploration wells (Dell'Aversana, 2003). The fig. 3-17c shows a schematic geologic interpretation of the tomographic image.

The strong lateral velocity variations located both on the eastern and western side of the basin suggest the presence of strong discontinuities related to a series of NW-striking extensional faults, parallel to the basin margin that cut both the bedrock and the overall basin infill on both sides of the basin.

More in details, four steeply dipping normal fault structures, affecting the bedrock and also Lower and Middle Pleistocene continental deposits, causing about 440 m of vertical throw in the carbonate rocks of the Apennine Platform are well-recognizable along the north-eastern side of the basin (e.g. the fault system located around 9500 m distance in fig. 3-17). The slope breccias thickness is well-constrained by an exploration well located in the area. These faults cut the slope breccias and control the location of an ancient depocenter on the eastern side of the basin. These structures are well-known in literature (Lentini *et al*., 1988) and correspond to the SW-dipping strike-slip (Cello *et al*., 2000-2003) reactivated as dip-slip Val d'Agri Fault System (Maschio *et al*., 2005). As these structures offset Lower and Middle Pleistocene continental deposits, their activity must have Middle Pleistocene or younger ages. Moreover, ^{14}C dating of faulted paleosoils indicate that most fault segments in the area were still active in the last 40-20 ka (Giano *et al*., 2000). Thus, this fault system has to be considered active (Machette *et al*., 2000).

It is worth noting that the faults inferred by high-resolution tomography well match the faults traced in the available geological map (fig. 3-17). This result highlights how high-resolution controlled source tomography is effective to investigate shallow fault zones (Hole *et al*., 2006) and complex geological structures (Improta *et al*., 2002). This allows to confirm the

existence of faults previously mapped as presumed because of the absence of recent quaternary deposits clearly involved in faulting.

Along the western side, the tomographic images confirm previously mapped tectonic structures (Lentini *et al*., 1988) such as the thrust fault related to the out-of-sequence thrust of Lagonegro basin rocks onto carbonates of the Apennine Platform and the normal faults affecting carbonates of the Apennine Platform.

Furthermore, sharp lateral velocity changes suggest the presence of NE-dipping normal faults in the central and western sectors of the basin. Three main structures are located at about 5, 6 and 7 km distance, producing a vertical total throws (<200 m) in the carbonates of the Apennine platform but also affecting the continental deposits of the basin highlighting another, and probably younger, depocenter shifted toward the western flank of the basin. These normal-faulting structures were unknown so far.

Following earlier inferences drown by Morandi and Ceragioli (2002) on the base of resistivity and seismic tomographies, and of Maschio *et al*. (2005) based on geological and geomorphological observations, it is here proposed that this depocenter located along the western side (about 6.3 km distance) is the younger depocenter of the basin with Middle-Pleistocene to present-day activity while, the depocenter located around 8 km distance, below the breccias deposits, could be an ancient one, with activity during the first stages of the basin evolution (Early-Middle Pleistocene). This hypothesis is in agreement with the present position of the Agri river, that flows in an asymmetric position along the south-western limit, bounding the Monticello Hill.

The tomographic images interpretation in correspondence of the Monticello Hill and, further west, of the Tramutola thrust is quite ambiguous and made more complicated by the complex geological and structural setting of the area. Therefore, a more precise field survey was needed. This topic will be addressed in the following chapter.

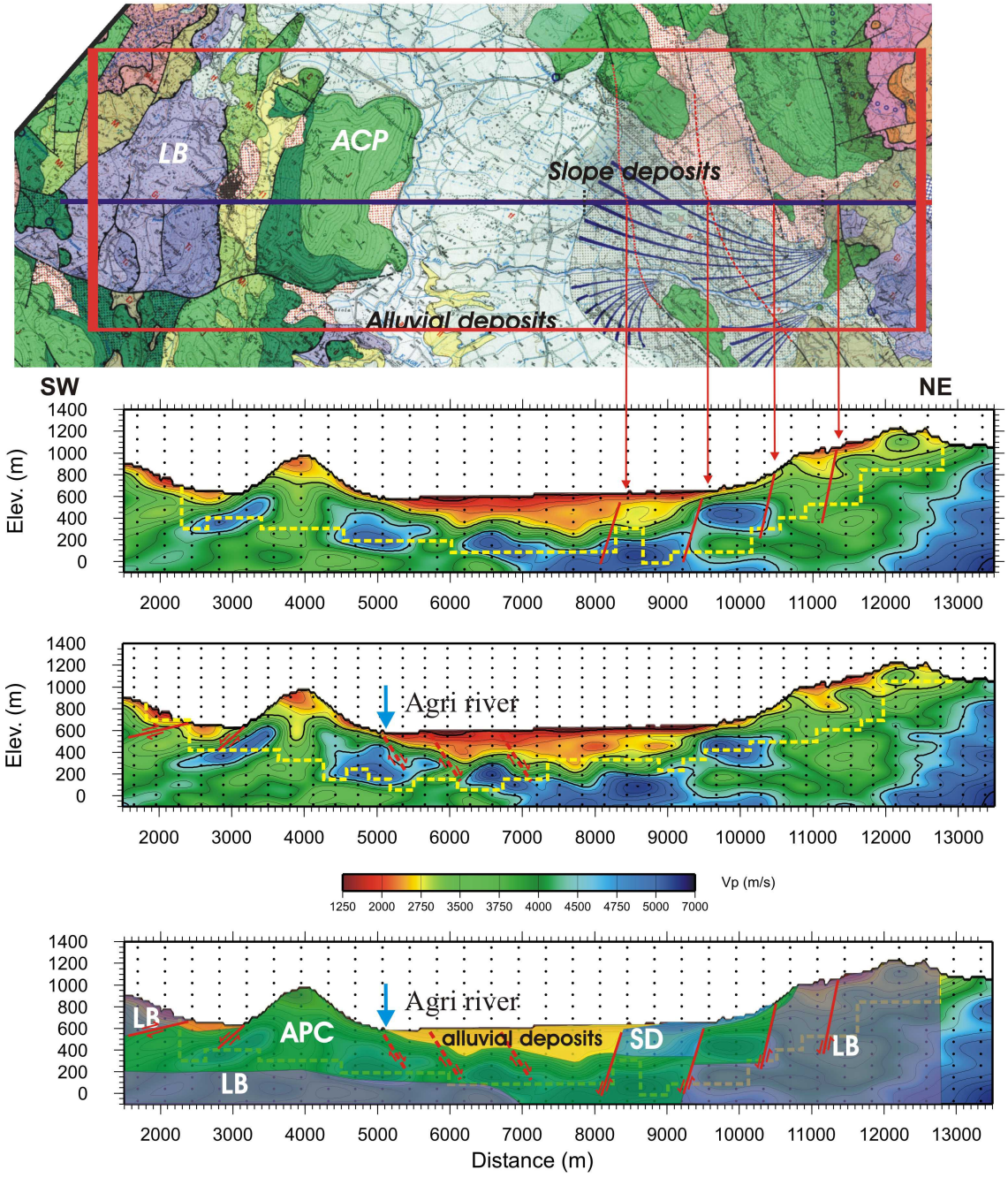

Fig. 3-17. Schematic geological and structural interpretation of the Esit 700 seismic line. a) The geologic map is from Lentini et al., 1988. LB: Lagonegro Basin Formation; ACP: Apenninic Carbonate Platform. SD: Slope Breccias (Lower-Middle Pleistocene); b) The velocity model obtained by the last run of the tomographic inversion (39x17b); c) a schematic geologic interpretation of the tomographic image. The light blue arrow indicates the present asymmetric position of the Agri river shifted toward the south-western flank of the valley. It's worth noting the perfect correspondance between previosly mapped structures and those retrieved by high resolution seismic tomography. The red square delineates the area investigated through detailed field work.

Esit 658 line

Figure 3-18 shows a geological and structural interpretation of this seismic line. The basin infill has *Vp* velocity in the range of 1500-2750 m/s interpreted as lacustrine and alluvial deposits of the Agri river (Middle-Late Pleistocene) that reach the thickness of 250 m at about 8 km distance (fig. 3-18). This indicates that the basin is shallower in this southern sector of the valley respect to the northern sector where the thickness reaches about 400 m in correspondence of the eastern depocenter. This feature is well-constrained by borehole data and geo-electrical tomography (Pierdominici *et al*., 2002; Colella *et al*., 2004). In the southern sector of the basin the present-day position of the Agri river is still shifted toward the western side.

The contact between Quaternary sediments and the substratum has a quite regular topography. Isovelocity lines gently deeps toward NE in the western portion of the basin while a steeper rising is recognizable along the eastern side.

The substratum is made of different units. The body with high *Vp* velocity located at 4 km distance has been interpreted as carbonates of the Apennine Platform outcropping along the south-western margin of the basin. The region characterized by *P*-wave velocity between 3000-4500 m/s, outcropping with variable thickness through the entire profile, has been associated to Sicilide units (Ogniben, 1969) including Lower to Middle Miocene sandstone and marls (Albidona Flysch) and Middle-Late Miocene sandstone and conglomerate Gorgoglione Formation thrust-sheet top deposits. These deposits represent the highest tectonic units of the southern Apennines chain constituting the allochthonous nappes of the mountain belt. An exhaustive treatment of these deposits can be found in the paper by Catalano *et al*. (2004). These deposits unconformably cover the body with velocity between 4500-5000 m/s. The latter is associated to the Lagonegro basin units. Finally, the shallow body outcropping at about 3200 m distance with Vp velocity between 2000-2750 m/s can be associated to siliciclastics deposits developed during the foredeep phase of the Western Carbonate Platform (Bifurto Formation, Lower Miocene).

A schematic structural interpretation of the tomographic image is shown in fig. 3-18. Along the south-western margin two major thrust-fault structures can be identified carrying the Apennine carbonate Platform above the Lagonegro basin deposits and the overlaying Miocene flysch deposits belonging to the Sicilide nappe. The thrust fault located at about 3 km distance affects the Apennine Platform moving the carbonates atop the siliciclastic Bifurto formation deposits.

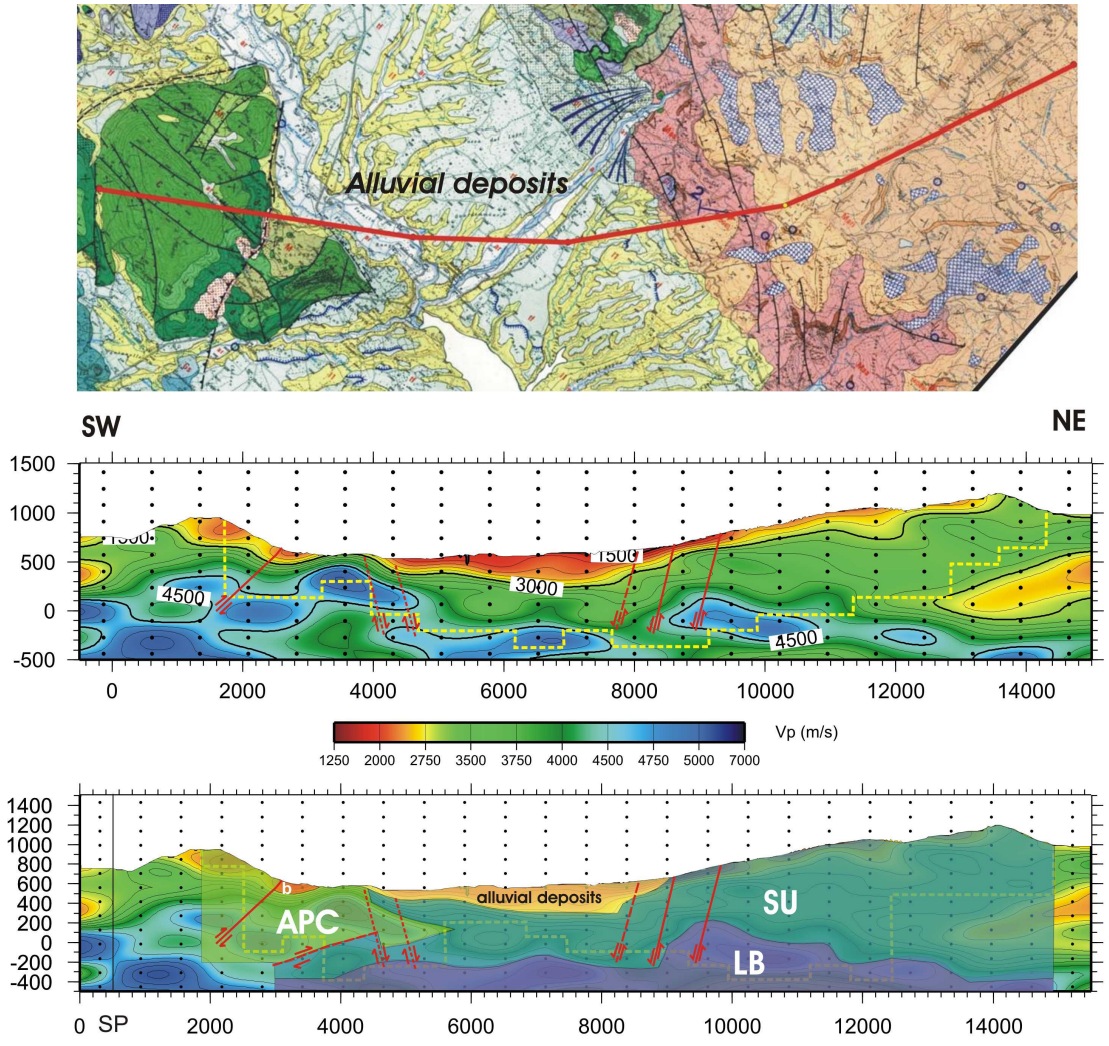

Fig. 3-18. Schematic geological and structural interpretation of the Esit 658 seismic line. The geologic map is from Lentini et al., 1988. b) The velocity model obtained by the last run of the tomographic inversion (25x14f); c) a schematic geologic interpretation of the tomographic image. ACP: Apenninic Carbonate Platform; LB: Lagonegro basin units; SU: Sicilide nappe including Lower-Upper Miocene flysh (Albidona Flysh) and thrust-sheet top deposits (Gorgoglione Fm); b: Bifurto siliciclastics (Lower Miocene); Alluvial deposits (Upper Pleistocene - Holocene.)

The second thrust fault is buried and imaged between 3 and 6 km distance at about 500-800 m depth from the surface. This thrust, about 30° W-dipping, puts the Apennine carbonate Platform above the Lagonegro basin deposits and the overlaying Miocene flysch deposits belonging to the Sicilide nappe, defining the leading edge of the Apennine carbonate Platform in this portion of the basin.

These structures are related to the compressive tectonics affecting the area from Middle Miocene to Lower Pleistocene (Patacca *et al.*, 1990).

Normal fault structures, imaged at both the eastern and the western side of the basin, are related to the ensuing extensional phase. The lateral velocity variation located at about 4200

m distance can be tentatively interpreted as a NE-dipping normal fault structure cutting the pre-existing thrust-fault. To the eastern flank three main SW-dipping fault splays affect the pre-quaternary substratum and the quaternary alluvial deposits. These structures account for a total vertical throw of about 250 m. The normal fault structure located in the inner portion of the basin, at about 8200 m distance has not been mapped before (Lentini *et al.*, 1988).

The presented high-resolution tomographic images will be discussed in the following chapter 4 together with the results of a detailed field work conducted along the Esit700 line.

Chapter 4

Geological mapping and fault kinematics analysis

Introduction

In order to compare *Vp* models and geological data, detailed "target oriented" field survey along the Esit700 profile was conducted. The collected data were used to better constrain geological and structural features of the Val d'Agri basin and, at the same time, to check the geological reliability of the high-resolution tomographic images discussed in the chapter 3 (fig. 3-17).

Fieldwork was basically devoted to two targets: 1) geological mapping; 2) fault-kinematic analysis.

Mapping and structural analysis were conducted at about 100 sites (a map of the data points distribution along the western flank of the basin is shown in fig. 4-1). Data on lithology, bedding attitude, geometry of depositional and tectonic contacts were collected at each outcrop. The observed outcrops were assigned to existing geological formations (both formally and informally established). Field work involved mapping at 1:10.000 scale (base Topographic Maps from 1:25000 scale IGM and 1:10000 scale ortophotos) supplemented by analysis of air photographs.

Outcrops of striated fault planes in bedrock allowed to assess the kinematics of recent faults in the area. We measured both the main fault planes (including lateral variations due to the corrugated nature of the planes) and smaller-size, minor fault surfaces in both hanging-wall and footwall, where available. Outcrops were small (< 300 m^2) compared to the lengths of single fault strands (usually ≥ 5 km).

Fault slip data were analyzed by means of the inversion technique of Marrett and Almendinger (1990), in order to determine the orientation of the principal kinematic axes related to a particular fault population. At least three, but usually more than five, non-parallel striated faults were used for assessing the displacement axes at a specific site and for a specific kinematic episode. Because we are dealing with a predominant extensional regime and a generally plain strain, we focus here on the minimum principal, or extensional, axis.

Detailed fieldwork was imperative along the south-western side of the Esit700 profile (figs. 4-2 and 4-3), where major discrepancies between high-resolution tomographic models (shown in the chapter 3) and previously mapped structural features were found (Lentini *et al.*, 1988; Cello *et al.*, 2003). On the other hand, more reconnaissance mapping was conducted on the eastern side (the investigated area is shown in fig. 3-17 and contoured by a red square).

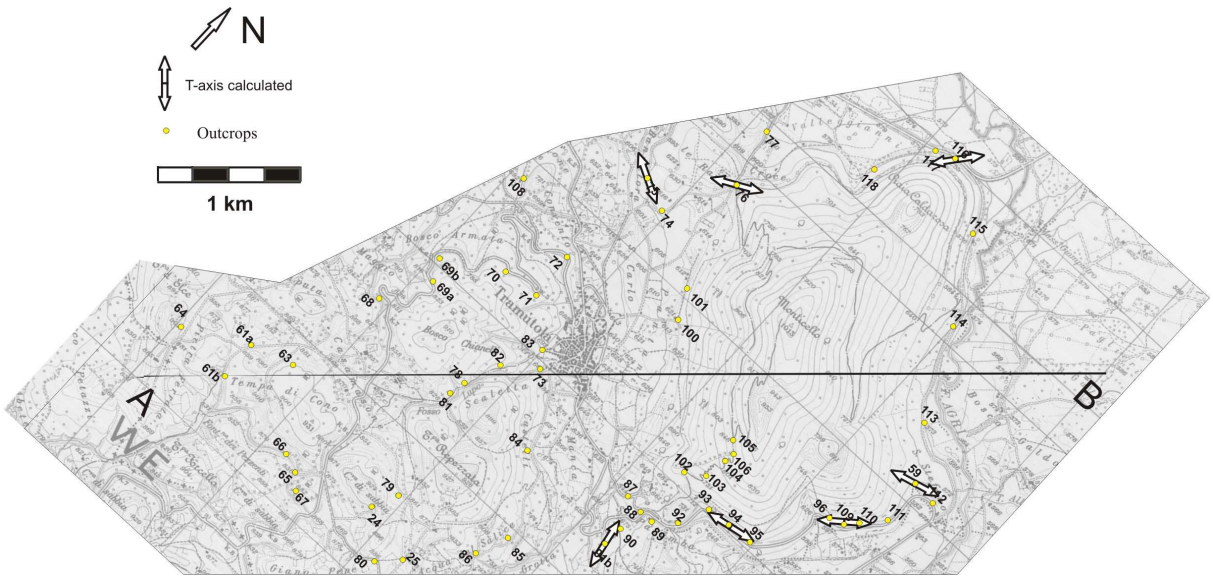

Fig. 4-1. Fieldwork map showing the investigated points (in yellow) and calculated tensile axis.

The geological map of fig. 4-2 corresponds to an area of about 40 km^2 located along the western flank of the Agri basin while the fig. 4-4 shows the geological map of the eastern side of the Esit700 line and cover an area of about 30 km^2.

Field work results

Esit700 South-Western side: Fieldwork started from the south-western end of the Esit700 profile (figg. 4-1, 4-2, 4-3). In this portion of the study area, the highest structural units are represented by Miocene sandstone and marls of the Albidona Formation which sit atop the Monti della Maddalena thrust sheet. The carbonates of the Monti della Maddalena unit overthrust the Lagonegro basinal rocks but, locally, the geometrical relationship is inverted by an out-of-sequence thrust (here named the Tramutola thrust fault) (figg. 4-2 and 4-3). The Lagonegro thrust sheet forms a long-wavelength folded imbricate affected, at the mesoscale, by several minor folds (fig. 4-2). On the SW edge of the Lagonegro thrust-sheet a minor anticline is cut by a NE-dipping fault that represents the projection of NW-trending scarplets in loose deposits outcropping further south (Monte Aquila Fault (Maschio *et al*., 2005)). This NE-dipping fault is not shown in the tomographic images because it is affected by a small cumulative vertical throw (< 50 m) (Maschio *et al*., 2005; Improta & Bruno, 2007) that is beyond the resolution power of seismic data used in this study (fig. 4-7 and 3-17).

Further to the north-east, the Lagonegro unit rocks are in tectonic contact with the Monti della Maddalena carbonates in correspondence of the Tramutola village (figs. 4-2 and 4-3).

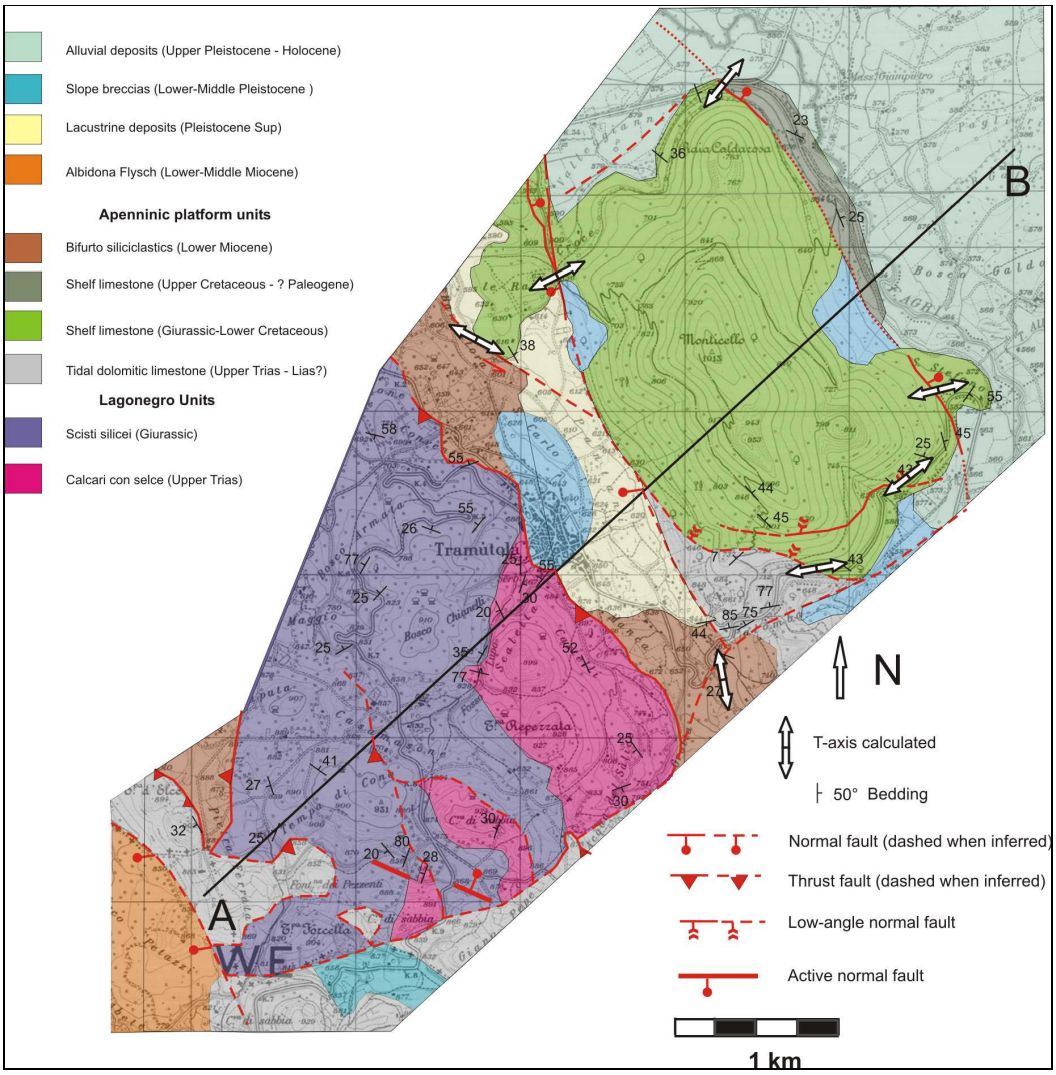

Fig. 4-2. Geological map for the SW portion of the Esit700 profile.

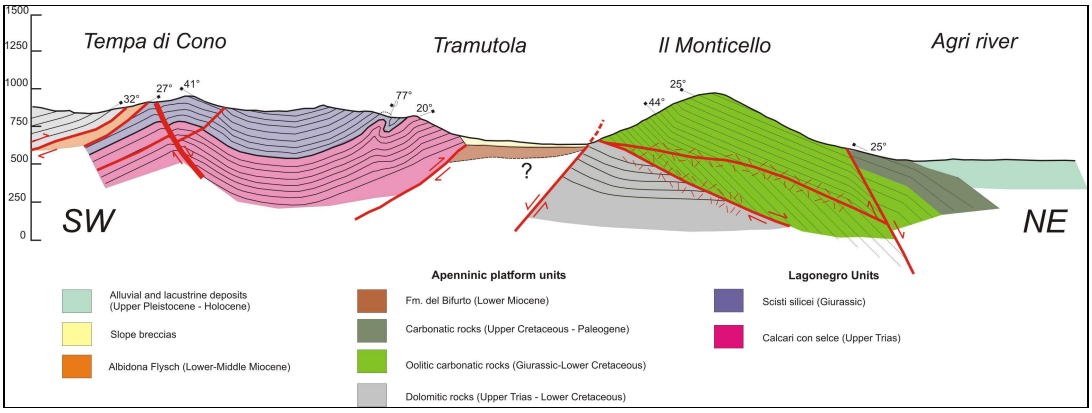

Fig. 4-3. Geologic cross-section of the SW end of the Esit700 line. The trace is shown in fig. 4-2.

Here, the Tramutola thrust fault puts the Lagonegro basinal rocks above the carbonates of the Maddalena unit and the overlying Miocene siliciclastics deposists of the Bifurto Formation, which typically reside stratigraphically above the slope rocks of the Maddalena unit (Lentini *et al.*, 1988). High-resolution seismic tomographic images (described in chapter 3) show a low-velocity wedge dipping beneath the Lagonegro rocks west of Tramutola, and well image the breaching thrust of the Lagonegro units (fig. 4-7).

Further to north-east, Monti della Maddalena carbonates outcrop on the Monticello Hill. The carbonates bedding dips between 40° and 25° to the NE. The Monticello Hill is bounded by several normal-faults. Along the south-western flank of the hill a SW-dipping normal fault down-throws dolomite rocks of the Apennine platform. The fault plane is exposed (for at least 4 m) at the north-western end of the Monticello Hill (outcrop number 76) (fig. 4-2). The inversion of slip lineations for this structure indicates an WSW-ENE oriented extensional axis (fig. 4-6 and table 1, outcrop 76b). Another normal fault bounds the north-eastern flank of the Monticello hill. This NE-dipping structure affects the M.ti Maddalena carbonates and outcrops, with a clear geomorphic expression, at two sites located both at the southern and northern tips of the Monticello Hill (outcrops 116-117 to the north and 59 to the south in fig. 4-1). The structure is characterized by an extensional kinematics with a SW-NE extensional axis (fig. 4-6 and table 1 (116-59)). This normal fault was unknown so far (Lentini *et al.*, 1988) and its existence is supported by the tomogram (fig. 4-7).

The southern flank of the Monticello Hill is characterized by an impressive, about 30° NE-dipping, low-angle brittle shear zone (fig. 4-3). This huge structure continuously outcrops for about 1000 meters along the southern flank of the hill affecting dolomites and carbonates of the Monti della Maddalena unit. The shear zone is composed by several anastomosing cataclasite bands, each characterized by a several m-thick damage zone, where bedding is unrecognizable. Several slip lineations have been used to constrain a SW-NE oriented extensional fault kinematics (figg. 4-3, 4-6 and table 1, outcrop 109). These shear zones cut the carbonate sequence putting younger over older rocks, and are thus characterized by extensional relationships. Similar structures are widespread along the western margin of the southern Apennines (low angle normal faults or LANFs (Ferranti *et al.*, 1996)). In all those examples, huge cataclasite textures, suggestive of deformation under low-confining pressure typical of extensional environments, were observed. High-resolution seismic tomographic images show an unexpected low-velocity zone in this part of the profile, which is likely related to the thick cataclastic shear zone affecting the carbonates (fig. 4-7).

Mesostructural Site	N° measurements	P-axes			T-axes		
		eigenvalue	trend	plunge	eigenvalue	trend	plunge
59 (Monticello SE)	6	-0,3382	182	84	0,3246	75	1.07
76° (Monticello NW)	3	-0,4378	84	64	0,395	282	25
76b (Monticello NW)	5	-0,4025	45	76	0,2397	242	13
91a (Monticello SW)	3	-0,3559	32	70	0,3363	170	15
93 (Monticello SW)	3	-0,3137	308	48	0,1696	192	20
94 (Monticello SW)	3	-0,4743	26	72	0,4486	259	10
109 (Monticello S)	8	-0,3666	264	81	0,3292	52	7
116 (Tramutola)	4	-0,3754	291	48	0,3213	38	14
117 (Tramutola)	4	-0,3809	214	58	0,3782	92	18
122 (eastern border)	4	-0,3016	288,2	83,5	0,2472	143,1	5,4

Table 1: Site averaged kinematic axes derived from mesoscale fault population data

North-eastern side: Figg. 4-4 and 4-5 show a schematic geologic map and cross-section of the NE sector of the Esit700 profile. The structural setting of this part of the Esit700 profile is characterized by the overthrust of the carbonates of the Maddalena unit above the Lagonegro unit rocks. During Quaternary, this compressive structure was affected by stike-slip and extensional tectonics that formed four SW-dipping normal faults. The vertical throw of the single faults has been constrained using tomographic images and exploration wells published by Dell'Aversana (2003) (figg. 4-5, 4-8).

Starting from the south-western end of the section, alluvial to lacustrine deposits of the Agri fluvial system outcrop. They depositionally overlie slope breccia deposits, that extensively outcrop in the piedmont zone and that reach about 440 m thickness in this eastern portion of the basin (fig. 4-5). The slope breccia thickness is well constrained by published well data (Dell'Aversana, 2003) as well as by the tomographic images (fig. 4-8). This piedmont zone is affected by two SW-dipping normal faults (fault 1 and 2 in fig. 4-5) producing about 100 m and 400 m of vertical throws, respectively (fig. 4-5 and 4-8). These two faults are not clearly detectable on the alluvial fan and breccia deposits outcropping along the Esit700 profile. For this reason there are neither fault plane nor slip lineation data for these structures. However, according to the tomographic images, in the reconstruction of the map and cross-section shown in figg. 4-4 and 4-5 these structures have been drown as inferred.

More in detail, the fault 1 affects the carbonates of the Monti della Maddalena unit and at shallow depth the slope breccia deposits as testified by the sharp lateral velocity variation shown by the tomographic image at about 8200 m distance (see fig. 4-7). Nonetheless, the absence of this fault at the outcrop suggests that the more recent deposists are not involved in faulting.

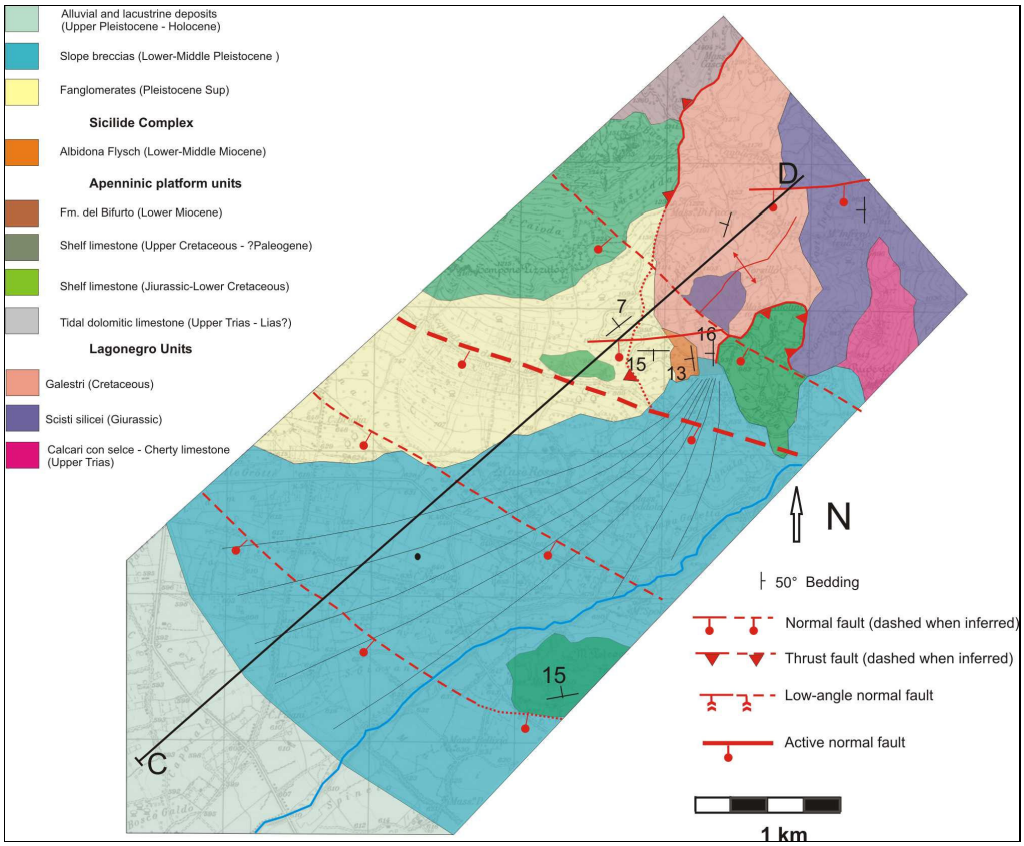

Fig. 4-4. Schematic geological map along the NE portion of the Esit700 profile.

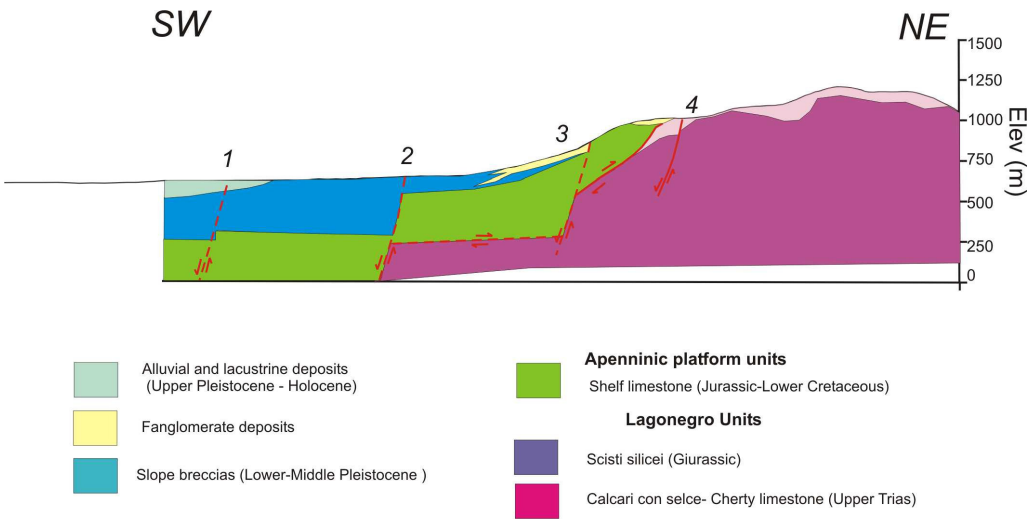

Fig. 4-5. Schematic cross-section of the NE end of the Esit700 line. The trace is shown in fig. 4-4. The vertical throws of the normal faults have been calculated based on tomographic images and exploration wells (Dell'Aversana, 2003).

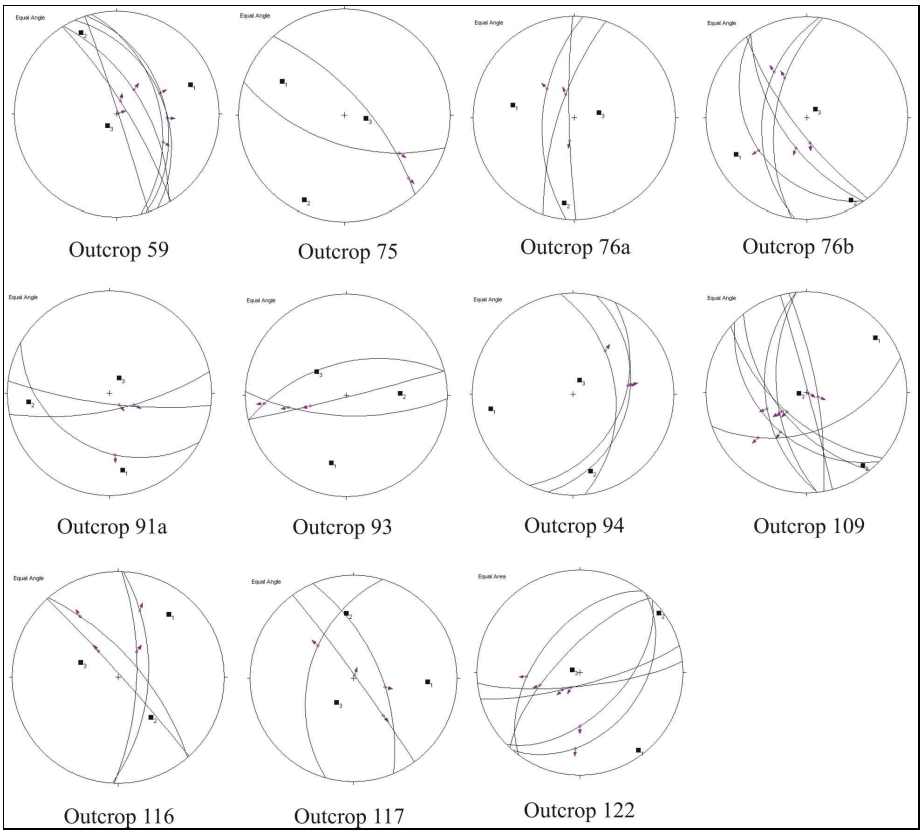

Fig. 4-6. Fault and slip lineations for fault population data at mesostructural analysis along the Esit700 mapping swath (see location in fig. 4-1). More information are listed in table 4-1.

Fault 2 position (figg. 4-5 and 4-7) correlates this fault with those reported by Lentini *et al*., (1988) and Cello *et al*., (2003) close to the Villa d'Agri village. For this fault Cello *et al*., (2003) report a fault zone exposed for a length of about 3 km and estimate a 100-250 m of morphological displacement.

However, according to the tomographic images, in the reconstruction of the map and cross-section shown in figg. 4-4 and 4-5 these structures have been drown as inferred.

Moving uphill slope breccias grade into low-thickness well-cemented alluvial fan deposits. Another fault splay (fault 3), affecting carbonates of the Monti della Maddalena unit, is reported in the section; this splay correspond to a fault plane well-exposed few hundreds meters to the south of the section, which produces about 1 m vertical throw at the surface (Gambini, 2003). This fault is positively imaged by the tomograms showing an abrupt lateral Vp variation around 10.4 km, corresponding to the contact between carbonates of the Apenninic Platform and basinal rocks of the Lagonegro unit (Scisti silicei and Galestri) (fig. 4-8). This fault probably offsets also the thrust surface by 100-150 m (fig. 4-8).

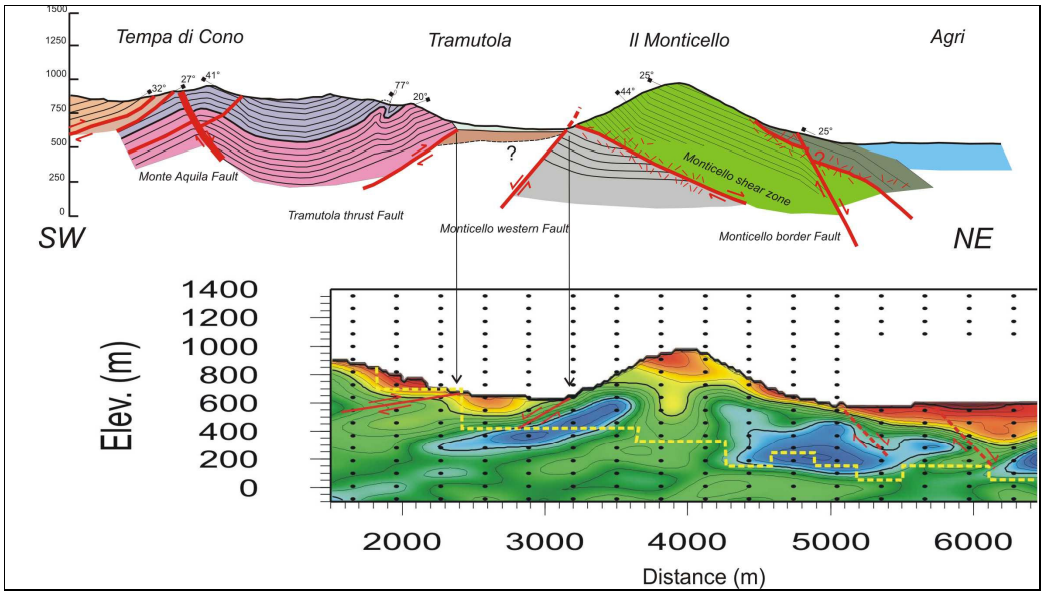

Fig. 4-7. Comparison between the schematic cross-section along the SW end of the Esit700 line and the tomographic model.

Further to north-east the carbonates of the Monti della Maddalena unit are thrust over the Lagonegro basin rocks. The carbonates dip about 10° toward NW (fig. 4-4). The thrust fault dips about 30° to SW and is not clearly exposed at the surface. However, bedding-fault cutoffs allow to reconstruct the leading-edge hanging-wall anticline. The hanging-wall rocks are cataclastic, and this could explain the low-velocity encountered at the tip of the carbonate structural sheet (fig. 4-8). Lagonegro basinal rocks are involved in SW-asymmetric folding which have been already studied north of this area (Mazzoli *et al.*, 2001) (fig. 4-5). These backfolds are clearly shown in the tomogram (fig. 4-8). The thrust structure is cut by a fourth normal fault splay characterized by a low-vertical throw (figg. 4-5, 4-8).

Discussion

The 2D tomographic images, complemented by new acquired structural and kinematic data, yields valuable constrains on the shallow structure of the Agri basin down to 1000 m depth, allowing the interpretation of the geological and structural setting of the basin and providing new insights on the recent tectonics in the area.

The shallow structural architecture of the basin seems partly inherited by the previous (Mio-Pliocene) thrust displacements, but largely controlled by Quaternary high angle normal faults, that cut both the bedrock and the basin fill on both sides of the basin.

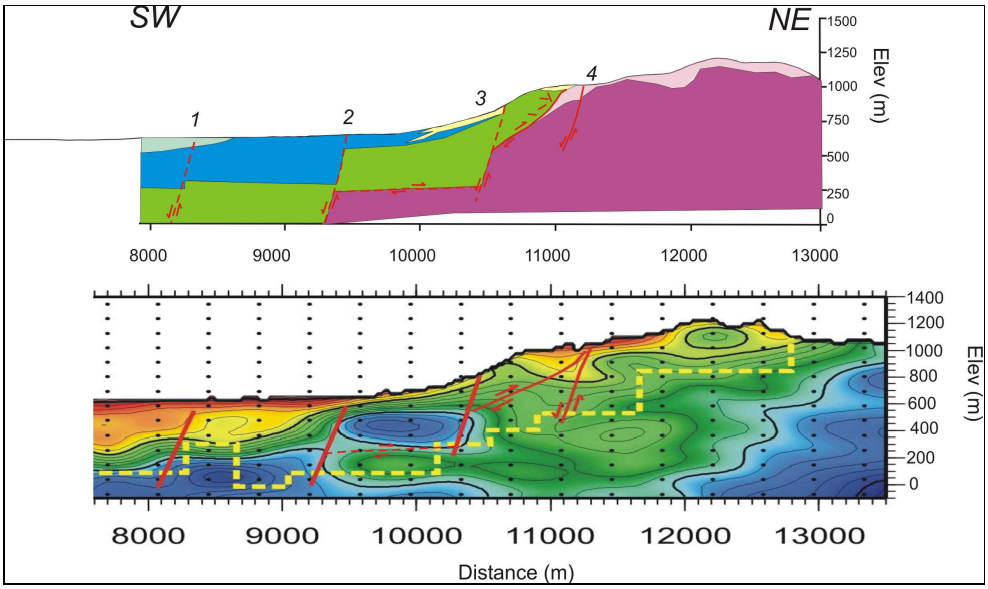

Fig. 4-8. Comparison between the schematic cross-section along the NE end of the Esit700 line and the tomographic model.

Very strong lateral velocity variations are indicative of normal-faulting structures. Those located along the eastern flank of the valley are well-known in literature and correspond to the SW-dipping strike-slip, locally reactivated in dip-slip Eastern Agri Fault System (Cello *et al.*, 2000-2003; Giano *et al.*, 2000; Maschio *et al.*, 2005). This system is characterized by a mature geomorphic expression and by a regularly spaced array of 4 fault splays; its activity accounted for the deposition of about 400 m of Lower-Middle Pleistocene slope breccias and conglomerate deposits along the eastern side of the basin, reflecting coeval SW-dipping faulting activity with a depocenter located at about 8 km distance (fig. 3-17). Recent deformation along this fault system is documented by paleosoils involved in faulting during the last 39-18 ka (Giano *et al.*, 2000) and by surface offsets (Gambini, 2003). This fault system is, therefore, considered by many authors (Benedetti *et al.*, 1998; Cello and Mazzoli, 1999; Cello *et al.*, 2003; Barchi *et al.*, 2006) the morphological expression of the seismogenic source responsible of the historical and ongoing seismic activity of the area.

The tomographic images also show NE-dipping normal faults along the south-western flank of the valley (fig. 3-17). These normal-faulting structures affect the carbonates of the Monti della Maddalena unit. This fault system is partially covered by continental deposits.

This could explain why it was never mapped before despite of intense field surveys conducted in the area (Lentini *et al.*, 1988; Cello *et al.*, 2003; Maschio *et al.*, 2005).

Therefore, our results are consistent with the hypothesis, mainly based on morpho-tectonic data, of NE-dipping normal faults located along the western side of the basin. Maschio *et al.*

(2005) speculate that since the Middle Pleistocene *p.p.*, deformation in the Val d'Agri area was concentrated on the MMFS, as suggested by scarplets in loose deposits, by fault control on the hydrographic pattern of the Agri river, and on the mountain landscape (figg. 3-17). The recent control played by the MMFS on geomorphic and sedimentary features is typified by the westward shift of the Agri alluvial system, also highlighted in the tomographic models by the depocenter located around 6 km distance, probably active since Middle Pleistocene up to the present (fig. 3-17). The presence of a second, more recent depocenter, beneath the western border of the Agri basin is also supported by electrical resistivity tomographies (Colella *et al.*, 2004).

According to tomographic images and field surveys, it cannot be ruled out any of the two formulated hypothesis about the most recent activity of these fault systems; the fault geometry at depth is, in fact, not imaged by this type of data and definitely it is impossible to assign a hierarchy between fault systems. Many Authors mostly prefer the hypothesis of a SW-dipping normal fault and rule out the alternative one. Nonetheless, the presented results document a most recent control on basin sedimentation by the NE-dipping fault system, which is consistent with new microseismicity data collected in the area (see chapter 2 for an exhaustive treatment).

Chapter 5

3-D velocity (V*p* and V*p*/V*s*) crustal structure of the Val d'Agri area

Introduction

In this chapter I present three-dimensional *Vp* and *Vp/Vs* models of the upper crustal structure (down to 12 km depth) of the Val d'Agri area, obtained by inverting P and S arrival times from 667 local earthquakes recorded by up to 50 seismic stations.

Local Earthquake Tomography (LET) is a widely used inversion technique (Aki and Lee, 1976, Thurber, 1983; Eberhart Phillips and Micheal, 1993, 1998; Amato *et al*., 1992; Chiarabba and Amato, 2003, among many others). The basic assumption of LET is that the arrival time of a seismic wave at a seismic station depends on the time at which the wave originated (origin time), the source location and on the velocity structure of the medium travelled by the seismic rays between the seismic source and the station. Thus we can invert the travel time residuals (the differences between observed and predicted travel times) to find the best three-dimensional velocity structure.

Local earthquakes tomography represents a basic tool to reconstruct the three-dimensional velocity structure in seismically active areas. In particular, the integration of surface geology, *Vp* and *Vp/Vs* models and accurate 3D hypocentral locations is a powerful tool to study the subsurface structural setting in seismogenic areas and to constrain location and geometry of active faults (Thurber, 1983; Amato *et al*., 1992; Chiarabba and Selvaggi, 1997; Chiarabba *et al*., 1997; Michael and Eberhart-Phillips, 1991, Chiarabba and Amato, 2003).

Moreover, earthquake focal mechanisms, source moment tensors, inversion for anisotropy or attenuation, and any other calculations relying to the geometry of seismic wave ray paths within and near the fault zone, all depend critically for their accuracy on a realistic 3D velocity model for *P* and *S* waves (Michelini and McEvilly, 1991).

Inversion procedure

The LET inversion technique used in this work is the linearized iterative Simulps-13q inversion procedure developed originally by Thurber (1983) and Um and Thurber (1987) and modified by Eberhart-Phillips (1993) and Eberhart-Phillips and Reyners (1997). *P* and *S* first arrival times are simultaneously inverted for both earthquake locations and velocity model parameters, at each step of the inversion procedure. The importance of coupling earthquake hypocenter parameters on one hand, and velocities on the other, has been discussed by Thurber (1992) who emphasized that all required parameters should be mutually consistent to

avoid significant bias in the derived models. Initial development of the simultaneous inversion technique were due to Crosson (1976) and Aki and Lee (1976). The approach followed in these studies was later modified in applications by numerous authors. The fundamental improvement added to the inversion procedure, in respect with previous algorithms is the use of approximate ray tracing, to calculate *P*-wave arrival times, instead of the three dimensional ray tracing procedure, a very costly procedure for use in iterative simultaneous inversion problems (Thurber, 1983). An important consequence is the ability to measure directly the model improvement achieved via the inversion by computing travel time residuals after each iteration. An additional practical improvement is the use of parameter separation (Pavlis and Booker, 1980) which allows the inclusion of large amounts of data in order to better constrain the models.

The inversion process starts with the initial estimate of the velocity model, origin times and hypocenters. These hypocentres and velocity parameters are iteratively adjusted in order to minimize the difference between the observed and calculated arrival times for each source at each station.

We prefer to obtain *Vp* and *Vp/Vs* models rather than *Vp* and *Vs* models since *Vp/Vs* models are more easily interpretable in terms of rock properties and rheology (Eberhart-Phillips and Micheal, 1998). The great advantage of this inversion techniques is the direct computation of 3D *Vp/Vs* model by using S-P times, instead of obtaining such values from the differently resolved *Vp* and *Vs* models.

Matematical formulation

The body-wave travel time *T* from an earthquake *i* to a seismic station *j* is expressed using ray theory as a path integral:

$$T_{ij} = \int_{source}^{receiver} \frac{1}{v(x,y,z)} ds$$

where v(x,y,z) is the velocity function, *ds* is an element of path length, and the line integral is calculated along the ray path. For the LET, the actual observations are the arrival times t_{ij} :

$$t_{ij} = \tau_i + T_{ij}$$

where τ_i is the earthquake origin time. The only known data in the LET problem are the receiver locations and the observed arrival times. The source coordinates (x_1, x_2, x_3), origin times, ray paths and slowness field are unknown and represent the model parameters.

Given a set of arrival times t_{ij}^{obs} measured at a network of stations (times of first P and S waves arrival times), the calculated arrival times t_{ij}^{cal} are determined from equations (1) and (2) using trial hypocenters and origin time and an initial minimum 1D velocity model. The misfit between observed and calculated arrival times are the residuals r_{ij}:

$$r_{ij} = t_{ij}^{obs} - t_{ij}^{cal}$$

The residuals can be related to perturbations of hypocenter and velocity parameters by a linear approximation:

$$r_{ij} = \sum_{k=1}^{3} \frac{\partial T_{ij}}{\partial x_k} \Delta x_k + \Delta \tau_i + \sum_{n=1}^{N} \frac{\partial T_{ij}}{\partial m_n} \Delta m_n$$

where m_n are the N parameters of the velocity model, dT_{ij}/dx_k are the variations of T with respect to hypocentral coordinates and $\Delta\tau_i$ with respect to the origin time, dT_{ij}/dm_l are the variations of T with respect to the model parameters, and Δx_k , Δm_l are the unknown parameters.

Model parameterization: the crustal model is parameterized assigning suitable initial velocities to each node of a three-dimensional grid and is linearly interpolated through the medium. It is worth noting that assessing the most suitable parameterization in seismic tomography is an important task since it controls the final solution as well as its reliability.

Forward problem: the forward problem is solved by using an approximate ray tracing technique proposed by Um & Thurber (1987). A large number of circular arcs connecting the source and receiver are constructed and the travel time along each arc is computed using the three-dimensional velocity model. Arcs of varying radii of curvature are examined (see figure 5-1). The dip of the plane connecting the arcs is varied systematically in order to sample thoroughly the volume of interest. From this large set of arcs, an approximation to the true first arrival ray path is selected on the basis of the shortest travel time.

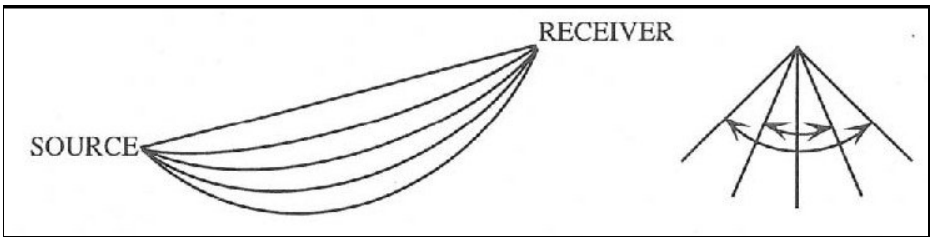

Figure 5-1. Approximate ray tracing scheme showing circular paths of different radii of curvature and the plane containing the paths (rotated about the source-receiver axis). The path with the shortest travel time is adopted as the best estimate of the true ray path. (From Thurber, 1983).

Inverse problem solution:

In the matrix notation, the linearized inversion equation can be written:

$$d = Gm$$

where d is the residual vector, m is the parameters perturbation vector, and G is the kernel of the partial derivatives. The equation (4) (i.e. the solution of model parameters) is solved using a damped least square inversion:

$$m = (G^T G + \theta^2 I)^{-1} G^T d$$

where θ is a damping parameter added to the diagonal of the medium matrix to avoid artificial small-scale velocity variations due to small eigenvalues of G, and I is the identity matrix.

Resolution: The reliability of the obtained *Vp* and *Vp/Vs* velocity models has been verified by a complete formal analysis of the resolution matrix (see Menke, 1989; Toomey and Foulger, 1989; Michelini and McEvilly, 1991). Model resolution depends on the data quality, grid-node spacing and ray sampling within the volume. It is well known that the use of a coarse grid yields formally well resolved velocity parameters at the expense of spatial aliasing of anomalies into the parameter space (see Toomey and Foulger, 1989). The resolution matrix R (Menke, 1989) is a square matrix with MxM dimensions, where M is the number of the inverted model parameters:

$$R = (M^T M + \theta^2)^{-1} M^T M$$

This matrix describes the distribution of information for each node, such that each row is the averaging vector for a parameter. Diagonal elements of the resolution matrix vary from 0 (no resolution) to 1 (full resolution). The relative size and pattern of the off-diagonal elements show how the information is smeared. For a node to be adequately resolved, its resolution should be peaked and should have no significant contribution from off-diagonal nodes.

An effective representation of the resolution and the smearing of some node is the *Spread Function* which compresses each row of the resolution matrix into a single number that describes how much is strong and peaked the resolution for that node (Toomey and Foulger, 1989; Michelini and McEvilly, 1991). As described in detail by Toomey and Foulger (1989) the spread function is a better way to describe the resolution than by solely examining the diagonal element, since the diagonal resolution is very dependent on the grid spacing and damping. As defined by De Gori *et al.* (2005), the spread function Sj for a node is computed from the all elements s_{kj} of the corresponding row of the resolution matrix, weighted by their distance D_{jk} from the node, and sj is the diagonal element.

$$S_j = \log\left[|r_j|^{-1} \sum_{K=1}^{N} \left(\frac{r_{jk}}{|r_j|} \right)^2 D_{jk} \right]$$

For the same dataset, Spread Function values vary within a range controlled by the grid node spacing and damping parameters. The greater is the distance between node pairs, the higher is the Spread Function. For higher damping values, the Spread Function increases. Generally, a well defined model parameter has a value of the Spread Function smaller than the grid spacing.

Three-dimensional inversion: geometry and resolution

Three-dimensional *Vp* and *Vp/Vs* images of the upper crust in the Val d'Agri area (Southern Apennines seismic belt), down to 12 km depth, were computed by traveltime inversion of P (9269) and S (8726) waves from about 667 local earthquakes, recorded at a maximum 50 stations, selected according to RMS time residuals less than 1 s, azimuthal gap less than 200°, hypocenters formal errors less than 1 km and at least 8 *P*-wave readings. The distribution of stations/events allowed to investigate a volume about 40 x 50 x 12 km^3.

The medium is parameterized by assigning to a 3D grid the initial 1D velocity model (see chapter 2). Assessing the most suitable parameterization in seismic tomography is an important task since it controls the final solution as well as its reliability. For this reason, we try different parameterizations before choosing the grid spacing showed in figure 5-2.

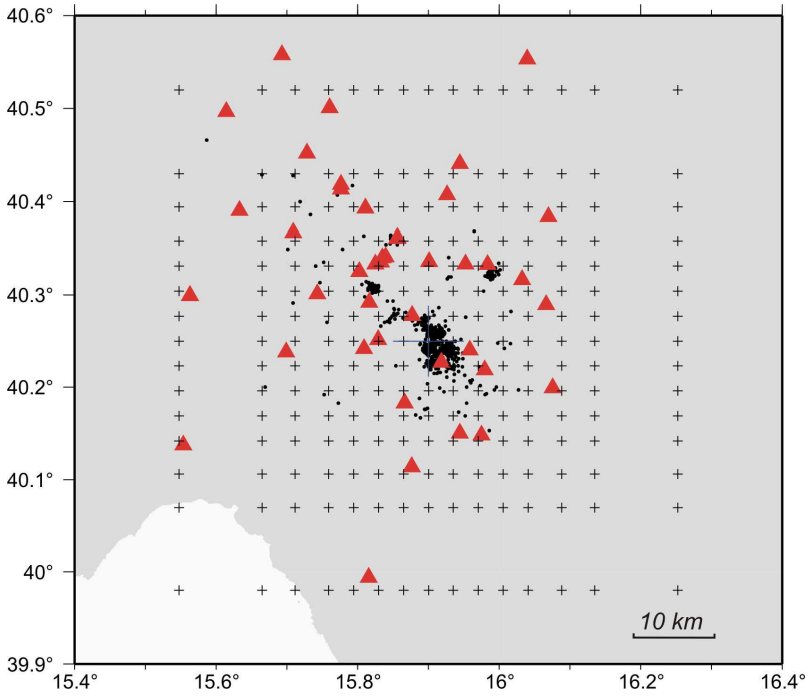

Fig. 5-2. Seismic stations and model parameterization. Triangles represent the stations of the local network. Black dots are seismic events relocated with the 3D model. Crosses are the inversion nodes.

The horizontal grid area is 50 km both in X and Y directions with a node spacing of 3 km in the central part of the grid and 10 km in the less resolved model periphery. In the vertical direction, the model is divided into six layers located at 0, 3, 6, 9, 12 and 15 km depth.

Following the suggestion of Eberhart-Phillips (1986) the damping parameters is chosen empirically, by evaluating the trade-off curve between data variance and model roughness (fig. 5-3). An under estimated damping parameter results in noise contaminated high variance anomalies, while over estimated damping reduces real lateral velocity variations. To find the best damping parameter a series of single-iteration inversions with a wide range of damping values has been run. Values of 30, 45 and 60 are chosen for the *Vp*, *Vp/Vs* models and station corrections respectively, due to a significant reduction of the data variance with only a moderate increase of the model roughness (figure 5-3). The initial *Vp/Vs* value (1.90) is calculated from Wadati diagram (see chapter 2).

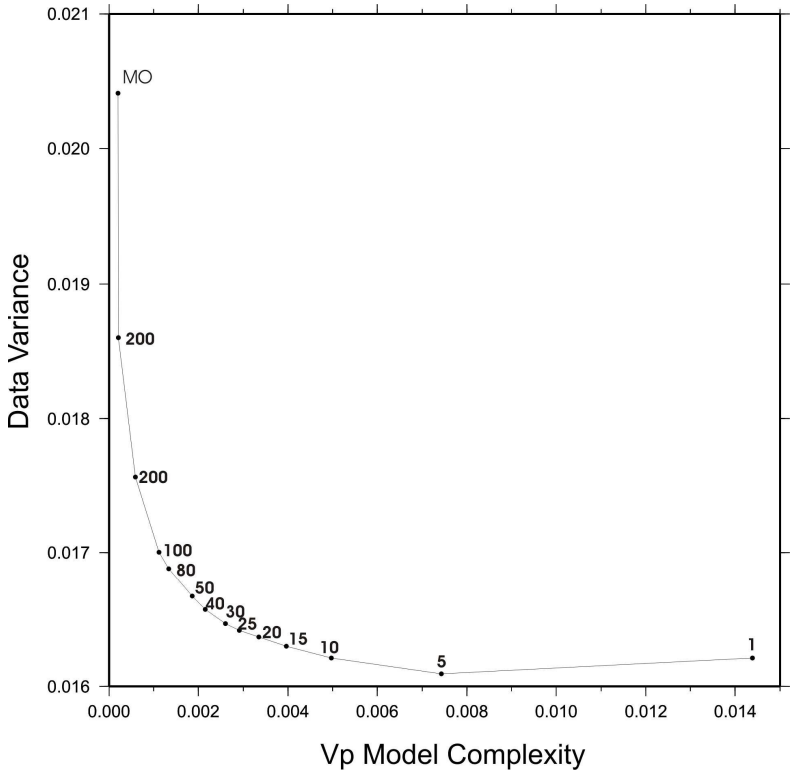

Fig. 5-3. Trade-off curve between variance and model lenght. The selected *Vp* damping parameter is 30.

The 3D *Vp* and *Vp/Vs* models and hypocentral locations were obtained after 4 iterations with a final reduction of the data variance of 36% (from 0.023 s to 0.014 s). During the inversion, weighting is applied to each observation (ray path), based on observation quality, source-receiver distance and size of residual.

After an accurate inspection of the spread function values and of the direction of smearing for each inverted node of the *Vp* and *Vp/Vs* models, the Spread Function value equal to 2 was considered a suitable choice as representing well resolved nodes.

Three-dimensional inversion: results

Figure 5-4 shows the computed *Vp* and *Vp/Vs* models at 0, 3, 6, 9 and 12 km depth, with the three-dimensional relocated events. The well-resolved area is defined by the SF $\leq$ 2 (white and black line in the *Vp* and *Vp/Vs* layers, respectively). Resolution is high down to 6 km depth with a maximum at 3 km depth, and rapidly decreases at 9 km depth and below.

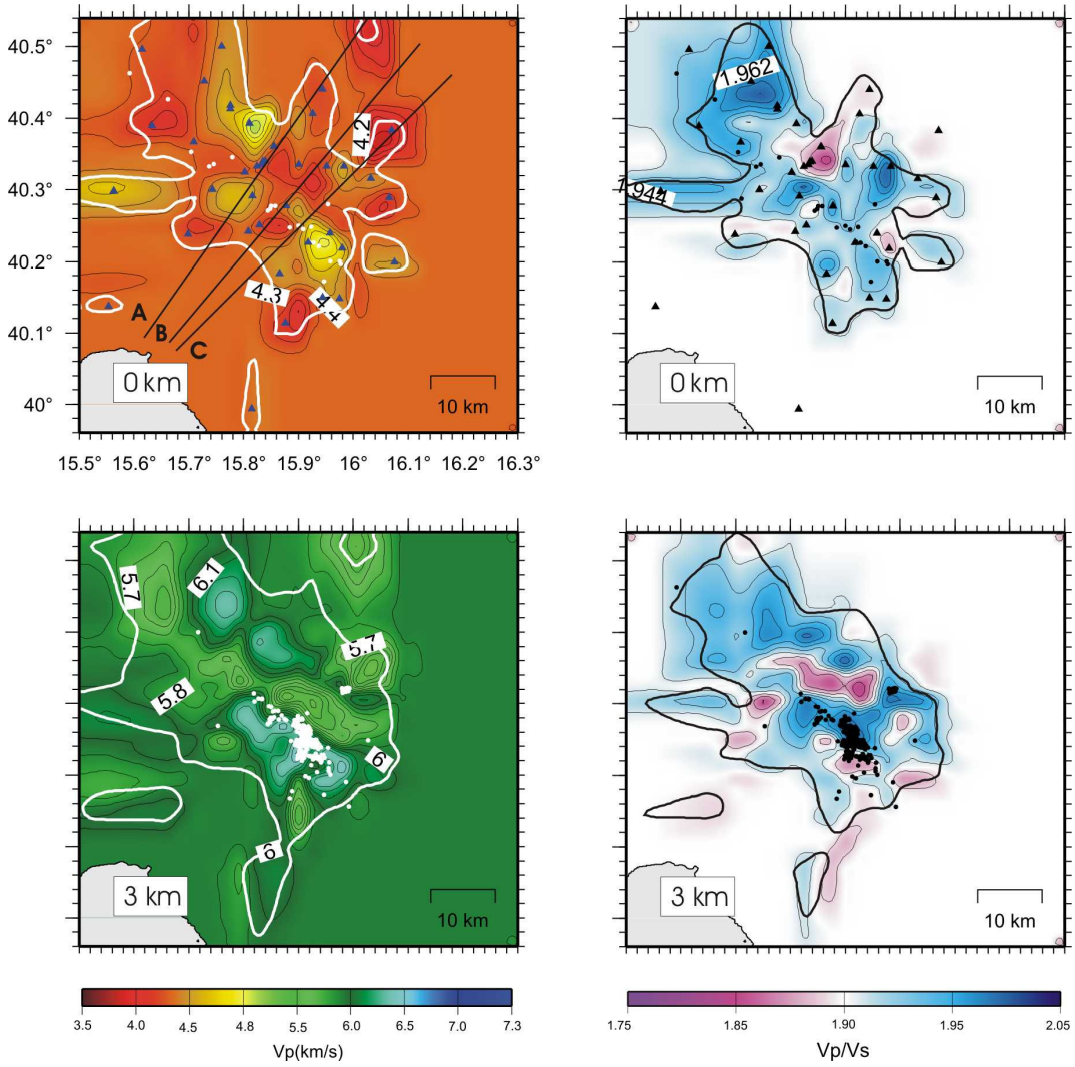

Fig. 5-4. Three-dimensional *Vp* (left) and *Vp/Vs* (right) models. The white and black contours represent the volume comprising nodes with SF<= 2, on the *Vp* and *Vp/Vs* layers, respectively. White (*Vp*) and black (*Vp/Vs*) dots are the relocated earthquakes. On the 0 km layer, the position of the cross-sections discussed in fig. 5-6 is shown.

P-wave velocities vary between 4.0 km/s and 7.0 km/s while *Vp/Vs* ratio ranges between 1.85 and 1.98, variations consistent with those found in regions of active tectonics (Zhao and Kanamori, 1995; Thurber, 1995; Zhao and Negishi, 1998; Chiarabba and Amato, 2003).

At 0 km depth, (fig. 5-4) the complex pattern of the *Vp* and *Vp/Vs* anomalies testifies the highly variable surface geology of the area. A low-velocity anomaly (*Vp* < 4.3 km/s) is found in the central portion of the model, extending NW-SE beneath the Agri basin. Regions characterized by *Vp* greater than 4.3 km/s (i.e. high velocity anomalies) correspond to areas where carbonates of the Apennine platform outcrop. The shape of the *Vp/Vs* anomalies is

complex and characterized by a predominance of high *Vp/Vs* zones within and outside the basin. Two very high *Vp/Vs* anomalies (up to 1.96) are located in the northern and eastern portion of the model (fig. 5-4). Another high *Vp/Vs* anomaly is located in the northern-western sector of the basin. The few earthquakes projected on this layer are located along the south-western portion of the basin.

At 3 km depth, the pattern of *Vp* and *Vp/Vs* anomalies is more regular. The *Vp* model shows a NW-striking low-velocity anomaly (*Vp* < 5.9 km/s) in correspondence of the Agri basin, bounded at both the north-eastern and south-western border by two very high *Vp* bodies (*Vp* up to 6.2 km/s). These high-velocity anomalies trend NW-SE and a rotation to the north is observed in the northernmost anomaly. The high *Vp/Vs* anomalies (with *Vp/Vs* value up to 1.98) show a very good match with the two NW-SE striking high *P*-wave velocity anomalies. Earthquakes are clustered beneath the south-western side of the Agri basin in correspondence of a high *Vp* and high *Vp/Vs* region.

At 6 km depth, a broad positive velocity anomaly is found in the central area of the model with spots of high *Vp* (*Vp* up to 6.6 km/s), slightly elongated in the NW-SE direction. These anomalies have low *Vp/Vs* values (down to 1.83). A low *Vp* anomaly characterized by high *Vp/Vs* values (*Vp* less than 6.2 km/s and *Vp/Vs* value up to 1.95) is located along the eastern portion of the well-resolved region in correspondence of a small cluster of seismicity. Few earthquakes are located along the south-western portion of the Agri basin in correspondence of a high *Vp* and low *Vp/Vs* region.

Below this depth, the model resolution rapidly decreases due to the very low number of deep earthquakes. At 9 km depth, the central portion of the model shows a region with a positive *Vp* anomaly (*Vp* up to 7 km/s) and negative *Vp/Vs* anomaly (*Vp/Vs* less than 1.85). The earthquakes occurring at this depth are scarse. At 12 km depth, *P*-wave velocity is generally lower than those found at 9 km depth; this feature is inherited from the 1D velocity model. The well-resolved region is very small and limited to the occurrence of two small clusters of events located at this depth. The *Vp/Vs* model shows a negative anomaly region (*Vp/Vs* less than 1.85).

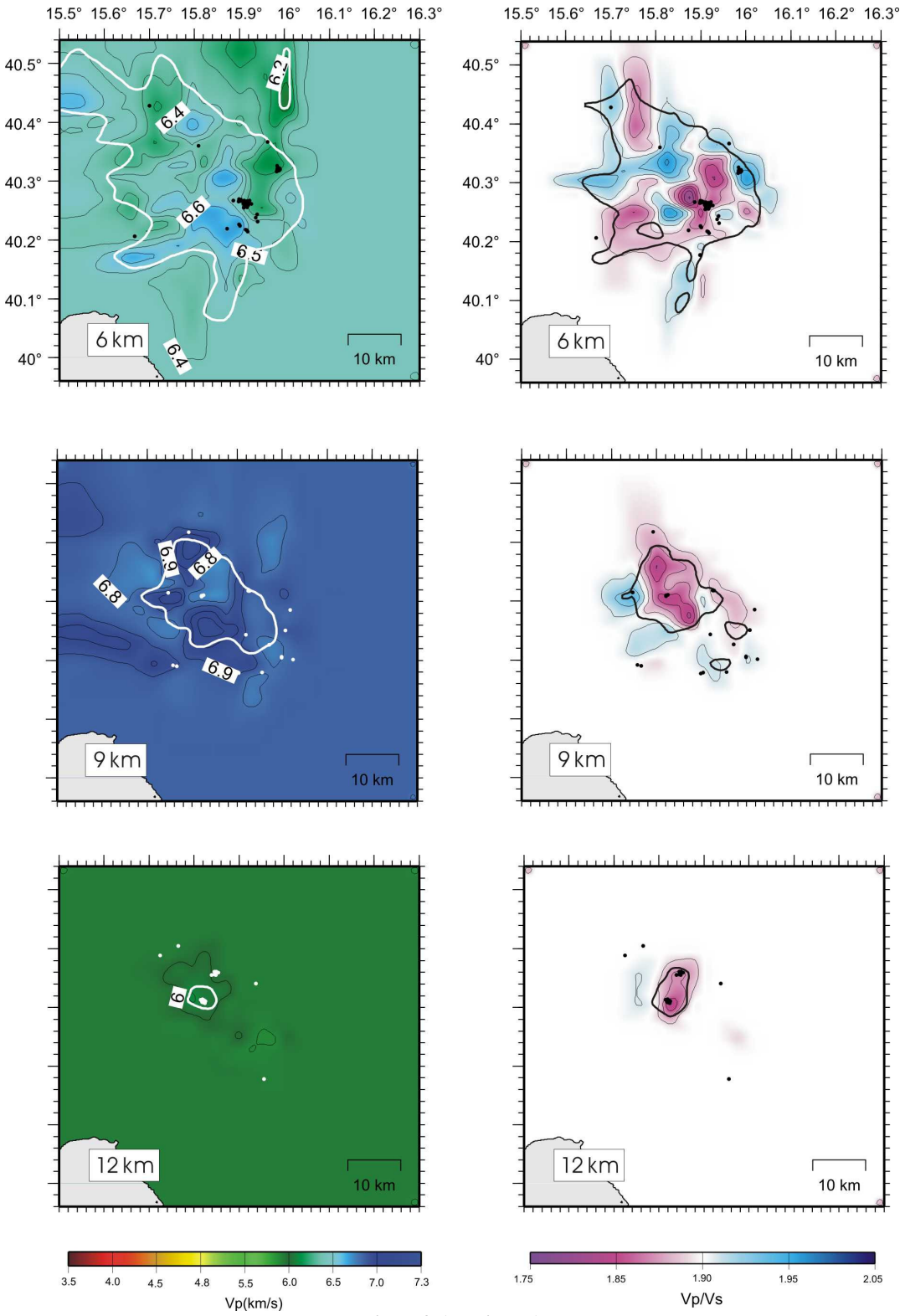

Fig. 5-4. (continued)

Three-dimensional earthquake locations

Earthquakes relocated with the obtained 3D velocity model are more clustered and slightly shallower with respect to the 1-D located ones showed in the chapter 2. Three-dimensional hypocentral locations are affected by lower horizontal and vertical formal errors and RMS values. RMS value is in average less than 0.1 s, with 50% of events with final RMS smaller than 0.05 s. Horizontal and vertical hypocentral formal errors are less than 0.3 km. The relationship between earthquake occurrence and crustal structure will be clarified in the following section along with the *Vp* and *Vp/Vs* upper crustal models.

***Vp* and *Vp/Vs* models interpretation**

Before proceeding to the geological and structural interpretation of the obtained *Vp* and *Vp/Vs* models it is necessary to bear in mind some considerations.

The structural interpretation (structure position and geometry) of the three-dimensional velocity models is not unique, due to the smoothing effect (as the velocity at a given point is determined by interpolation among the surrounding grid points) and the limited resolution in the marginal zones. Furthermore, since the velocities are linearly interpolated in the three spatial directions, sharp velocity gradients are an expression of horizontal and vertical discontinuities, indicating the location and geometry of the faults (Eberhart-Phillips and Michael, 1993; Chiarabba and Amato, 1994). However, the lateral resolution of the velocity models computed with the chosen model parameterization (a node every 3 km in the central part of the model), is on the order of 1.5 to 3 km, indicating that higher frequency heterogeneity is almost completely lost.

Previous tomographic studies in Italy have shown that the main factor affecting *P*-wave velocity in the upper crust is the lithological variation (Chiarabba and Amato, 2003 and reference therein).

Positive velocity anomalies can be related to anticlines or horsts. Thrusts can be distinguished as low angle velocity contrasts flanked by positive velocity anomalies above, and normal or negative velocities below, indicating thrusting of rock units over adjacent formations. Quaternary basins usually appear at the model surface layer as local low velocity anomalies. In vertical sections, these basins are usually bounded by relatively high angle, lateral velocity contrasts, representing the major normal faults, responsible for the formation of these basins.

In the southern Apennines, the comparison between stratigraphic and sonic velocity logs form deep wells, seismic refraction profiles, laboratory data, and seismic tomography models, results in *P*-wave velocity ranges for lithologies composing the upper crust (Chiarabba and

Amato, 1997; Iannaccone *et al*., 1998; Improta *et al.*, 2000, 2003; Bisio *et al.*, 2004; Improta and Corciulo, 2006).

Plio-Quaternary basin-filling sediments have *P*-wave velocities ranging between 2.0 and 3.0 km/s. *Vp* up to 4.5 km/s are found for Mesozoic-Cenozoic deep water silicoclastic deposits of the Lagonegro basin, while *Vp* values up to 5.5-6 km/s for carbonates of the Apennine platform (see also *P*-wave velocities shown in the high-resolution tomographic models for the shallow upper crustal structure in chapter 3). At greater depth, *Vp* in the range between 6 and 6.6 km/s are interpreted as Meso-Cenozoic carbonates of the Apulia Platform. Velocities as high as 6.7–7.0 km/s have been attributed to the Triassic successions (anhydrites and dolomites) of the Apulian platform (Iannaccone *et al*., 1998; Improta *et al*., 2000; Bisio *et al*., 2004; Bagh, 2006). Finally, a lower *P*-wave velocity is hypothesized at greater depth and has been loosely related to the Permo-Triassic clastic deposits drilled at the bottom of the Apulia platform in the foreland area (Shiner *et al.*, 2004; Butler *et al*., 2004). Figure 5-5 shows a simplified stratigraphic log of the Puglia 1 well drilled in the Apulian foreland.

Vp/Vs variations are related to rock properties, rheology, fluid type and saturation degree. In particular, within a fault zone, *Vp/Vs* is mostly controlled by a different level of cracking in the subsurface rocks and fluid pressure at depth (Zhao and Negishi, 1998 and references therein). In liquid-phase filled rocks, an increase of the *Vp/Vs* ratio is observed due to the decrease of the *Vs* with the increase of pore pressure, while the *Vp* remains relatively constant (Ito *et al*., 1979). Positive *Vp/Vs* values, found within the shallow (3-6 km depth) sedimentary cover of the investigated area, suggest abundance of fluids and high pore-pressure.

Low V*p*/V*s* anomalies could be explained by the presence of vapour-phase or two-phase fluids volumes in geothermal area (e.g. Julian *et al*., 1996), by a lower saturation in fluids or by a quartz-enriched lithology (Kern, 1982; Tatham, 1982). In our tomographic models, considering that the *Vp/Vs* is on average high for the whole area (values higher than 1.84), the low *Vp/Vs* anomalies found between 6 and 10 km depth, in correspondence of very high *Vp* values can be explained by the presence of a less developed system of cracks within these bodies and, consequently, a lower content in fluids.

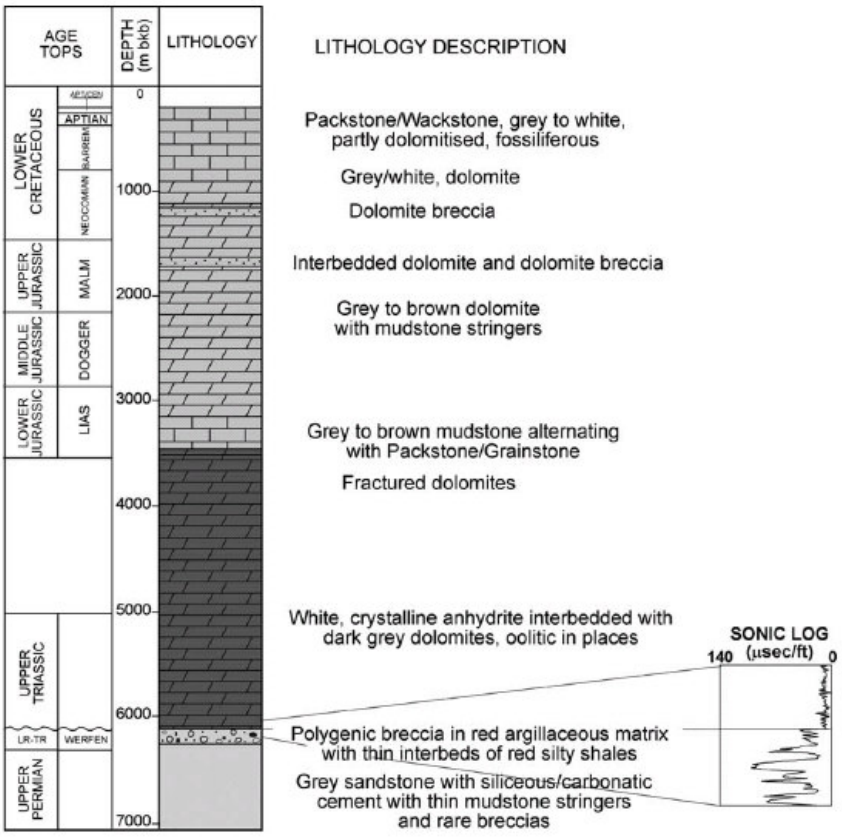

Fig. 5-5. Summary log of the Puglia-1 well showing the deep stratigraphy of the Apulian platform and the underlying Permo-Triassic clastic sequence. The inset sonic log shows the strong negative reflection coefficient associated with the contact between these two intervals (from Shiner *et al*., 2004).

Figures 5-6, 5-7 and 5-9 shows three *Vp* and *Vp/Vs* model vertical sections along with the relocated seismicity. The width for plotting earthquakes is ± 1 km. The location of the sections is shown in the 0 km depth *Vp* layer in fig. 5-4. The white and black contour lines define the well resolved area with SF ≤ 2 for the *Vp* and *Vp/Vs* model, respectively. On vertical sections, the main thrusts and normal faults were traced following the main *Vp* contrasts, and on the basis of our knowledge about the surface and the subsurface geology of the investigated area. *Vp/Vs* contrasts were also used to confirm the traced geometries.

Compressive structures

The deep structure beneath the Val d'Agri basin, in the central part of the model, is complex and appears preferentially due to the compressive tectonics.

In the vertical sections in fig. 5-6, the most impressive features are two high *Vp* anomalies, interesting the model between about 2-3 km (at the top) and about 9-11 km depth (at the bottom). *P*-wave velocity varies between 6 km/s in the shallower portion and 6.8 km/s at the

core of these anomalies, reaching values as high as 7 km/s at around 9 km depth. The wavelength of the anomalies, that is about 15 km in the shallower portion, decreases with depth. These two structural highs are also imaged in the 3 and 6 km depth *Vp* layers, corresponding to the NW-trending positive *Vp* anomalies (fig. 5-4).

We interpret these features as high velocity materials constituting the major folds involved in thrust, onto relatively low *Vp* anomalies; thus, they are well correlated to the major thrust anticlines and their related thrusts of the buried Apulia contractional belt. Consequently, we interpret the top of these two positive anomalies, with *Vp* about 6 km/s (figg. 5-6), as the culmination of the compressive structures of the Mesozoic Apulia platform. The high *Vp/Vs* anomalies associated to the top of these anticlines suggest that high pore pressure is present within the folds (fig. 5-7).

The top of the Apulia Platform (TAP hereinafter) is a well-constrained feature in the Val d'Agri area, because of the extensive exploration of the Val d'Agri oil field. Data coming from deep wells and vertical seismic profiles as well as high-resolution gravity modelling of the area (Menardi Noguera and Rea, 2000; Dell'Aversana, 2003; Shiner *et al*., 2004) furnish a very good image of the TAP in this area, allowing to better constrain our tomographic models. Fig. 5-8 shows a 2D schematic geologic model across the northern portion of the Val d'Agri basin with an accurate location of the top Apulia platform. The section in fig. 5-8 has the same position of the section A in fig. 5-6; consequently, we have drown in our section A the location of the TAP as reported in fig. 5-8. The section in fig. 5-8 shows the TAP at about 2 km depth along the western flank of the basin, while a deeper position of the same horizon is found further east. Along the eastern side of the basin, the depth of the TAP is also constrained by the Costa Molina 2 well (Menardi Noguera and Rea, 2000) that penetrate this horizon at about 2.9 km depth, testifying its deeper position along this side of the basin. This feature is visible in the section B in fig. 5-6, that crosses the central portion of the Val d'Agri basin close to the Costa Molina 2 well.

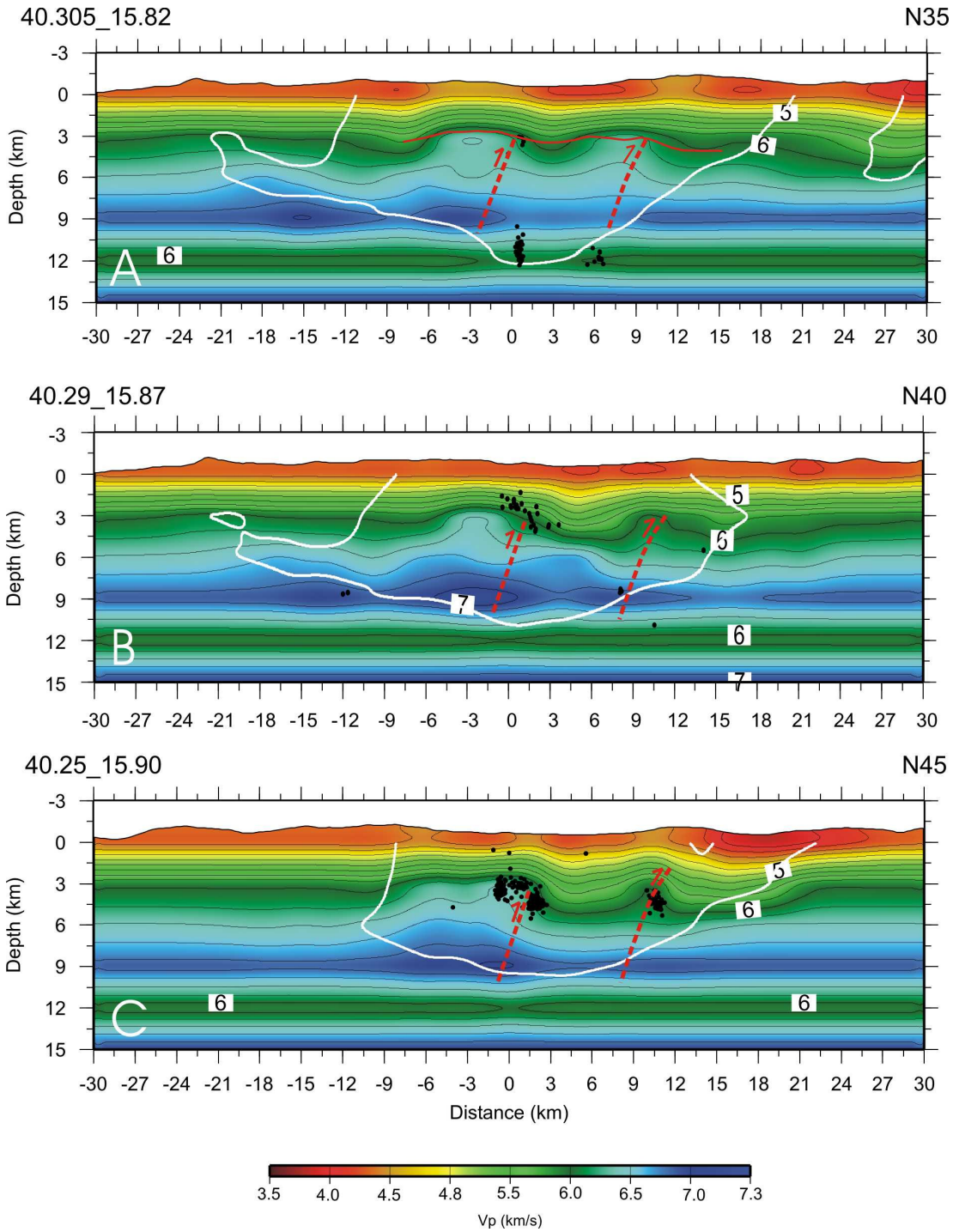

Fig. 5-6. V*p* model vertical cross sections. The white contour lines define the well resolved area with SF≤ 2. 3D relocated seismicity and the main tectonic features are also shown. Red dashed lines represent the main thrusts. The continuous red line represents a highly accurate location of the top of the Apulian platform along the northern portion of the Agri basin as reported by Dell'Aversana (2003). The top of the Apulia Carbonate Platform is located at about 1.8 km depth along the western border of the Agri basin while it is deeper along the eastern side of the basin. See text for further explanation.

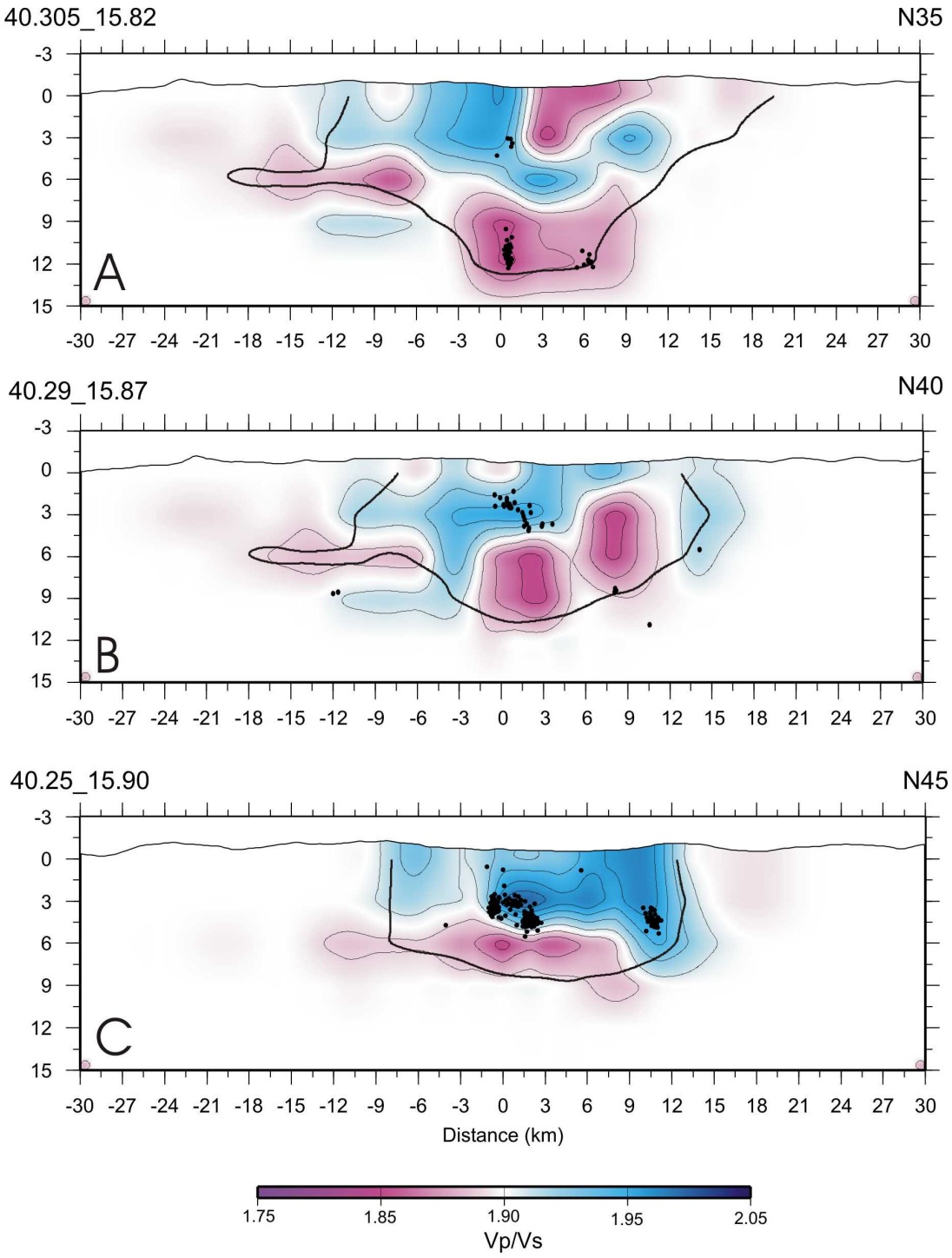

Fig. 5-7. ***Vp/Vs*** **model vertical sections. The black contour lines define the well resolved area with SF≤ 2.**

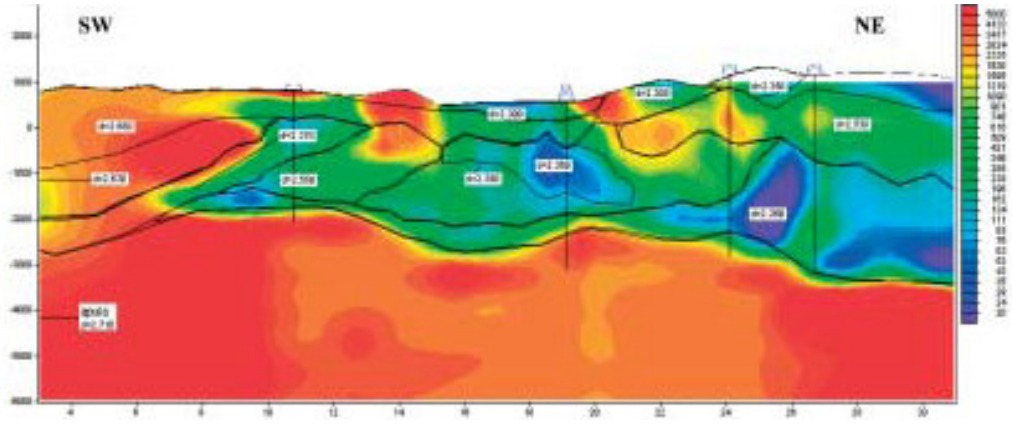

Fig. 5-8. Geological sketch model is from the work of Dell'Aversana (2003) showing a highly accurate location of the top Apulian platform along the northern portion of the Agri basin. The section has the same location of the vertical section A of fig. 5-6 and 5-11. The top of the Apulia Carbonate Platform is located at about 1.8 km depth along the western border of the Agri basin while is deeper along the eastern side of the basin. See text for further explanation.

Other published data constrain the position in map of these positive *Vp* anomalies. Figure 5-9 shows the comparison between the position of the approximate crestal locations of major Apulia Platform highs in the Val d'Agri area, constructed integrating deep wells and good-quality seismic lines (Shiner *et al*., 2004), and the *Vp* anomalies shown in the 3 km depth layer of the our tomographic model. The comparison delineates a very good match between the pattern of the positive *Vp* anomalies with the trend described by the structural highs of the Apulia carbonate platform (fig. 5-9); thus, suggesting that the chosen model parameterization is appropriate for imaging structures with a comparing wavelength.

The interpretation of the thrust-involved rock packages (the core of the anomalies), with *P*-wave velocities up to 6.8 km/s and low *Vp/Vs* value, is more ambiguous, due to lack of constrains or direct information (figg. 5-6 and 5-7). From active and passive seismic experiments along the Apennines, velocities close to this value were observed for the Triassic successions of the Apulia Platform (Mostardini and Merlini, 1986; Iannaccone *et al*., 1998; Improta *et al*., 2000, 2003; Chiarabba and Amato, 1997, 2003; Bisio *et al*., 2004, Bagh, 2006), suggesting that the Mio-Pliocene contractional deformation in the Lucanian Apennines involved Triassic successions at the core of the thrust anticlines.

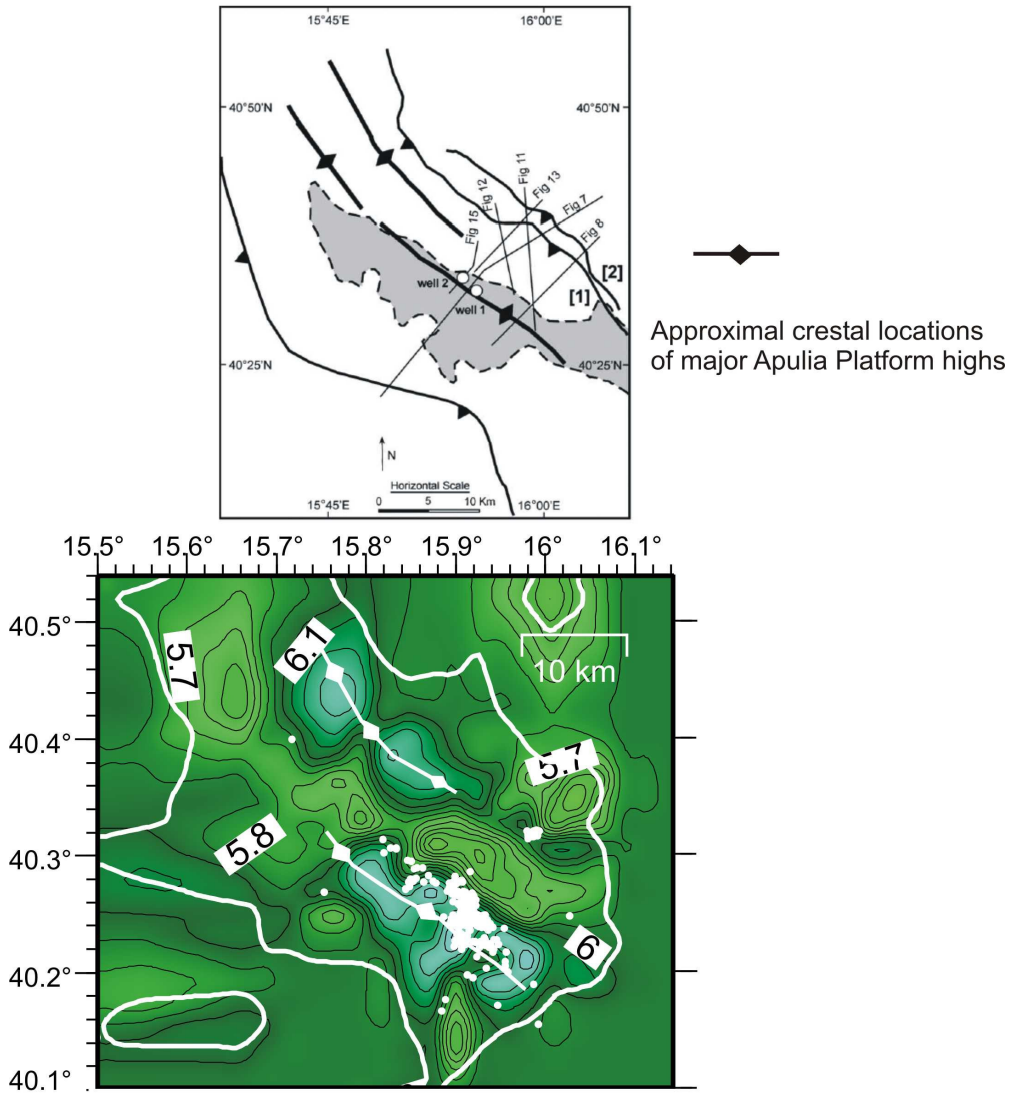

Fig. 5-9. Comparison between the approximate crestal locations of major Apulian Platform highs as shown be Shiner *et al.* (2004) and the 3 km depth *Vp* layer of the our tomographic model.

At depth between 8 and 10 km, V*p* models show velocities as high as 7 km/s. In the southern Apennines, velocities as high as 6.7 – 7.0 km/s were found from deep seismic sounding, passive and active seismic experiments and laboratory data (Chiarabba and Amato, 1997; Iannaccone *et al*., 1998; Improta *et al*., 2000, 2003; Bisio *et al*., 2004; Improta and Corciulo, 2006, Vinciguerra *et al.*, 2007). Iannaccone *et al*. (1998) and Improta *et al*. (2000, 2003) attributed these velocities to the Triassic successions (anhydrites and dolomites) of the Apulia Platform (southern Apennines, Sannio-Matese region), involved in the thrust tectonics.

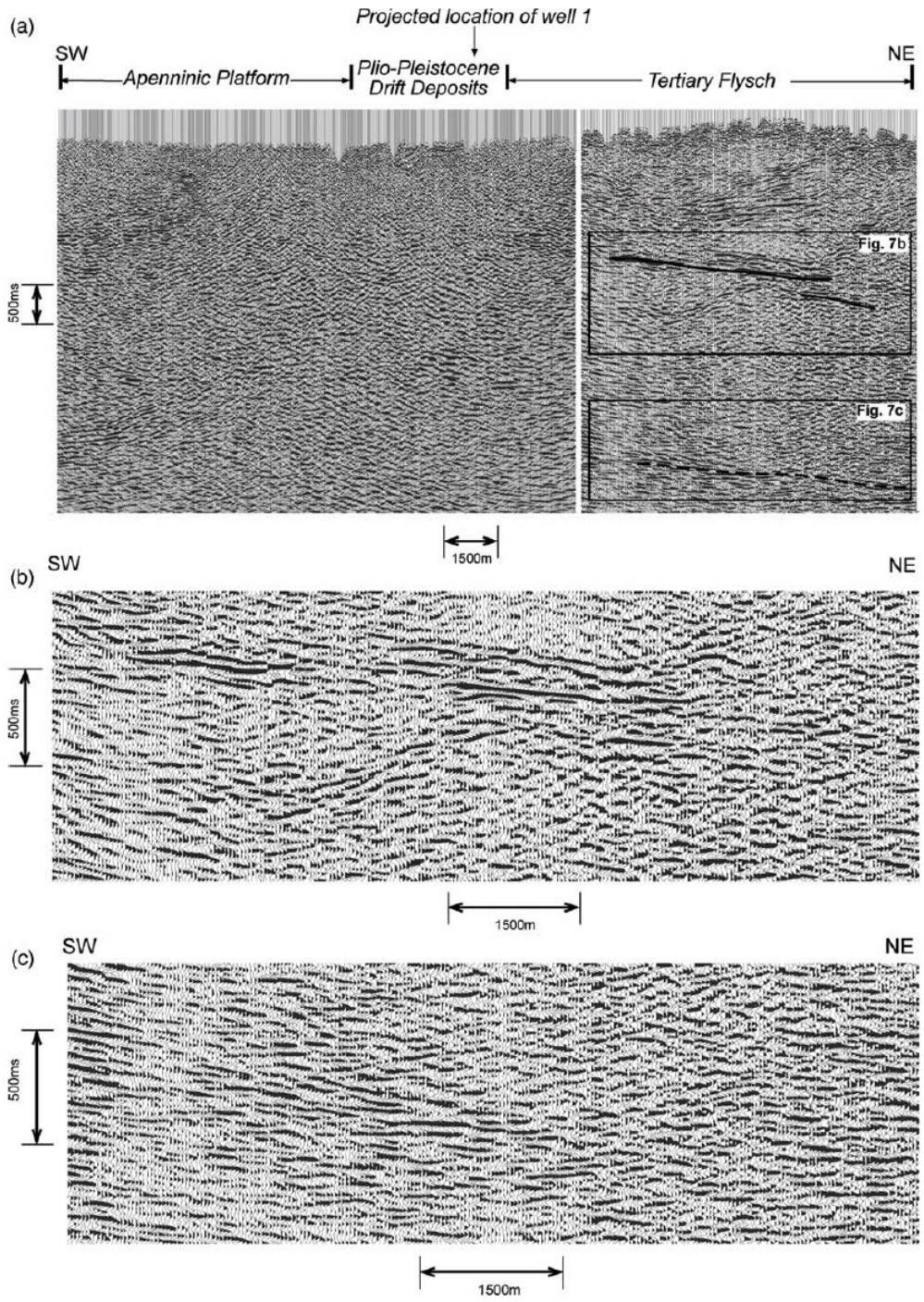

Fig. 5-10. (a) Regional 2D migrated seismic transect across the oilfield structure showing the lateral variation in seismic data quality that characterizes the study area. The location of this transect has almost the same location of the section B in fig. 5-6 and 5-7. The continuous black line shows the Top Apulian Platform seismic reflection whilst the dashed black line shows the Base Apulian Platform reflection. (b) Inset of (a) showing the Top Apulian seismic reflection in detail. (c) Inset of (a) showing the Base Apulian Platform reflection in detail. The horizontal and vertical scales used in this figure are such that the aspect ratio is approximately 1:1 at the Top Apulian Platform level. (from Shiner *et al.*, 2004) see text for further explanation.

Bisio *et al*. (2004) and Chiarabba and Amato (1997) do not exclude the involvement of the metamorphic basement in thrusting, as an explanation of the high V*p* anomalies imaged between 8 and 14 km depth beneath the northern sector of the Molise-Sannio arc. Improta and Corciulo (2006) explain the velocities exceeding 7.0 km/s, obtained by controlled-source non-linear tomography beneath the same region, as a constraint on crystalline basement involvement in the thrust stack. Following these studies, the deeper high V*p* anomalies, imaged beneath the Lucanian Apennines, can be explained with two hypotheses: *i*) a 5-6 km thick layer of Triassic anhydrites and prevalently dolomites; *ii*) an involvement of a metamorphic crystalline basement wedge in the thrust belt.

In order to shed light on the meaning of this high *Vp* region, we have considered the constrains about the position of the bottom of the Apulia Platform in this sector of the chain, posed by Shiner *et al*. (2004) through interpretation of subsurface data from seismic reflection profiles. Figure 5-10 shows a 2D migrated seismic transect along the Agri basin (from Shiner *et al.*, 2004). Along the eastern end of the profile, located beneath Tertiary flysch, seismic quality is moderate to good and several coherent, laterally continuous reflection events can be identified. The first one (also shown in the inset b) is the top of the Apulia Carbonate Platform. The second one, visible in figure 5-10c, is a poorly imaged deeper reflector. According to Shiner *et al*. (2004), on the base of regional correlation from wells and seismic data in the foreland, this reflector can be interpreted as the contact between the Burano anhydrites at the base of the Apulia Platform and the underlying Permo-Triassic sedimentary deposits. The identification of this horizon allow us to extrapolate the Apulia Carbonate Platform thickness in this sector of the southern Apennines; thus, allowing us to interpret the region with *Vp* up to 7 km/s located at about 9 km depth in our tomographic model. The thickness between the top and the bottom of the Apulia Platform, as shown in fig. 5-10, is about 2.5 s (TWT; Two Ways Time). This thickness roughly corresponds to 7.5 km and 8.1 km if we perform the depth conversion using an averaged *Vp* velocity of 6 km/s and 6.5 km/s, respectively. If we consider the top of the Apulia Platform located at about 2 km along the western side of the basin and at about 3 km along the eastern side of the basin, we found the contact between the Triassic anhydrites and the underlying Permo-Triassic succession between 10 and 11 km depth.

Following these considerations, we interpret the high *Vp* body, located between 8 and 10 km depth, as Triassic dolomites and anhydrites of the Burano formation. Furthermore, we tentatively interpret the underlying low-velocity body (*Vp* $\approx$ 6 km/s) as Permo-Triassic

sedimentary deposits (associated with a strong negative reflection coefficient in the Puglia 1 sonic log, see fig. 5-5).

The thrusts bounding the main folds have been drown following the main lateral velocity variations and following the suggestion of Shiner *et al*. (2004) who, by means of well-defined fault plane reflectors imaged on good-quality data, suggest that the wide anticlines of the Apulia Platform have been developed in the hanging wall of moderate-high angle (up to about 60°) reverse faults, interpreted as inverted Permo-Triassic extensional faults.

The vertical sections of figg. 5-6 and 5-7 help to clarify the connection between seismicity and the previously described compressive structures.

In section A the deep cluster of events located between 10 and 13 km depth is shown. Following the previous interpretation, the earthquakes are released at the contact between the bottom of the Apulia Platform and the underlying low *Vp* Permo-Triassic deposits. As shown in chapter 2, these seismic events are related to an about N30°-N20° sub-vertical fault plane characterized by a dip-slip kinematics (fig. 8 in chapter 2). Therefore, we speculate that they could be probably related to the re-activation of inherited structures at the bottom or even below the Apulia platform.

Both sections B and C (figg. 5-6 and 5-7) underscore that most of the seismicity is located at the top and within of the high *Vp* velocity anomalies.

In the section B, seismic events are located along a lateral *P*-wave velocity variation along the anticline limb, characterized by high *Vp/Vs* values (fig. 5-6 and 5-7). Seismic events roughly follow the local northeast-dipping warp of the velocity line of *Vp* 6 km/s.

In the section C, a very dense cluster of seismic events are located at the top and within the structural highs of the Apulia Platform, characterized by very high values of the *Vp/Vs* ratio (up to 1.98), indicating the presence of high pore pressure (fig. 5-7C). The small cluster located along the eastern side of the section, located in correspondence of a high *Vp/Vs* anomaly (fig. 5-7) might possibly be induced by oil extraction.

In summary, all sections highlight that seismicity preferentially occurs in regions characterized by high-*Vp* and *Vp/Vs* anomalies, related to the structural high of the Apulia Platform located beneath the western border of the Agri basin (figg. 5-4, 5-6, 5-7). This result is similar to those observed along the southern Apennines in other active fault regions like the Irpinia and the Benevento seismogenetic zones (Chiarabba and Amato, 1994 and Chiarabba and Selvaggi, 1997, respectively).

Extensional structures

The lateral resolution of the velocity models computed with the chosen model parameterization (a node every 3 km in the central part of the model), is on the order of 1.5 to 3 km, indicating that higher frequency heterogeneities are almost completely lost. As a result, the subsurface structure enlightened by tomography mostly consists of compressive structures developed during the Mio-Pliocene compressive tectonics, while the more recent extensional structures are not outstanding on the *Vp* models (fig. 5-11).

As discussed at length in previous chapters, in the Val d'Agri basin two Quaternary fault systems outcrop along the eastern and western side of the basin (fig. 1-8). The Eastern Agri Fault System (EAFS) acted since Lower Pleistocene to Holocene time reaching cumulative vertical displacement in the order of 500-700 m (Cello *et al.*, 2003 and also chapter 3 and chapter 4 of this work); and the Monti della Maddalena Fault System (MMFS) is a younger fault system (Middle Pleistocene-Holocene), which cumulative displacement, not fully constrained, does not exceed 200-300 m (Maschio *et al.*, 2005 and chapter 3 and 4). Consequently, small-displacement features like these faults are not well imaged in the coarse grid spacing tomographic models. Furthermore, as seen in the previous chapters 3 and 4, the Agri basin reaches a maximum thickness of 440 m and is filled by deposits with *Vp* in the range 1.3-3.0 km/s. Both the thickness and the *P*-wave velocities of the basin are not well-resolved in the *Vp* tomographic model (see figg. 5-4, 5-11). This can be explained by the inadequate model parameterization and by the vertical smearing of the surface layer inverted nodes, due to the poor lateral ray sampling.

The vertical sections shown in fig. 5-11 report the main Quaternary faults mapped at surface. An approximate downward projection has been drown following the dip-angles measured at the surface. Thus, faults of the EAFS have an approximate dip of 70° toward SW (Cello *et al.*, 2003), whilst those of the MMFS have an approximate dip of 60-65° toward NE (Maschio *et al.*, 2005 and also focal mechanism solutions shown in the second chapter).

In section A (fig. 5-11), two areas of strong lateral *Vp* contrasts are recognized. These features can be correlated with the following major faults exposed at the surface: the Monticello Fault (MTF) along the western margin of the basin (extensively described in chapters 3 and 4), and the major splays of the EAFS (almost parallel each other and, consequently, not distinctly reported in this section). Very few seismic events, located at about 3 km depth, can be tentatively associated to the Monticello fault.

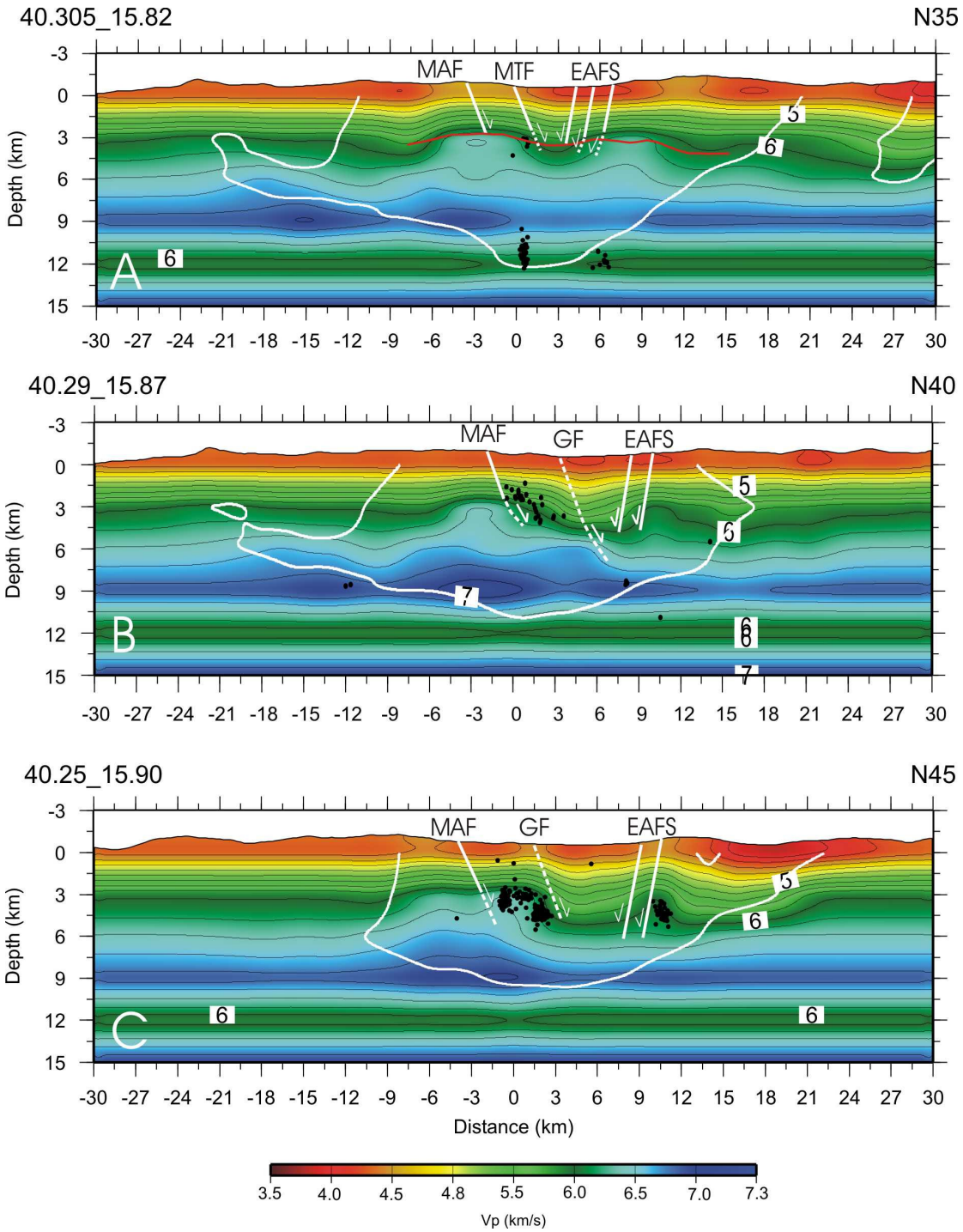

Fig. 5-11. V*p* model vertical cross sections. The white contour lines define the well resolved area with SF≤ 2. 3D relocated seismicity and the main tectonic features are also shown. White dashed and continuous lines represent the main Quaternary fault systems. The red continuous line represents a highly accurate location of the top apulian platform along the northern portion of the Agri basin as reported by Dell'Aversana (2003). EAFS= Eastern Agri Fault System; MAF= Monte Aquila Fault; MTF= Monticello Fault; GF= Grumento Fault (see figure 1-8 for active normal faults position).

In section B, three normal faults can be recognized from the *Vp* anomalies distribution, from SW to NE: the Monte Aquila Fault (MAF), at the eastern limb of the western anticlines; the Grumento Fault (GF), laterally correlative to the Monticello Fault, and the major splays of the EAFS. In this section, earthquakes are aligned along a 50-60° NE-dipping plane between 2 and 5 km depth, whose projection at the surface shows a good correspondence with the MAF. Furthermore, a sharp velocity contrast, located between 6 and 9 km depth, might suggest the prolongation at depth of the NE-dipping Grumento Fault.

In section C, located about 2 km south-east of the section B, the main lateral *Vp* contrasts are related to the same structures reported in the latter section. However, in section C, the larger spread of hypocenters indicates volume fractures rather than main fault slip. Furthermore, it is worth to note that seismicity occurs at the top and within the high *Vp* structural high of the Apulia platform.

Previous studies emphasize the notion that the lateral heterogeneities of the upper crust influence the geometry and segmentation of fault systems, and thus, the rupture evolution during large seismic events. High velocity zones along the faults can be related to high-strength regions where large stress drops and relatively large slip occur (e.g. Scholz, 1990; Chiarabba and Selvaggi, 1997; Chiarabba and Amato, 1997). Zhao and Kanamori (1992) showed that earthquakes are often concentrated within these high V*p* zones and proposed that these zones are responsible for the transition from stable to unstable slip. The *Ms*=7.3 El-Asnam (1980, Algeria), the *Ms*=6.9 Irpinia (1980, southern Apennines) and the *Ms*=6.6 Grevena (1995, Greece) earthquakes are good examples of rupture nucleation in a high *Vp* zones (Chiarabba *et al*., 1997; Chiarabba and Amato, 1997; Chiarabba and Selvaggi, 1997, respectively).

Within the well resolved area, comparing the distribution of the high *Vp* anomalies in the layers at 3, 6 and 9 km depth (fig. 5-4), with a reasonable depth-projection of mapped active normal faults, a spatial correlation between the high *Vp* features and the faults mapped along the western side of the Agri basin is remarkable.

Discussion

Structural inferences

The interpretation of the deep structure of the Lucanian Apennines is made problematic by the poor resolution at depths greater than 10 km of seismic reflection data (Mostardini and Merlini, 1986; Casero *et al*., 1988; Menardi Noguera and Rea, 2000; Mazzoli *et al*., 2000; Shiner *et al*., 2004; Butler *et al*., 2004). All studies clearly image the top Apulian platform

reflector but do not allow a good definition of the internal architecture of the belt. These uncertainties open to different interpretation of the deep tectonic style and of the degree of basement involvement for this sector of the Apennine chain (e.g. thin vs thick-skinned tectonic models).

The three-dimensional *Vp* and *Vp/Vs* tomographic models, obtained by inverting *P* and *S-P* times, have furnished interesting constrains about the structure of the Apulia Carbonate Platform in the Val d'Agri area. The main resolved features are the two NW-SE oriented wide anticlines of the Apulia platform bounded by moderate to high angle reverse faults (see figg. 5-4, 5-6 and 5-8). According to these models, the geometry of the thrust system within the Apulian carbonates (i.e. moderate to high angle faults), together with the occurrence of relatively low-displacement, (i.e. small thickness of the sediments involved in thrust), strongly suggest that a thick-skinned structural model is the more appropriate to describe the Apulian structures in the Val d'Agri area. Furthermore, the geometry of the high angle faults are likely to represent pre-existing structures (i.e. Permo-Triassic extensional faults) which were reactivated and inverted during compressive deformation.

On the contrary, it is widely accepted that thin-skinned structures characterize the shallower and older part of the thrust belt made of highly allochthonous tectonic units (Mostardini and Merlini, 1986; Menardi Noguera and Rea, 2000; Mazzoli *et al.*, 2000; Shiner *et al.*, 2004; Butler *et al.*, 2004; Scrocca *et al.*, 2005). Thus, in the Lucanian Apennines, a transition from thin-skinned to thick-skinned thrusting appears to have occurred through time. This hypothesis is in agreement with timing of deformation in southern Apennines. Analysis of synorogenic deposits indicates that thrust accretion of the allochthonous units derived from the deformation of Apennine Platform and the Lagonegro basin passive margin successions occurred mainly in Miocene to Early Pliocene time, whereas deeper thrusting involving the Apulia carbonate Platform occurred mainly during Late Pliocene to Early Pleistocene (Cello and Mazzoli, 1999; Menardi Noguera and Rea, 2000). The different type of tectonic style (thin-skinned and thick-skinned in the shallower and deeper portion of the thrust-belt, respectively) can be tentatively related to different relative motion during the Apennines accretion process due to the different nature of the Adriatic lithosphere involved in the subduction.

Seismotectonic inferences

The relation between earthquake occurrence and crustal structure suggests considerations about the seismotectonic in the Val d'Agri area.

Seismicity is preferentially located at shallow depth (between 2 and 6 km depth) beneath the south-western margin of the basin (see sections B and C in figg. 5-6 and 5-11 and the 3 km depth layer in fig. 5-4). It occurs at the top and within the western high *Vp* and high *Vp/Vs* anomaly interpreted as a structural high of the Apulia Platform (see section C in fig. 5-6) and follows the NW-trending elongation of this high *P*-wave velocity anomaly (see 3 km depth *Vp* layer in fig. 5-4). This result suggests that the seismic events are preferentially enucleated in high velocity zones corresponding to high-strength regions where large stress drops and relatively large slip occur (Scholz, 1990; Zhao and Kanamori, 1992; Chiarabba and Selvaggi, 1997; Chiarabba and Amato, 1997), allowing us to suppose that the next big earthquake in the Agri valley could be enucleated along this high-velocity zone located beneath the south-western side of the Agri basin.

Vertical sections in figg. 5-7 and 5-11 show an absence of seismicity at seismogenic depth (i.e. between 9 and 12 km depth) suggesting that the seismogenic structures in the Val d'Agri area may be presently locked, probably as a result of the recent (1857) large earthquake.

Finally, it is interesting to note that it is difficult to correlate the deep tectonic structures within the Apulia platform (i.e. the high angle reverse and normal faults) with the Quaternary normal fault systems exposed at the surface in the Agri basin (i.e. the MMFS and the EAFS). This observation suggests, on one hand, that the low-magnitude background seismicity recorded in the Val d'Agri area is mainly related to small fractures in the upper crust that only represent the upper termination of a major seismogenic structure located at greater depth, which is probably locked. On the other hand, it suggests that the old structures are not always reactivated as normal faults, even if they are kinematically compatible with the present-day NE-SW extension.

Conclusive remarks

In this PhD thesis, I have applied a multidisciplinary approach to investigate the upper crustal structure of the seismically active Val d'Agri region (Lucanian Apennines), focusing on the definition of location, geometry and kinematics of recent and active faults. Passive and active seismic data, complemented by a detailed field survey, have been used to shed light on the seismotectonics of the area.

- The passive seismic experiment (a temporary network, composed by up to 23 continuously recording seismic stations, installed in the Val d'Agri area for about 13 months) has allowed, for the first time, to accurately investigate the background seismicity in the area. We analysed a large dataset of about 2000 low-magnitude earthquakes ($-0.19<M_L<2.74$). This dataset has been used to:

- estimate the background seismicity release
- perform 1-D earthquake locations

About 700 earthquakes has been extracted from the preliminary large dataset, to hand-pick *S*-waves arrival times to better constrain hypocentral locations. The accurate dataset is characterized by location RMS values less than 0.3 s, azimuthal gaps smaller than 200° and horizontal and vertical errors less than 0.5 km s. These seismic events have furnished:

- *Vp* and *Vp/Vs* images of the upper crust down to 12 km depth though Local Earthquake Tomography
- Accurate 3D earthquake locations
- Subsurface geometry, kinematics and seismic activity of active fault segments
- Accurate focal mechanisms for 108 best-located events, computed by using the *P*-wave first motion polarity method

- The tomographic inversion of two high-resolution crustal profiles, about 15 km long, crossing the central sector of the basin, has furnished detailed *P*-wave velocity models of the shallow structure of the Agri basin down 1.5 km depth. The high-resolution tomographic images allowed an accurate imaging of :

- The Agri basin (basin geometry, depocenters locations, internal architecture of the basin infill)
- The fault systems bounding the basin (location, subsurface geometry, vertical throw estimate)

- Fieldwork was basically devoted to two targets: geological mapping and fault-kinematic analysis. I have used the collected data to better constrain geological and structural features of the Val d'Agri basin and, at the same time, to check the geological reliability of the high-resolution tomographic images.

Structural inferences

Deep structure (down to 12 km depth): The three-dimensional *Vp* and *Vp/Vs* tomographic models, obtained by inverting *P* and *S-P* times, have provided interesting constrains about the structure of the Apulia Carbonate Platform in the Val d'Agri area.

The main resolved features are the two NW-SE oriented high *Vp* and high *Vp/Vs* anomalies interpreted as structural highs of the Apulia platform (figg. 5-4, 5-6, 5-7). On the basis of the good match between the *Vp* anomalies of the tomographic model and the approximate crestal locations of major Apulia Platform highs in the Val d'Agri area, constructed integrating deep wells and good-quality seismic lines (Shiner *et al*., 2004), we interpret these anomalies as anticlines of the Apulia platform bounded by moderate to high angle reverse faults.

The geometry of the thrust system within the Apulian carbonates (i.e. moderate to high angle faults), together with the occurrence of relatively low-displacement of the thrust-involved rock packages (i.e. small thickness of the sediments involved in thrust), strongly suggest that a thick-skinned structural model is the more appropriate to describe the Apulian structures in the Val d'Agri area.

These anomalies have high *Vp/Vs* values indicative of high pore pressure (fig. 5-7); thus, they are consistent with carbonates of the Apulia platform that represent the oil reservoir in the area. It is important to note that high-pore pressure can play an important role in the earthquake generation and rupture evolution of normal faulting events.

Due to the inadequate model parameterization and to the poor lateral ray sampling of the surface layer, local earthquake tomography is not adequate to resolve the shallow upper crustal structure of the basin. Therefore, high resolution controlled source tomography is crucial to obtain information about the shallow structure.

Shallow structure (down to 1.5 km depth): The high-resolution *Vp* models, together with detailed geological mapping, highlight that the shallow architecture of the basin seems partly inherited by the previous (Pliocene) compressive tectonics, but largely controlled by Quaternary high angle normal faults, that cut both the bedrock and the Pleistocene basin infill on both sides of the basin (figg. 3-17, 3-18).

Faults located along the eastern flank of the valley are well-known in literature and correspond to the SW-dipping left-lateral transtensional Eastern Agri Fault System. V*p* images constrain faults location, whose identification is hampered by thick covers of fanglomerate deposits and provide independent estimate of the cumulative slip. We estimate a cumulated slip across the EAFS of about 800 m. This value is greater than previously estimated values by morpho-structural analysis (Cello *et al.*, 2003).

Along the western side of the basin, the tomographic images suggest NE-dipping normal faults, never mapped before, with vertical cumulative slip larger than 200 m (fig. 3-17). These faults affect the carbonates of the Monti della Maddalena unit (fig. 4-3). Recent fault activity along the western side of the basin is confirmed by the presence of a second, more recent depocenter, beneath the western border of the Agri basin. This finding is consistent with previous electrical resistivity tomographies (Colella *et al.*, 2004).

Seismotectonic inferences

We recorded, in thirteen months, about 2000 low-magnitude earthquakes ($-0.19<M_L<2.74$) testifying a high rate of background seismic release (about 3.3e-03 events/day/km^2) almost continuous in time.

Seismicity is preferentially located in the shallow crust (between 2 and 6 km depth) beneath the south-western margin of the basin (fig. 2-6). Earthquakes reflect small fractures spread in a volume whilst only few events enlighten fault plane geometry at depth (fig. 2-6, sections 10-11 and fig. 5-11, section B).

Seismicity occurs at the top and within the western high *Vp* and high *Vp/Vs* anomaly interpreted as a structural high of the Apulia Platform and follows the NW-trending elongation of this high *P*-wave velocity anomaly (figg. 5-4, 5-6). This result suggests that the seismic events enucleate in high velocity zones (Apulia carbonates) corresponding to high-strength regions where large stress drops and relatively large slip occur. This allows to suppose that the next big earthquake in the Agri valley could be enucleated along high-velocity zones located beneath the Agri basin as already observed for the 1980 Irpinia M6.9 normal faulting event (Amato *et al.*, 1992).

Few events occur at 10 – 12 km depth, beneath the central sector of the basin (fig. 5-6, section A), that is the seismogenic depth for large (M7) normal-fauting events of the southern Apennines. Hypocentral locations and focal mechanisms for these events suggest a N-S subvertical fault plane with pure dip-slip kinematics. We tentatively interpret this structure as

a pre-existing structure in the deep Apulia units now reactivated as dip-slip in the present SW-NE extensional tectonic regime.

Importantly, except for few induced seismicity, no seismic events have been recorded along the EAFS, considered by many Authors the surface expression of a seismogenic structure (Benedetti *et al.*, 1998; Cello *et al.*, 2000-2003, Barchi *et al.*, 2007). Therefore, our 3D hypocentral locations do not provide constrain about the geometry at depth for this fault system.

On the contrary, along the western side of the basin we note that few events are aligned along a 50° NE-dipping plane, whose projection at the surface well matches the fault scarp of Monte Aquila Fault. Late-Pleistocene-Holocene coseismic surface faulting along this fault is documented by recent paloseismological, geophysical and geo-morphological investigations (Maschio *et al.*, 2005; D'Addezio *et al.*, 2006; Improta and Bruno, 2007). Focal mechanisms for these events (fig. 2-8) indicate NW-SE striking and 55° to 65° NE-dipping fault planes characterized by normal kinematics with a NE-oriented T-axes. These results are in agreement with pseudo-focal mechanisms computed by fault slip inversion from surface exposures of fault planes (Maschio *et al.*, 2005 and also fig. 4-6). Thus, our results confirm the presence of active NE-dipping normal faults located along the south-western side of the Agri basin.

The absence of seismicity at seismogenic depth (i.e. between 9 and 12 km depth) suggests that the seismogenic structures in the Val d'Agri area may be presently locked, probably as a result of the recent (1857) large earthquake.

Therefore, our data can not definitely shed light on the hierarchy between the two Val d'Agri fault systems, and consequently, solve the worm debate about the seismogenic source responsible of the 1857 event. Nonetheless, our data furnish incontrovertible constrains about the present tectonic activity of some segments of the MMFS improving the knowledge of the geometry at depth and kinematics of this fault system. Earthquakes enlighten, between 2 and 6 km depth, a seismogenic fault about 15 km in length, able to generate M>5.5 earthquakes.

I gratefully acknowledge Paolo Dell'Aversana, Enterprise Oil Italiana and Shell Italia E & P S.p.A. for the permission to use Esit data.

Bibliography

Aki. K., and W.H.K. Lee, 1976. Determination of the three-dimensional anomalies under a seismic array using first P arrival times from local earthquakes. A homogeneous initial model. *J. Geophys. Res.*, vol. 81, pp. 4381-4399.

Alsaker, A., L.B. Kvamme, R.A. Hansen, A. Dahle and H. Bungum, 1991. The M_L scale in Norway, *Bull. Seism. Soc. Am.*, vol. 81 (2), pp. 379-398.

Amato, A., C. Chiarabba, L. Malagnini, and G. Selvaggi, 1992. Three-dimensional P-velocity structure in the region of the Ms=6.9 Irpinia, Italy, normal faulting earthquake. *Phys. Earth Planet. Inter.*, vol. 75, pp. 111-119.

Amato, A., P. Montone and M. Cesaro, 1995. State of stress in southern Italy from borehole breackout and focal mechanism data. *Geophy. Res. Lett.*, vol. 22, pp.3119-3122.

Amato, A., and P. Montone, 1997. Present day stress field and active tectonics in southern peninsular Italy. *Geophys. J. Int.*, vol. 130, pp. 519-534.

Amato, A., C. Chiarabba, G. Selvaggi, 1997. Crustal and deep seismicity in Italy (30 years after). *Ann. Geofis.*, vol. 40 (5), pp. 981-994.

Azzara, R., A. Basili, L., Beranzoli, C. Chiarabba, R. Di Giovambattista, and G. Selvaggi, 1993. The seismic sequence of Potenza (May 1990). *Annali di Geofisica*. Vol. 36. pp. 237-243.

Bagh, S., 2007. Crustal structure of the Abruzzo Apennines. *PhD thesis*, Università di Perugia. Pp. 120.

Bakun, W.H. and W.B. Joyner, 1984. The M_L scale in Central California, *Bull. Seismo. Soc. Am.*, vol. 74, pp 1827-1843.

Baratta, M., 1901. I terremoti d'Italia. Saggio di storia, geografia e bibliografia sismica italiana. Torino, pp. 1-950.

Barchi, M., A. Amato, G. Cippitelli, S. Merlini, S., and P. Montone, 2007. Extensional tectonics and seismicity in the axial zone of the Southern Apennines. *Boll. Soc. Geol. It.,* Spec. Issue 7, 47-56. CROP-04 (ed. By A. Mazzotti, E. Patacca and P. Scandone).

Benedetti, L., P. Tapponier, G.C.P. King, L. and Piccardi, 1998. Surface rupture due to the 1857 Southern Italian Earthquake. *Terra Nova*, vol. 10-4, pp. 206-210.

Bisio, L., R. Di Giovanbattista, G. Milano, and C. Chiarabba, 2004. Three-dimensional earthquake locations and upper crustal structure of the Sannio-Matese region (southern Italy). *Tectonophysics*, vol. 385, pp. 121-136.

Borraccini, F., M. De Donatis, D. Di Bucci, and S. Mazzoli, 2002. 3D Model of the active extensional fault system of the high Agri River valley, Southern Appennines, Italy. *Journal of the Virtual Explorer*, vol. 6, pp. 1-6.

Boschi, E., 1999. Catalogo parametrico dei Terremoti Italiani. ING, GNDT, SGA, SSN, Bologna.

Boschi, E., E. Guidoboni, G. Ferrari, D. Mariotti, G. Valensise and P. Gasperini, 2000. Catalogue of strong Italian earthquake, *Ann. Geofis.,* vol. 43-4, pp. 609-868.

Branno, A., E.G.I. Esposito, A. Marturano, S. Porfido and V. Rinaldis, 1983. Studio, su base macrosismica, del terremoto della Basilicata del 16 Dicembre 1857, *Boll. Soc. Natur. di Napoli*, vol. 92, pp. 249-338.

Burrato, P. and G. Valensise, 2007. Rise and fall of a hypothesized seismic gap: source complexity in the 16 December 1857, Southern Italy earthquake (Mw7.0). *Bull. Seism. Soc. Am*., accepted manuscript.

Butler, R.W.H., S. Mazzoli, S. Corrado, M. De Donatis, D. Di Bucci,R. Gambini, G. Naso,C. Vicoli, D. Scrocca, P. Shiner and V. Zucconi, 2004. Applying thick-skinned tectonic model to the Apennine thrust-belt of Italy: Limitations and implications, in McClay. K.R., ed., *Thrust tectonic and hydrocarbon system*: American Association of Petroleum Geologists Memoir vol. 82, pp. 647-667.

Casero, P., Roure, F., Endignoux, L., Moretti, L., Muller, C., Sage, L., Vially, R., 1988. Neogene geodynamic evolution of the southern Apennines. *Mem. Soc. Geol. Ital*., vol. 41, pp. 109-120.

Carbone, S., S. Catalano, F. Lentini and C. Monaco, 1988. Le unità stratigrafico-strutturali dell'Alta Val d'Agri (Appennino Lucano) nel quadro dell'evoluzione del sistema catena-avanfossa, *Mem. Soc. Geol. Ital*., vol. 41, pp. 331-341.

Carbone, S., S. Catalano, S. Lizzari, F. Lentini, and C. Monaco, 1991. Presentazione della carta geologica del Bacino del fiume Agri (Basilicata), *Mem. Soc. Geol. Ital*., vol. 47, pp.129-143.

Cassinis R., Scarascia S. and Lozej A. (2003). The deep crustal structure of Italy and surrounding areas from seismic refraction data. A new synthesis. *Boll. Soc. Geol. Ital*., vol. 122, pp. 365-376.

Catalano, S., C. Monaco, L. Tortorici, W. Paltrinieri and N. Steel, 2004. Neogene-Quaternary evolution of the southern Apennines. *Tectonics*, vol. 23, TC2003, doi:10.1029/2003TC001512.

Catchings, R.D., Rymer, M.J., Goldman, M.R., Hole, J.A., Huggins, R., and Lippus, C., 2002. High-resolution seismic velocities and shallow structure of the San Andreas Fault zone at Middle Mountain, Parkfield, California. *Bull. Seism. Soc. Am.*, vol. 92-6, pp. 2493-2503.

Cello, G. and S. Mazzoli, 1999. Apennine tectonics in southern Italy: a review. *J. of Geodynamics*, vol. 27, 191-211.

Cello, G., R. Gambini, S. Mazzoli, A. Read, E. Tondi and V. Zucconi, 2000. Fault zone characteristics and scaling properties of the Val d'Agri Fault System (Southern Apennines, Italy). *J. of Geodynamics,* vol. 29, pp. 293-307.

Cello, G., E. Tondi, L. Micarelli, L. Mattioni, 2003. Active tectonics and earthquake sources in the epicentral area of the 1857 Basilicata earthquake (Southern Italy). *J. Geodynamics*, vol. 36, pp. 37-50.

Chiarabba, C., and A. Amato, 1997. Upper-crustal structure of the Benevento area (southern Italy): fault heterogeneities and potential for large earthquakes. *Geophys. J. Int*., vol. 130, pp. 229-239.

Chiarabba C., Amato A. and Meghraoui M., 1997. Tomographic images of the El-Asnam fault zone and the evolution of the seismogenic thrust-related fault. *J. Geoph. Res*., vol. 102, pp. 24485-24498.

Chiarabba C. and Selvaggi G., 1997. Structural control on fault geometry: The example of the Grevena Ms 6.6 normal faulting earthquake, *J. Geoph. Res*., vol. 102, pp. 22445-22457.

Chiarabba, C., and A. Amato, 2003. *Vp* and *Vp/Vs* images in the Mw 6.0 Colfiorito fault region (central Italy): a contribution to the understanding of seismotectonic and seismogenic processes. *J. Geophys. Res.*, vol. 108, doi:10.1029/2001JB001665.

Chiarabba, C., L. Jovane, R. Di Stefano, 2005. A new view of Italian seismicity using 20 years of instrumental recordings. *Tectonophysics*, vol. 395, pp. 251-268.

Chiaraluce, L., A. Amato, M. Cocco, C. Chiarabba, G. Selvaggi, M. Di Bona, D. Piccinini, A. Deshamps, L. Margheriti, F. Courboulex and M. Ripepe, 2004. Complex normal faulting in the Apennines thrust-and-fold belt: the 1997 seismic sequence in Central Italy. *Bull. Seism. Soc. Am*., vol. 94, pp. 99-116.

Chiaraluce, L., Barchi, M., Collettini, C., Mirabella, F., Pucci, S., 2005. Connecting seismically active normal faults with Quaternary geological structures in a complex extensional environment: the Colfiorito 1997 case history (northern Apennines, Italy). *Tectonics*, vol. 24. doi: 10.1029/2004TC001627.

Cimini, G.B, P. De Gori and A. Frepoli, 2006. Passive seismology in Southern Italy: the SAPTEX array. *Annals of Geophysics*. Vol. 49. pp. 825-840.

Cinque, A., E. Patacca, P. Scandone, and M. Tozzi, 1993. Quaternary kinematic evolution of the southern Apennines: Relationships between surface geological features and deep lithospheric structures, *Ann. Geofis*., vol. 36, pp. 249-259.

Colella, A., V. Lapenna, E. Rizzo, 2004. High-resolution imaging of the High Agri Valley Basin (southern Italy) with electrical resistivity tomography. *Tectonophysics*, vol. 386, 29-40.

CPTI Working Group (2004). Catalogo Parametrico dei Terremoti Italiani, version 2004 (CPTI04). INGV, Milan, available from http://emidius.mi.ingv.it/CPTI/

Crosson, R.S., 1974. Non-linear least squares crustal structure from earthquake data (abstract). *Eos. Trans. AGU*, 56, pp. 1145

Cucci, L., D'Addezio, G., Valensise, G., and Burrato, P., 1996. Investigating seismogenic faults in Central and Southern Apennines (Italy): modelling of fault-related landscape features. *Ann. Geofis*., vol. 34, pp. 603-618.

Cucci, L., Pondrelli, S., Frepoli, A., Mariucci, M.T., and Moro, M., 2004. Local pattern of stress field and seismogenic sources in Meandro Pergola basin and in Agri valley (Southern Italy). *Geophys. J. Int*., vol. 156, pp. 575-583.

D'Agostino, N., and McKensie D., 1999. Convective support of long wavelength topography in the Apennines (Italy). *Terra Nova*, vol. 11, pp. 234-238.

D'Argenio, B., T. Pescatore & P. Scandone, 1975. Structural pattern of the Campania-Lucania Apennines, *Le Scienze, Quaderni della Ricerca Scientifica,* vol. 90, pp. 313-327.

Dell'Aversana, P., S. Morandi, L. Improta, A. Zollo, 1999. Tomographic images from 'global offset' seismic data inversion in Southern Apennines. *Extended abstracts from 61st EAGE conference,* Helsinki.

Dell'Aversana, P., Ceragioli, E., Morandi, S., and Zollo, A., 2000. A simultaneous acquisition test of high density 'Global Offset' seismic in complex geological setting. *First Break*, vol. 18, pp. 87-96.

Dell'Aversana, P., 2001. Integration of seismic, MT and gravity data in a thrust belt interpretation, *First Break*, vol. 19, pp. 335-341.

Dell'Aversana, P., Colombo, D., Buia, M., and Morandi, S., 2003. Velocity/interface model building in a thrust belt by tomographic inversion of global offset seismic data. *Geophisical Prospecting*, vol. 51, pp. 23-35.

Dell'Aversana, P., 2003. Integration loop of 'global offset' seismic, continuous profiling magnetotelluric and gravity data. *First break*, vol. 21, pp. 32-41.

Dewey, J.F., Helman, M.L., Turco E., Hutton, D.W.H. & Knott, S.P., 1989. Kinematics of the western Mediterranean, in *Alpine Tectonics*, eds. Coward, M.P., Dietrich, D., & Park, R.G., *Geol. Soc. Lond. Spec. Publ.,* vol. 45, pp. 265-283.

Di Niro, A., S.I. Giano and N. Santangelo, 1992. Primi dati sull'evoluzione geomorfologica e sedimentaria del bacino dell'Alta Val d'Agri (Basilicata). Studi Geol. Camerti, vol. 1992/1, pp. 257-263.

Di Niro, A., and Giano S.I., 1995. Evoluzione geomorfologica del bordo orientale dell'alta Val d'Agri (Basilicata), *Studi Geol. Camerti* spec. issue 1995/2, pp. 207-218.

DISS Working Group (2007). Database of Individual Seismogenic Sources (DISS), Version 3.0.4: A compilation of potential sources for earthquakes larger than M 5.5 in Italy and surrounding areas, http://www.ingv.it/DISS/

Di Stefano, R., C. Chiarabba, F. Lucente and A. Amato, 1999. Crustal and uppermost mantle structure in Italy from the inversion of P-wave arrival times: geodynamic implications. *Geophys. J. Int.,* vol. 139, pp. 483-498.

Di Stefano, R., Aldersons, F., Kissling E., Baccheschi P., Chiarabba C., Giardini D., 2006. Automatic seismic phase picking and consistent observation error assessment; application to the italian seismicity. *Geophys. J. Int*, vol. 165–1, pp. 121-134.

Doglioni, C., 1991. A proposal of kinematic modelling for W-dipping subduction. Possible applications to the Tyrrenian-Apennines system. *Terra Nova*, vol. 3, pp. 423-434.

Doglioni, C., P. Harabaglia, G. Martinelli, F. Mongelli, G. Zito, 1996. A geodynamic model of the Southern Apennines accretionary prism. *Terra Nova*, vol. 8, 540-547.

Dolan, J.F., K. Sieh, T.K. Rockwell, R.S. Yeats, J. Shaw, J. Suppe, G. Huftile and E. Gath, 1995. Prospects for larger or more frequent earthquakes in greater metropolitan Los Angeles, California. *Science*, vol. 267, pp. 199-205.

Dolan, J.F., and T.L. Pratt, 1997. High resolution seismic profiling of the Santa Monica fault zone, West Los Angeles, California. *Geophys. Res. Lett.*, vol. 24-16, pp. 2051-2054.

Eberhart-Phillips, D., 1986. Three-dimensional velocity structure in the northern California Coast Ranges from inversion of local earthquake arrival times. *Bull. Seismol. Soc. Am.*, vol. 76, pp. 1025-1052.

Eberhart-Phillips, D., 1990. Three-dimensional P and S velocity structure in the Coalinga region, California. *J. Geophys. Res*., vol. 95, pp. 15343-15363.

Eberhart-Phillips, D., and A.J. Michael, 1993. Three-dimensional velocity structure, seismicity and fault structure in the Parkfield region, central California. *J. Geophys. Res*., vol. 98, pp. 15737-15758.

Eberhart-Phillips, D., 1993. Local earthquake tomography: earthquake source regions, in *Seismic tomography*, edited by H.M. Iyer and K. Hirahara, Chapman and Hall, New York. Pp. 613-643.

Eberhart-Phillips, D. and M. Reyners, 1997. Continental subduction and three-dimensional crustal structure: the Northern South Island, New Zeland. *J. Geophys. Res*., vol. 102, pp. 11843-11861.

Ekstrom, G., 1994. Teleseismic analysis of the 1990-1991 earthquakes near Potenza. *Annals of Geophysics*. Vol. 38. pp. 283-300.

Ferranti, L. & Oldow, J.S., 2005. Rates of late Neogene deformation along the southwestern margin of Adria, Southern Apennines orogen, Italy. In *The Adria microplate: GPS Geodesy, Tectonics, and Hazard, eds Pinter, N., Grenerczy, G., Medak, D., Stein, S. & Weber, J.C., Kluwer Academic Publishers, Dordecht.* Pp. 93-116.

Frepoli, A., F.R. Cinti, L. Amicucci, G.B. Cimini, P. De Gori and S. Pierdominici, 2005. Pattern of seismicity in the lucanian Apennines (Southern Italy) from recording by SAPTEX temporary array. *Annals of Geophysics*. Vol. 48. pp. 1035-1054.

Galadini, F., C. Meletti and A. Rebez, 2000a. Le ricerche del GNDT nel campo della pericolosità sismica (1996-1999). *CNR-Gruppo Nazionale Per la Difesa dei Terremoti*, Roma. 397 pp.

Gambini, S. (2003). Structural evolution of the Val d'Agri fault system, Southern Apennines, Italy. PhD thesis, University of Leeds, UK.

Gasparini, C., Iannaccone, G., & Scarpa, R., 1985. Fault-plane solutions and seismicity of the Italian peninsula. *Tectonophysics*, 117, 59-78.

Giano, S.I., La Penna, V., Piscitelli, S., Schiattarella, M., 1997. Nuovi dati geologici e geofisici sull'assetto strutturale dei depositi continentali quaternari dell'alta Val d'Agri (Basilicata). *Il Quaternario*, 10 (2), 589-594.

Giano, S.I., La penna V., Piscitelli, S., and Schiattarella, M., 2000. Electrical imaging and self-potential surveys to study the geological setting of the Quaternary slope deposits in the Agri high valley (Southern Italy). *Ann. Geofis.*, vol. 43-2, pp. 409-419.

Giano, S.I., Maschio, L., Alessio, M., Ferranti, L., Improta, S., and Schiattarella, M., 2000. Radiocarbon dating of active faulting in the Agri high valley, Southern Italy. *J. Geodynamics*, 29, 371-386.

Hearn, T.M., and J.F. Ni, 1994. *Pn* velocities beneath continental collision zones, *Geophys. J. Int*., vol.117, pp. 273-283.

Herrero, A., A. Zollo, and J. Virieux, 2000. 2D non linear first arrival time inversion applied to Mt. Vesuvius active seismic data, *Am. Geophys. Un*., Fall Meeting, 15-19 December 2000, San Francisco, USA.

Iannaccone, G., L. Improta, P. Capuano, A. Zollo, G. Biella, R. De Franco, A. Deshamps, M. Cocco, F. Mirabile, and R. Romeo, 1998. A P-wave velocity model of the upper crust of the Sannio region (Southern Apennines, Italy). *Ann. Geofis.*, vol. 41, pp. 567-582.

Improta, L., A. Zollo, M.R. Frattini, J. Virieux, A. Herrero, and P. Dell'Aversana, 2000. Mapping interfaces in an overthrust region by non-linear traveltime inversion of reflection data, *Am. Geophys. Un*., Fall Meeting, 15-19 December 2000, San Francisco, USA.

Improta, L., G. Iannaccone, P. Capuano, A. Zollo, and P. Scandone, 2000. Inferences on the upper crustal structure of the southern Apennines (Italy) from seismic refraction investigations and subsurface data. *Tectonophysics,* vol. 317, pp. 273-297.

Improta, L., A. Zollo, A. Herrero, R. Frattini, J. Virieux, and P. Dell'Aversana, 2002. Seismic imaging of complex structures by non-linear traveltime inversion of dense wide-angle data: application to a thrust belt. *Geophys. J. Int*., vol. 151, pp. 264-278.

Improta, L., A. Zollo, P.P. Bruno, A. Herrero, F. Villani, F., 2003. High resolution seismic tomography across the 1980 (Ms 6.9) Southern Italy earthquake fault scarp. *Geophysical Research Letters*, vol. 30-10.

Improta, L., M. Bonagura, P. Capuano and G. Iannaccone, 2003. An integrated geophysical investigations of the upper crust in the epicentral area of the 1980, Ms=6.9, Irpinia earthquake (Southern Italy). *Tectonophysics*, vol. 361, pp. 139-169.

Improta, L. and M. Corciulo, 2006. Controlled source nonlinear tomography: a powerful tool to constrain tectonic models of the Southern Apennines orogenic wedge, Italy. *Geology*, vol. 34-11, pp. 941-944.

Improta, L. and P. P. Bruno, 2007. Combining seismic reflection with multi-fold wide-aperture profiling: an effective strategy for high-resolution shallow seismic imaging of active faults. *Geophys. Res. Lett.*, 34L20310

Ito H., De Vilbiss J. and Nur A., 1979. Compressional and shear waves in saturated rock during water-steam transition. *J. Geophys. Res.*, vol. 84, pp. 4731-4735.

Julian B. R., 1996. Three-dimensional seismic image of a geothermal reservoir: The Geysers, California. *Geophys. Res. Lett.*, vol. 23, pp. 685-688.

Kern, H., 1982. *P*- and *S*-wave velocities in crustal and mantle rocks under the simultaneous action of high confining pressure and high temperature and the effect of rock microstructure, in *High-Pressure Research in Geoscience*. Stuttgart, Germany. pp. 15-45

Lahr, J.C., 1989. HYPOELLIPSE/version 2.00: a computer program for determining local earthquakes hypocentral parameters, magnitude and first motion pattern. *U. S. Geol. Surv. Open-File Rep*. 89-116, pp. 92.

Lay, T., and T.C. Wallace, 1995. Modern global seismology. Springer, New York.

Lee, W.H.K., and J.C. Lahr, 1975. HYPO71: a computer program for determining hypocenter, magnitude and first motion pattern of local earthquakes, *U. S. Geol. Surv. Open-file Rep.* 75-311, 1-116.

Lucente, F.P., C. Chiarabba, G.B. Cimini, and D. Giardini, 1999. Tomographic constrains on the geodynamic evolution of the Italian region. *J. Geophys. Res.*, vol. 104, pp. 20307-20327.

Lucente, F.P., N. Piana Agostinetti, M. Moro, G. Selvaggi and M. Di Bona, 2005. Possible fault plane in a seismic gap area of the southern Apennines (Italy) revealed by receiver function analysis. *J. Geophy. Res.*, vol. 110, B04307, doi: 10.1029/2004JB003187.

Lutter, W.J., R.L. Nowack, L.W. Braile, 1990. Seismic imaging of the upper crustal structure using travel times from the PASSCAL Ouachita Experiment. *J. Geophy. Res.*, vol. 95, pp. 4633-4646.

Malinverno, A & Ryan, W.B.F., 1986. Extension in the Tyrrhenian sea and shortening in the Apennines as a result of arc migration driven by sinking of the lithosphere. *Tectonics,* vol. 5, pp. 227-245.

Mallet, R., 1862. Great Neapolitan Earthquake of 1857, in *The First Principles of Observational Seismology*, (ING-SGA Bologna), London, pp.862.

Marrett, R. and Allmendinger, R.W., 1990. Kinematic analysis of fault-slip data. *J. Struct. Geol.*, vol. 12, pp. 973-986.

Maschio, L., Ferranti, L., Burrato, P., D'Addezio, G., De Martini, P.M., Improta, L., Pantosti, D., Bruno, P., La penna, V., Piscitelli, S., and Rizzo, E., 2004. Pattern of active crustal

extension in the Monti della Maddalena (Val D'Agri, Lucania Appenines) provided by integrated structural, paleoseismological, electric and seismic investigations. *XXIII G.N.G.T.S. Meeting*, Rome, Italy, Ext. Abst., 199-200.

Maschio, L., Ferranti, L., and Burrato, P., 2005. Active extension in Val d'Agri area, Southern Appenines, Italy: implications for the geometry of seismogenic belt. *Geophys. J. Int*., vol. 162, pp. 591-609.

Mazzoli, S., S. Corrado, M. De Donatis, D. Scrocca, R.W.H. Butler, D. Di Bucci, G. Naso, C. Nicolai, V. Zucconi, 2000. Time and space variability of thin skinned and thick skinned thrust tectonics in the Apennines (Italy). *Rendiconti Lincei Scienze Fisiche e Naturali*, vol. XI.

Mazzoli, S., S. Barkham, G. Cello, R. Gambini, L. Mattioni, P. Shiner, and E. Tondi, 2001. Reconstruction of continental margin architecture deformed by the contraction of the Lagonegro Basin, southern Italy. *J. Geol. Soc*., vol. 158, pp. 309-319.

Mazzotti, A.P., E. Stucchi, G.L. Fradelizio, Zanzi L., and P. Scandone, 2000. Seismic exploration in complex terrains: a processing experience in the Southern Apennines. *Geophysics*, vol. 65, pp. 1402-1417.

Menardi Noguera A. and Rea G., 2000. Deep structure of the Campanian-Lucanian Arc (Southern Apennine, Italy). *Tectonophysics*, vol. 324, pp. 239-265.

Menke, W., 1989. *Geophysical data analysis: Discrete inverse theory, Int. Geophys. Ser*., vol. 45, pp. 285, Academic, San Diego, California.

Micheal, A.J., and D. Eberhart-Phillips, 1991. Relations among fault behaviour, surface geology and three-dimensional velocity models, *Science*, vol. 253, pp. 651-654.

Michelini, A., and T.V. McEvilly, 1991. Seismological studies at Parkfield. Simultaneous inversions for velocity structure and hypocenters using cubic B-splines parameterization, *Bull. Seismol. Soc. Am.*, vol. 81, pp. 524-552.

Monaco, C., L. Tortorici and W. Paltrinieri, 1998. Structural evolution of the Lucanian Appennines, Southern Italy. *Journal of structural geology*, vol. 20-5, pp. 617-638.

Montone, P., M.T. Mariucci, S. Pondrelli and A. Amato, 2004. An improved stress map for Italy and surrounding regions (central Mediterranean). *J. Geophys. Res.*, vol. 109, B10410, doi: 10.1029/2003JB002703.

Morandi, S., and Ceragioli E., 2002. Integrated interpretation of seismic and resistivity images across the "Val d'Agri" graben (Italy). *Ann. Geofis*., vol. 45, pp. 259-271.

Mostardini, F., and S. Merlini, 1986. Appennino centro-meridionale: sezioni geologiche e proposta di modello strutturale, *Mem. Soc. Geol. It.,* vol. 35, pp. 177-202.

Pantosti, D., and Valensise, G., 1990. Faulting mechanism and complexity of the November 23, 1980, Campania-Lucania earthquake, inferred from surface observation. *J. Geophys. Res*., vol. 95, B10, 15,319-15,341.

Pantosti, D., D.P. Schwartz and G. Valensise, 1993. Paleoseismology along the 1980 Irpinia earthquake fault and implications for earthquake recurrence in the Southern Apennines, *J. Geophys. Res.*, vol. 95(15), pp. 15319-15341.

Patacca, E., and P. Scandone, 2001. Late thrust propagation and sedimentary response in the trust-belt-foredeep system of the southern Apennines (Pliocene-Pleistocene), in *Anatomy of an orogen: The Apennines and Adjacent Mediterranean Basins*, edited by G. B. Vai and I. P. Martini, pp. 401-440, Kluwer Acad., Norwell, Mass.

Pavlis G. L. and Booker J. R. (1980). The mixed discrete continuous inversion problem application to the simultaneous determination of earthquake hypocenters and velocity structure. *J. Geophys. Res.*, vol. 85, pp. 4801-4810.

Piccinini, D., *et. al*., 2003. A microseismic study in a low seismicity area of Italy: the Città di Castello experiment. *Ann. Geophys*., vol. 46-6, pp. 1315-1324.

Pierdominici, S., F.R. Cinti, M.T. Mariucci and P. Montone, 2002. Data from boreholes as a tool for active tectonics studies: example in southern Apennines. International workshop active faults: analysis, processes and monitoring, Camerino, 3-6/05/02.

Piromallo, C., and A. Morelli, 2003. *P*-wave tomography of the mantle under the Alpine-Mediterranean region. *J. Geophys. Res.*, vol. 108, doi:10.1029/2002JB001757.

Podvin, P. & Lecomte, I., 1991. Finite difference computation of traveltimes in very contrasted velocity model: a massively parallel approach and its associated tools. *Geophys. J. Int*., vol. 105, pp. 271-284.

Reasenberg, P.A. and D. Oppenheimer, 1985. FPFIT, FPPLOT and FPPAGE: Fortran computer programs for calculating and displaying earthquake fault plane solutions. *U.S. Geological Survey – Open file report*, n° 85-739.

Richter, C.F., 1935. An instrumental earthquake magnitude scale, *Bull. Seism. Soc. Am.* , vol. 25, pp. 1-32.

Richter, C.F., 1958. Elementary seismology (W.H. Freeman & Co., San Francisco). Pp. 768.

Roure, F., P. Casero, and R. Vially, 1991. Growth processes and melange formation in the southern Apennines accretionary wedge. *Earth Planet. Sci. Lett*., vol. 102, pp. 395-412.

Royden, L.H., Patacca E., Scandone P., 1987. Segmentation and configuration of subducted lithosphere in Italy: an important control on thrust-belt and foredeep-basin evolution. *Geology*, vol.15, pp. 714-717.

Sambridge M.S., and Gallagher K. (1993). Earthquake hypocenter location using genetic algorithms. *Boll. Seismol. Soc. Am*., vol. 83, pp. 1467-1491.

Scandone, P., 1967. Studi sulla geologia lucana: le serie calcareo-silicomarnosa e i suoi rapporti con l'Appennino calcareo, *Bollet. Soc. Natur. Napoli*, vol. 76, pp. 1-175.

Scarascia, S., Lozej, A., Cassinis, R., 1994. Crustal structures of the Ligurian and Tyrrhenian and Ionian Seas and adjacent onshore areas interpreted from wide-angle seismic profiles. *Boll. Geofis. Teor. Appl.*, vol. 36, pp.141-144.

Schiattarella, M., P. Di Leo, P. Beneduce, S.I. Giano, 2003. Quaternary uplift vs tectonic loading: a case study from the Lucanian Apennine, southern Italy. *Quater. Inter.*, vol. 101, pp. 239-251.

Scholz, C. H., 1990. The mechanics of earthquake and faulting. *Cambridge University Press, New York.*

Scrocca, D., Carminati, E., and Doglioni, C., 2005. Deep structure of the Southern Apennines, Italy: thin-skinned or thick-skinned? *Tectonics*, vol. 24, TC3005, doi: 10.1029/2004TC001634.

Selvaggi, G., 1998. Spatial distribution of horizontal seismic strain in the Apennines from historical earthquakes. *Ann. Geofis.*, vol. 41, pp. 241-251.

Shiner, P., A. Beccaccini, and S. Mazzoli, 2004. Thin-skinned versus thick-skinned structural models for Apulian carbonate reservoirs: constrains from the Val d'Agri Fileds, S Apennines, Italy. *Marine and Petroleum Geology*, vol. 21, 805-827.

Speranza, F., and Chiappini, M., 2002. Thick-skinned tectonics in the external Apennines, Italy: New evidence from magnetic anomaly analysis. *J. Geophys. Res.*, vol. 107 (B11), 2290, doi: 10.1029/2000JB000027.

Stein, S. and M. Wysession, 2004. An introduction to seismology, earthquakes and Earth structure. *Blackwell Publishing*. Pp.

Tatham R. H. (1982). *Vp/Vs* and lithology. *Geophysics*, vol. 47, pp. 34-344.

Thurber, C.H., 1986. Analysis methods for kinematic data from local earthquakes. *Rev. Geophys.*, vol. 24, pp. 793-805.

Thurber, C.H., 1983. Earthquake location and three-dimensional crustal structure in the Coyote Lake area, Central California. *J. Geophys. Res.*, vol. 88, pp. 8226-8236.

Thurber, C.H., 1993. Local earthquake tomography: velocities and Vp/Vs theory. In *Seismic tomography*, edited by H.M. Iyer and K. Hirahara, Chapman and Hall, New York. Pp. 563-580.

Thurber, C.H., Roecker, S., Roberts, K., Gold, M., Powell, L., and Rittger, K., 2003. Earthquake locations and three-dimensional fault zone structure along the creeping section of the San Andreas fault near Parkfield, CA: preparing for SAFOD. *Geophys. Res. Lett.*, vol. 30-3, 1112-1118.

Thurber, C., Roecker, S., Zhang, H., Baher, S., and Ellsworth, W., 2004. Fine-scale structure of the San Andreas fault zone and location of the SAFOD target earthquakes. *Geophys. Res. Lett.*, 31.

Toomey, D.R., and G.R. Foulger, 1989. Tomographic inversion of local earthquake data from Hengill-Grendsalur Central Volcano Complex, Iceland, *J. Geophys. Res*., vol. 94, pp. 17497-17510.

Um J. and Thurber C.H. (1987). A fast algorithm for two-dimensional seismic ray tracing. *Bull. Seismol. Soc. Am*., vol. 77, pp. 972-986.

Valensise, G., Pantosti, D., D'Addezio, G., Cinti F.R. and Cucci L., 1993. L'identificazione e la caratterizzazione di faglie sismogenetiche nell'Appennino Centro-Meridionale e nell'arco calabro: nuovi risultati e ipotesi interpretative. *Atti del XII convegno GNGTS*, pp. 331-342.

Valensise, G., and D. Pantosti, 2001a. The investigation of potential earthquake sources in peninsular Italy: a review. *Journal of seismology,* vol. 5, pp. 287-306.

Valensise, G. and Pantosti, D., 2001b (eds). Database of potential sources for earthquakes larger than 5.5 in Italy, *Ann. Geofis*., 44(4), pp.910.

Vidale, J., 1988. Finite-difference calculation of travel times. *Bull. Seism. Soc. Am*., vol. 78, pp. 2062-2076.

Wallace, R.E., 1984. Pattern and timing of late Quaternary faulting in the Great Basin province and relation to some regional tectonic features. *J. Geophys. Res*., vol. 89, pp. 5763-5769.

Wells, D.L. and Coppersmith K.J., 1994. New empirical relationship among magnitude, rupture length, rupture width, rupture area, surface displacement. *Bull. Seism. Soc. Am*., vol. 84, pp. 974-1002.

Wang, C.Y., 2002. Detection of a recent earthquake fault by the shallow reflection seismic method. *Geophysics*, 67, 5, 1465-1473.

Wessel, P., & Smith, W.H.F., 1995. New version of the Generic Mapping Tools released, EOS, *Trans. Am. Geophys. Un.*, vol. 76, pp. 329.

Westway, R., and J.A. Jackson, 1987. The earthquake of 1980 November 23 Campania-Basilicata (Southern Italy). *J. Geophy. Res*., vol. 90, pp. 375-443.

Working Group CPTI, 1999. Catalogo parametrico dei terremoti italiani, ING, GNDT, SGA SSN, Bologna.

Yilmaz, O., 1987. Seismic data processing. *Soc. Exploration Geophys*., Tulsa, Oklahoma.

Zhao D. and Kanamori H., 1992. The 1992 Landers earthquake sequence: earthquake occurrence and structural heterogeneities. *Geophys. Res. Lett*., vol. 20, pp. 1083-1086.

Zhao, D., and H. Kanamori, 1995. The 1994 Northridge earthquake: 3-D crustal structure in the rupture zone and its relation to the aftershock locations and mechanisms, *Geophys. Res. Lett.*, vol. 22, pp. 763-766.

Zhao, D., and H. Negishi, 1998. The Kobe earthquake: seismic image of the source zone and its implications for the rupture nucleation, *J. Geophys. Res.*, vol. 103, pp. 9967-9986.

Appendix A

050521 2021
Z= 3.58 dis= 1
QF= A QP= A

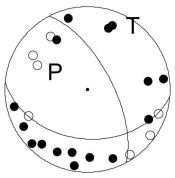

050523 0120*
Z= 4.56 dis= 2
QF= B QP= A

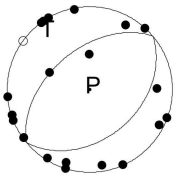

050525 0041
Z= 3.63 dis= 0
QF= A QP= B

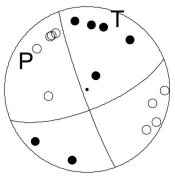

050527 0110
Z= 3.14 dis= 1
QF= B QP= A

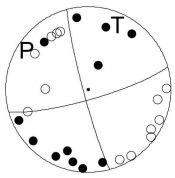

050612 2031
Z= 2.36 dis= 1
QF= B QP= A

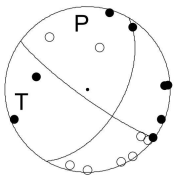

050613 2224
Z= 2.49 dis= 0
QF= A QP= A

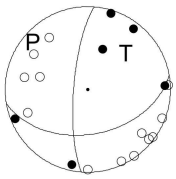

050618 2201
Z= 2.39 dis= 0
QF= A QP= B

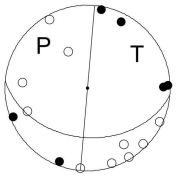

050620 0441
Z= 1.97 dis= 1
QF= B QP= A

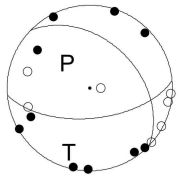

050621 0018
Z= 2.62 dis= 2
QF= B QP= A

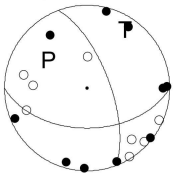

050621 1248
Z= 4.13 dis= 1
QF= B QP= A

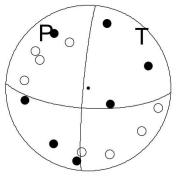

050623 0153
Z= 1.93 dis= 1
QF= B QP= A

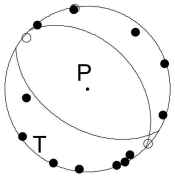

050623 2347
Z= 2.95 dis= 0
QF= A QP= A

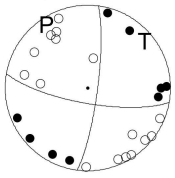

050625 0707
Z= 3.52 dis= 1
QF= B QP= A

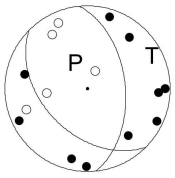

050625 1532
Z= 4.06 dis= 1
QF= B QP= A

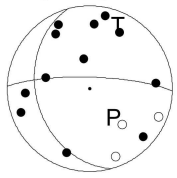

050626 1927
Z= 11.48 dis= 0
QF= A QP= A

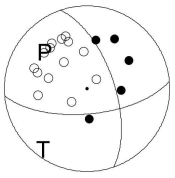

050628 0750
Z= 11.36 dis= 0
QF= A QP= A

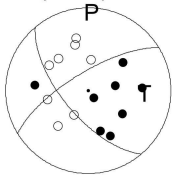

050629 0515
Z= 11.64 dis= 1
QF= A QP= B

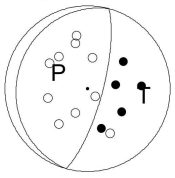

050702 0238
Z= 11.58 dis= 1
QF= B QP= B

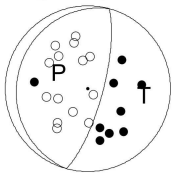

050702 0505
Z= 12.15 dis= 0
QF= A QP= B

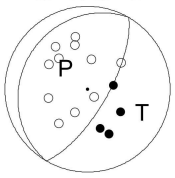

050715 0016
Z= 2.86 dis= 1
QF= B QP= A

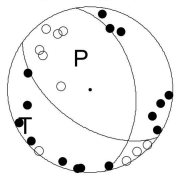

050718 1147
Z= 2.87 dis= 0
QF= A QP= A

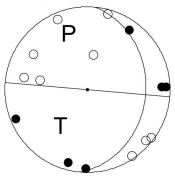

050719 0826*
Z= 5.31 dis= 2
QF= B QP= A

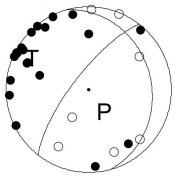

050720 1427
Z= 11.19 dis= 1
QF= B QP= B

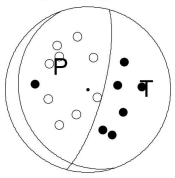

050720 1443
Z= 11.93 dis= 1
QF= A QP= B

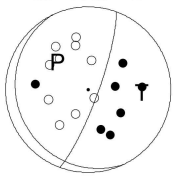

050720 2022
Z= 11.56 dis= 0
QF= A QP= B

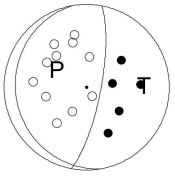

050722 1757
Z= 12.79 dis= 0
QF= A QP= A

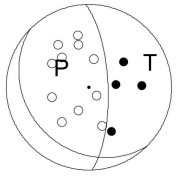

050722 2104
Z= 11.63 dis= 0
QF= A QP= A

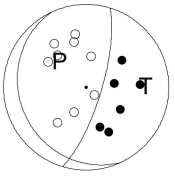

050727 0847
Z= 3.54 dis= 1
QF= A QP= A

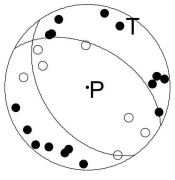

050730 2214
Z= 11.09 dis= 1
QF= A QP= A

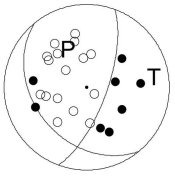

050730 2300*
Z= 11.17 dis= 1
QF= B QP= B

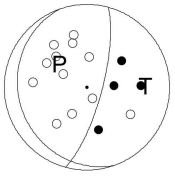

050730 2303
Z= 10.31 dis= 0
QF= A QP= A

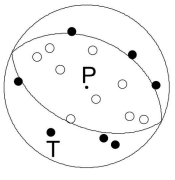

050809 0355
Z= 11.02 dis= 1
QF= B QP= B

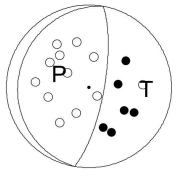

050811 0609
Z= 3.47 dis= 1
QF= A QP= A

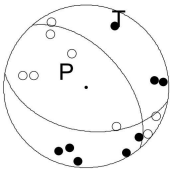

050812 0207
Z= 4.29 dis= 1
QF= B QP= A

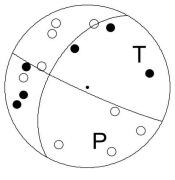

050812 0730
Z= 11.70 dis= 0
QF= A QP= A

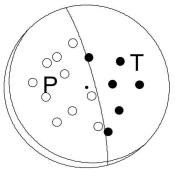

050825 0208
Z= 5.03 dis= 2
QF= B QP= A

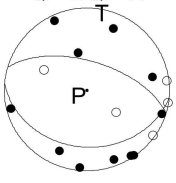

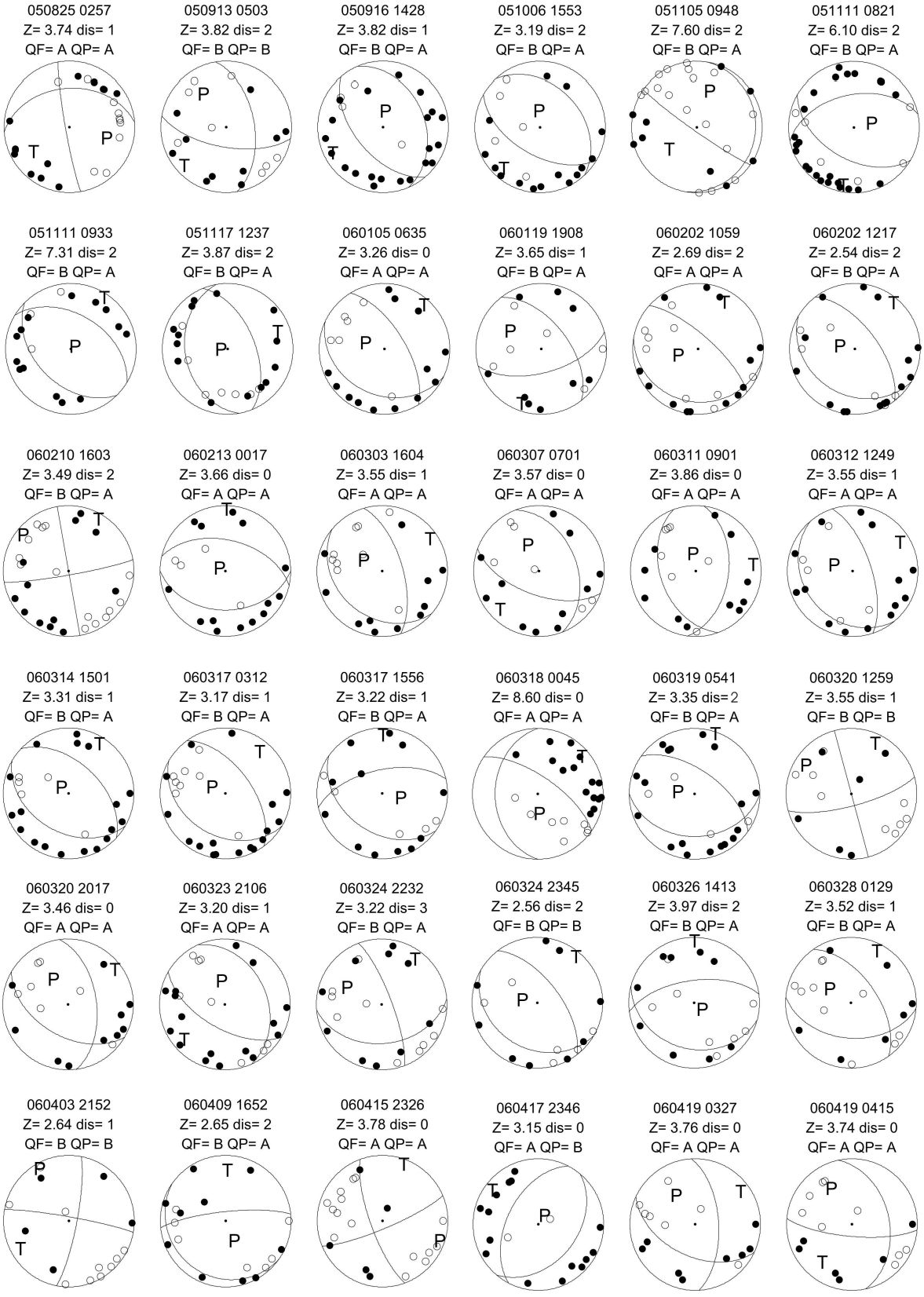
050825 0257
Z= 3.74 dis= 1
QF= A QP= A
050913 0503
Z= 3.82 dis= 2
QF= B QP= B
050916 1428
Z= 3.82 dis= 1
QF= B QP= A
051006 1553
Z= 3.19 dis= 2
QF= B QP= A
051105 0948
Z= 7.60 dis= 2
QF= B QP= A
051111 0821
Z= 6.10 dis= 2
QF= B QP= A
051111 0933
Z= 7.31 dis= 2
QF= B QP= A
051117 1237
Z= 3.87 dis= 2
QF= B QP= A
060105 0635
Z= 3.26 dis= 0
QF= A QP= A
060119 1908
Z= 3.65 dis= 1
QF= B QP= A
060202 1059
Z= 2.69 dis= 2
QF= A QP= A
060202 1217
Z= 2.54 dis= 2
QF= B QP= A
060210 1603
Z= 3.49 dis= 2
QF= B QP= A
060213 0017
Z= 3.66 dis= 0
QF= A QP= A
060303 1604
Z= 3.55 dis= 1
QF= A QP= A
060307 0701
Z= 3.57 dis= 0
QF= A QP= A
060311 0901
Z= 3.86 dis= 0
QF= A QP= A
060312 1249
Z= 3.55 dis= 1
QF= A QP= A
060314 1501
Z= 3.31 dis= 1
QF= B QP= A
060317 0312
Z= 3.17 dis= 1
QF= B QP= A
060317 1556
Z= 3.22 dis= 1
QF= B QP= A
060318 0045
Z= 8.60 dis= 0
QF= A QP= A
060319 0541
Z= 3.35 dis= 2
QF= B QP= A
060320 1259
Z= 3.55 dis= 1
QF= B QP= B
060320 2017
Z= 3.46 dis= 0
QF= A QP= A
060323 2106
Z= 3.20 dis= 1
QF= A QP= A
060324 2232
Z= 3.22 dis= 3
QF= B QP= A
060324 2345
Z= 2.56 dis= 2
QF= B QP= B
060326 1413
Z= 3.97 dis= 2
QF= B QP= A
060328 0129
Z= 3.52 dis= 1
QF= B QP= A
060403 2152
Z= 2.64 dis= 1
QF= B QP= B
060409 1652
Z= 2.65 dis= 2
QF= B QP= A
060415 2326
Z= 3.78 dis= 0
QF= A QP= A
060417 2346
Z= 3.15 dis= 0
QF= A QP= B
060419 0327
Z= 3.76 dis= 0
QF= A QP= A
060419 0415
Z= 3.74 dis= 0
QF= A QP= A

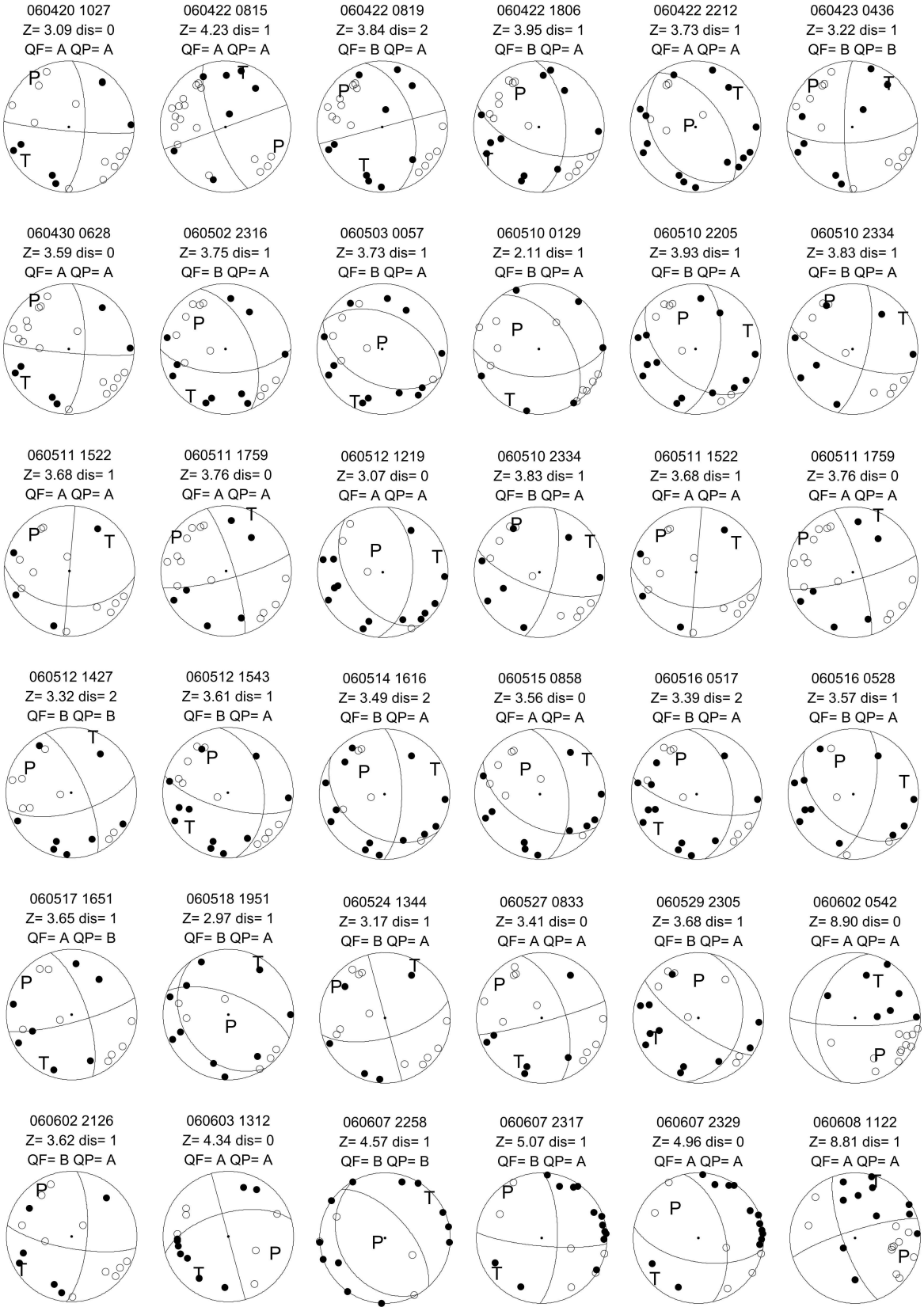
060420 1027
Z= 3.09 dis= 0
QF= A QP= A
060422 0815
Z= 4.23 dis= 1
QF= A QP= A
060422 0819
Z= 3.84 dis= 2
QF= B QP= A
060422 1806
Z= 3.95 dis= 1
QF= B QP= A
060422 2212
Z= 3.73 dis= 1
QF= A QP= A
060423 0436
Z= 3.22 dis= 1
QF= B QP= B
060430 0628
Z= 3.59 dis= 0
QF= A QP= A
060502 2316
Z= 3.75 dis= 1
QF= B QP= A
060503 0057
Z= 3.73 dis= 1
QF= B QP= A
060510 0129
Z= 2.11 dis= 1
QF= B QP= A
060510 2205
Z= 3.93 dis= 1
QF= B QP= A
060510 2334
Z= 3.83 dis= 1
QF= B QP= A
060511 1522
Z= 3.68 dis= 1
QF= A QP= A
060511 1759
Z= 3.76 dis= 0
QF= A QP= A
060512 1219
Z= 3.07 dis= 0
QF= A QP= A
060510 2334
Z= 3.83 dis= 1
QF= B QP= A
060511 1522
Z= 3.68 dis= 1
QF= A QP= A
060511 1759
Z= 3.76 dis= 0
QF= A QP= A
060512 1427
Z= 3.32 dis= 2
QF= B QP= B
060512 1543
Z= 3.61 dis= 1
QF= B QP= A
060514 1616
Z= 3.49 dis= 2
QF= B QP= A
060515 0858
Z= 3.56 dis= 0
QF= A QP= A
060516 0517
Z= 3.39 dis= 2
QF= B QP= A
060516 0528
Z= 3.57 dis= 1
QF= B QP= A
060517 1651
Z= 3.65 dis= 1
QF= A QP= B
060518 1951
Z= 2.97 dis= 1
QF= B QP= A
060524 1344
Z= 3.17 dis= 1
QF= B QP= A
060527 0833
Z= 3.41 dis= 0
QF= A QP= A
060529 2305
Z= 3.68 dis= 1
QF= B QP= A
060602 0542
Z= 8.90 dis= 0
QF= A QP= A
060602 2126
Z= 3.62 dis= 1
QF= B QP= A
060603 1312
Z= 4.34 dis= 0
QF= A QP= A
060607 2258
Z= 4.57 dis= 1
QF= B QP= B
060607 2317
Z= 5.07 dis= 1
QF= B QP= A
060607 2329
Z= 4.96 dis= 0
QF= A QP= A
060608 1122
Z= 8.81 dis= 1
QF= A QP= A